DISSERTATION

submitted to the

Combined Faculty of Natural Sciences and Mathematics

of the Ruperto-Carola University Heidelberg, Germany

for the degree of

Doctor of Natural Sciences

presented by

Mgr. Gabriela Nass Kovacs

Born in Přerov, Czech Republic

Date of oral examination: ……

LIGHT-ENERGY CONVERSION IN RHODOPSINS STUDIED BY TIME-RESOLVED SERIAL FEMTOSECOND CRYSTALLOGRAPHY

Referees: Prof. Dr. Ilme Schlichting

Dr. Thomas Barends

Contents

Acknowledgements

I was very fortunate to get to know so many talented, motivated and inspiring people during my PhD – I would never get this far without their aid and support. I am very grateful to …

… my supervisor Ilme Schlichting for excellent support and guidance throughout my PhD years. I really appreciate the long hours she invested into teaching me so many different skills – from everything related to growing and grilling crystals to scientific reasoning and writing. I am also thankful for the presentation and leadership lessons that came when entrusting me with the many conference talks and scientific collaborations. This really made me grow professionally and personally.

… my second supervisor Thomas Barends for outstanding scientific support. This work would not be possible without his extraordinary crystallographic expertise and programming skills.

… Prof. Rüdiger Hell and Dr. Axel Mogk for being interested thesis committee members.

… my former second supervisor Anton Meinhart for the many hours he spent on theoretical and practical aspects of crystallography with me.

… Prof. Rebecca Wade, Prof. Barbara di Ventura and Prof. Britta Brügger for being helpful TAC members.

… Tatiana Domratcheva for her patience when introducing me to the world of energy diagrams and for the many inspiring scientific and personal discussion we had.

… all past and current members of the FEL group. It was a privilege to be part of this multifaceted team where everyone always gave their best, no matter how long the beamtime was. I learned so much from you and enjoyed working with all of you –Bruce, Bob, Thomas, Lutz, Karol, Chris, Marco, Marie, Mario, Miriam and Alex. I am particularly grateful to Bruce and Bob for teaching me the art of injection and to Marie, Marco and Miriam for being superb enthusiastic team players during the many projects we did together – also outside of work.

… Jochen Reinstein for the many important scientific exchanges, including the Grafit tutorial on an Easter Sunday.

… Chris Roome for instantaneously fixing everything computer-related that (I) broke, for periodic donations of succulents and for his sharp British humour.

… my bench-neighbour Mirek for all the indispensable lab advice and help ranging from cloning to crystallization. I am particularly grateful for the help with insect cells expression. This really helped me to progress and avoid many potential pitfalls!

… Kazu, Rob, Udo, Clara, Diana, Akram, Andreas and Sarah for being always ready to give me a crash course on instruments and methods that I was not familiar with but desperately needed to use.

…Elisabeth for supporting me from my first to last day – first by helping me to get around in the lab and later by excellent technical assistance in my projects.

… Melanie for all the careful MS analyses.

… Sabine and Kerstin for all the secret tricks and help in the lab.

… to my current office mates Egle and Sarah for sharing so much more than just the space with me! I also appreciate your help with candy eating and watering of our little window garden.

… to my past office buddies Udo, Jule, Andrea, Felix, Monica, and Kaste for the friendly and disciplined atmosphere in the office. It was a nice place to come to every morning!

… Matthias, Max, Madeleine, Tiia, Veronika, Melanie, Lukas, Mónica, Anna, Tadeo, Alexa, Ulli and Alex C. for co-creating a friendly atmosphere in the Biomolecular mechanisms department and for all the nice lunch breaks or evening drinks!

… the extraordinary administrative support that we get from the Verwaltung. I am particularly grateful to Martina Blochmann for all the flawless (and if needed express) travel arrangements and to Ulrike Sanders for always professionally mastering my travel reimbursements despite my badly filled-in forms.

… the media and dish-washing kitchens for the great service they provide– it makes a huge difference.

… the workshop for their accurate and fast manufacturing of items for my project.

… the Max Planck Society for providing funding and conditions for cutting-edge research at the MPI for medical Research.

… the HBIGS graduate school – the courses and events that they provided really added value to my PhD!

… my many collaborators - the groups of Ramona Schlesinger, Prof. Joachim Heberle and of Prof. Karsten Heyne from FU Berlin for supply of material, experiments and countless discussion; Prof. Stefan Haacke for experiments and crucial discussions and Jacques-Philippe Colletier for the sophisticated and incredibly high-throughput data analysis.

… my parents, sister, grandmother and mother-in-law for providing an always welcoming home with a sense of belonging despite the long distance and infrequent visits.

… my best husband for love, care and understanding.

Summary

Light is an important environmental factor used by light-sensitive proteins, photoreceptors, as a source of information or energy. In several classes of photoreceptors, photon absorption triggers the isomerization around a double bond in the light-sensitive chromophore. In rhodopsins, the isomerization of the chromophore retinal is one of the fastest light-triggered processes and it initiates different, protein-specific functions, spanning from vision and sleep regulation to light-energy conversion and phototaxis. The best characterized rhodopsin is bacteriorhodopsin (bR), a light-activated proton pump. Spectroscopic techniques were used to characterize both the ultrafast processes related to the isomerization, but also the later steps when the translocation of protons occurs. Structural knowledge of the later intermediates was provided mostly by X-ray crystal structures of cryo-trapped bR or its mutants, contributing to a good understanding of the proton pumping steps. However, the ultrafast processes evolving on a sub-ps and ps time-scale are not amenable for time-resolved X-ray crystallography using synchrotron radiation, thus no structures of the ultrafast bR intermediates could be obtained. This changed with the advent of novel X-ray sources, the X-ray free-electron lasers, which make time-resolved serial femtosecond crystallography (TR-SFX) on the sub-ps time-scale possible. This enables to address the most puzzling questions about the isomerization not only spectroscopically and computationally, but also structurally. Why is the isomerization of retinal in rhodopsins highly bond-specific and efficient, whereas it is neither specific nor efficient when retinal is free in solution? Is the protein affecting the isomerization reaction not only sterically, but also actively?

This work used TR-SFX to obtain structures of the ultrafast intermediates in bR in order to observe the structural changes in the retinal and in the protein on the sub-ps and ps time-scale. Large quantities of well-diffracting bR microcrystals were prepared in very viscous lipidic cubic phase. Time-resolved SFX experiments were performed only with liquid samples before the start of this thesis, therefore methods used for delivery of viscous samples in SFX needed to be adapted specifically for this time-resolved experiment.

The crystal structures obtained in the TR-SFX experiment on bR visualize the torsion of the isomerizing double bond in retinal. They also show oscillatory motion in the retinal and in specific protein residues and their distances to other residues or to ordered, functionally relevant water molecules. Changes in the distances in the internal hydrogen-bonded network of water molecules and protein residues are also observed. Similar to many TR-SFX experiments, this experiment was performed at very high pump laser excitation intensity, which can induce multiphoton processes, complicating the functional interpretation of the observations made. Unlike other TR-SFX experiments, this work acknowledges and

addresses this caveat. Since the TR-SFX experiment could not be repeated at lower laser excitation intensity, additional spectroscopic and computational studies were carried out instead to gain more insight into multiphoton processes. These indeed provide new findings about decay channels in the multiphoton regime. Yet, it still remains open what the implications for the observations made in the TR-SFX structures are. In spite of that, a comparison of the TR-SFX observations with published spectroscopic and computational work performed in the single-photon regime shows remarkable similarities.

The insights obtained in this work pave the way for future TR-SFX experiments using optimal excitation conditions, which will clarify the relation of the observed structural changes to single-photon processes. This will allow judging whether the concerted motions observed in the retinal, residues and water molecules are part of the mechanism by which the protein actively controls the isomerization reaction of the chromophore. Furthermore, the methodological advances established here with the model system bR can now be directly applied to study other more challenging rhodopsins, such as the new family of anion-conducting channelrhodopsins (ACR). This work established insect-cell expression of an ACR protein and identified crystallization conditions yielding showers of microcrystals, which is the first step towards a future TR-SFX experiment.

Zusammenfassung

Licht ist ein wichtiger Umweltfaktor, der von lichtempfindlichen Proteinen, so genannten Fotorezeptoren, als Informations- oder Energiequelle genutzt wird. In mehreren Klassen von Fotorezeptorproteinen löst die Lichtabsorption die Isomerisierung um eine Doppelbindung im lichtempfindlichen Cofaktor aus. Im Rhodopsin startet die Isomerisierung des Retinal-Cofaktors, einer der schnellsten licht-induzierten Prozesse, verschiedene proteinspezifische Funktionen, vom Sehen und Regulation der circadianer Rhytmik bis zur Lichtenergieumwandlung und Phototaxis. Das am besten charakterisierte Rhodopsin ist Bacteriorhodopsin (bR), eine lichtaktivierte Protonenpumpe. Mit spektroskopischen Methoden wurden sowohl die mit der Isomerisierung verbundenen ultraschnellen Prozesse als auch die späteren Schritte wie die Translokation von Protonen charakterisiert. Strukturelles Wissen über die späteren Intermediate wurde hauptsächlich durch Röntgenkristallstrukturen von Tieftemperatur-stabilisiertem bR Wildtyp oder bR Mutanten bekommen, was zu einem guten Verständnis der Protonenpumpschritte beitrug. Die ultraschnellen Prozesse, die sich auf einer sub-ps- und ps-Zeitskala entwickeln, können jedoch nicht durch zeitaufgelöste Röntgenkristallographie unter Verwendung von Synchrotronstrahlung aufgelöst werden, so dass keine Strukturen der ultraschnellen bR-Intermediaten erhalten werden konnten. Dies änderte sich mit dem Aufkommen neuartiger Röntgenquellen, den Röntgen-Freie-Elektronenlaser (XFEL), die eine zeitaufgelöste Serielle femtosekunden-Kristallographie (TR-SFX) auf der sub-ps-Zeitskala ermöglichen. Dies erlaubt, die offene Frage zur Isomerisierung nicht nur spektroskopisch und quanten-mechanisch, sondern auch strukturell zu beantworten. Warum ist die Isomerisierung von Retinal in Rhodopsinen hoch bindungsspezifisch und effizient, während dies für freies Retinal in Lösung nicht der Fall ist? Beeinflusst das Protein die Isomerisierungsreaktion nicht nur sterisch, sondern auch aktiv?

Diese Arbeit verwendete TR-SFX, um Raumstrukturen der ultraschnellen Intermediate in bR zu bestimmen und dadurch die strukturellen Änderungen im Retinal und im Protein auf der sub-ps- und ps-Zeitskala zu beobachten. Große Mengen gut beugender bR-Mikrokristalle wurden in einer sehr viskosen kubischen Lipid-phase hergestellt. Zeitaufgelöste SFX-Experimente wurden vor Beginn dieser Arbeit nur mit flüssigen Proben durchgeführt. Daher mussten die Methoden zur Injektion viskoser Proben in den XFEL-Strahl speziell für dieses zeitaufgelöste Experiment angepasst werden.

Die im TR-SFX-Experiment an bR erhaltenen Kristallstrukturen machen die Torsion der isomerisierenden Doppelbindung im Retinal sichtbar. Sie zeigen auch eine oszillatorische

Bewegung im Retinal und in bestimmten Proteinresten und deren Abstände zu anderen Resten oder zu geordneten funktionell relevanten Wassermolekülen. Veränderungen der Abstände im inneren wasserstoffgebundenen Netzwerk von Wassermolekülen und Proteinresten werden ebenfalls beobachtet. Ähnlich wie bei vielen anderen TR-SFX Experimenten wurde dieses Experiment bei einer sehr hohen Pumplaser-Anregungsintensität durchgeführt, die Multiphotonenprozesse induzieren kann, was die funktionelle Interpretation der gemachten Beobachtungen kompliziert. Im Gegensatz zu anderen TR-SFX-Experimenten wird diese Einschränkung in dieser Arbeit angesprochen. Da das TR-SFX-Experiment nicht bei niedriger Laseranregungsintensität wiederholt werden konnte, wurden stattdessen zusätzliche spektroskopische und quanten-mechanische Untersuchungen durchgeführt, um mehr Einblick in Multiphotonenprozesse zu erhalten. Diese liefern in der Tat neue Erkenntnisse über Zerfallskanäle im Multiphoton-System. Es bleibt jedoch noch offen, welche Auswirkungen dies auf die Beobachtungen in den TR-SFX-Strukturen hat. Trotzdem zeigt ein Vergleich der TR-SFX Beobachtungen mit veröffentlichten spektroskopischen und quanten-mechanischen Arbeiten, die im Einphotonenbereich durchgeführt wurden, bemerkenswerte Ähnlichkeiten.

Die Erkenntnisse aus dieser Arbeit legen die Grundlagen für zukünftige TR-SFX Experimente mit optimalen Anregungsbedingungen, die den Zusammenhang zwischen den beobachteten strukturellen Veränderungen und Einphotonenprozessen erklären können. Das wird ermöglichen zu beurteilen, ob die koordinierte Bewegungen, die im Retinal, Proteinresten und Wassermolekülen beobachtet werden, Teil des Mechanismus sind, durch den das Protein die Isomerisierungsreaktion des Chromophors aktiv steuert. Darüber hinaus können die hier etablierten methodischen Fortschritte mit dem Modellsystem bR nun direkt zur Untersuchung anderer anspruchsvollerer Rhodopsine wie der neuen Familie von anionleitenden Channelrhodopsinen (ACR) angewendet werden. In dieser Arbeit wurde die Expression eines ACR-Proteins in Insektenzellen etabliert und Bedingungen für die Mikrokristallisation identifiziert. Dies ist der erste Schritt auf dem Weg zu einem zukünftigen TR-SFX-Experiment.

Publications and author contributions

Major parts of this work were published in following **research articles**:

Nass Kovacs, G., Colletier, J.-P., Grünbein, M. L., Stensitzki, T., Batyuk, A., Carbajo, S., Doak, R. B., Ehrenberg, D., Foucar, L., Gasper, R., Gorel, A., Hilpert, M., Kloos, M., Koglin, J. E., Reinstein, J., Roome, C. M., Schlesinger, R., Seaberg, M., Shoeman, R. L., Stricker, M., Boutet, S., Haacke, S., Heberle, J., Domratcheva, T., Barends, T. R. M., & Schlichting, I. **Three-dimensional view of ultrafast dynamics in photoexcited bacteriorhodopsin**. *Nat. Commun.* (under revision)

This was a highly collaborative project with following author contributions: G.N.K., R.B.D., T.D., I.S., designed the experiment; R.S. provided the purple membranes; G.N.K. purified bacteriorhodopsin; G.N.K. performed the retinal HPLC analysis; G.N.K., crystallized bacteriorhodopsin. T.S., Y.Y., K.H performed ultrafast transient UV-VIS and IR spectroscopy for which G.N.K prepared the samples; S.H. contributed to the analysis; G.N.K., M.L.G., R.L.S., M.S. and R.B.D. established the pre-illumination protocol; M.L.G., M.S., G.N.K., I.S., S.H., analysed the light scattering contribution, T.R.M.B., A.B., S.B., S.C., R.B.D., L.F., A.G., M.L.G., M.H., M.K., J.E.K., G.N.K., C.M.R., R.G.S., M.S., I.S., R.L.S. collected the SFX data; M.H., C.M.R., L. F. processed the SFX data; J.P.C., T.R.M.B. analysed the SFX data; G.N.K., J.-P.C., T.R.M.B. interpreted the electron densities; G.N.K., J.P.C., T.R.M.B., I.S. analysed the structures; T.D. performed quantum chemistry calculation; J.R., S.H., J.H. contributed discussions; G.N.K. and I.S. wrote the manuscript with input from all authors.

Kovacsova, G., Grünbein, M. L., Kloos, M., Barends, T. R. M., Schlesinger, R., Heberle, J., Kabsch, W., Shoeman, R. L., Doak, R. B., & Schlichting, I. (**2017**). **Viscous hydrophilic injection matrices for serial crystallography**. *IUCrJ, 4*(4). doi:10.1107/S2052252517005140

Review article:

Grünbein, M. L., & Nass Kovacs, G. (2019). **Sample delivery for serial crystallography at free-electron lasers and synchrotrons**. *Acta Cryst. D*75, doi:10.1107/S205979831801567X.

Parts taken from these publications and used in this thesis were written by myself. Figures and tables were taken from these open-access publications were prepared by myself unless stated otherwise. The supervisor of this work, Prof. Dr. Ilme Schlichting, herewith confirms this

Heidelberg,

Ilme Schlichting

Other publications:

Doak, R. B., Kovacs, G. N., Gorel, A., Foucar, L., Barends, T. R. M., Grunbein, M. L., Hilpert, M., Kloos, M., Roome, C. M., Shoeman, R. L., Stricker, M., Tono, K., You, D., Ueda, K., Sherrell, D. A., Owen, R. L. & Schlichting, I. (**2018**). **Crystallography on a chip-without a chip.** *Acta Cryst. D* **74**, 1000-1007

Grünbein, M. L., Bielecki, J., Gorel, A., Stricker, M., Bean, R., Cammarata, M., Dorner, K., Frohlich, L., Hartmann, E., Hauf, S., Hilpert, M., Kim, Y., Kloos, M., Letrun, R., Messerschmidt, M., Mills, G., Kovacs, G. N., Ramilli, M., Roome, C. M., Sato, T., Scholz, M., Sliwa, M., Sztuk-Dambietz, J., Weik, M., Weinhausen, B., Al-Qudami, N., Boukhelef, D., Brockhauser, S., Ehsan, W., Emons, M., Esenov, S., Fangohr, H., Kaukher, A., Kluyver, T., Lederer, M., Maia, L., Manetti, M., Michelat, T., Munnich, A., Pallas, F., Palmer, G., Previtali, G., Raab, N., Silenzi, A., Szuba, J., Venkatesan, S., Wrona, K., Zhu, J., Doak, R. B., Shoeman, R. L., Foucar, L., Colletier, J. P., Mancuso, A. P., Barends, T. R. M., Stan, C. A. and Schlichting, I. (**2018**). "**Megahertz data collection from protein microcrystals at an X-ray free-electron laser.**" *Nat. Commun.* 9. doi:10.1038/s41467-018-05953-4

Gorel, A., Motomura, K., Fukuzawa, H., Doak, R. B., Grünbein, M. L., Hilpert, M., Inoue, I., Kloos, M., Kovácsová, G., Nango, E., Nass, K., Roome, C. M., Shoeman, R. L., Tanaka, R., Tono, K., Joti, Y., Yabashi, M., Iwata, S., Foucar, L., Ueda, K., Barends, T. R. M., & Schlichting, I. (**2017**). **Multi-wavelength anomalous diffraction de novo phasing using a two-colour X-ray free-electron laser with wide tunability**. *Nat. Commun. 8*(1), 1170. doi: 10.1038/s41467-017-00754-7

Coquelle, N., Sliwa, M., Woodhouse, J., Schirò, G., Adam, V., Aquila, A., Barends, T. R. M., Boutet, S., Byrdin, M., Carbajo, S., De la Mora, E., Doak, R. B., Feliks, M., Fieschi, F., Foucar, L., Guillon, V., Hilpert, M., Hunter, M. S., Jakobs, S., Koglin, J. E., Kovacsova, G., Lane, T. J., Lévy, B., Liang, M., Nass, K., Ridard, J., Robinson, J. S., Roome, C. M., Ruckebusch, C., Seaberg, M., Thepaut, M., Cammarata, M., Demachy, I., Field, M., Shoeman, R. L., Bourgeois, D., Colletier, J.-P., Schlichting, I., & Weik, M. (**2017**). **Chromophore twisting in the excited state of a photoswitchable fluorescent protein captured by time-resolved serial femtosecond crystallography.** *Nat. Chem. 10*, 31. doi: 10.1038/nchem.2853

Barends, T. R. M., Foucar, L., Ardevol, A., Nass, K., Aquila, A., Botha, S., Doak, R. B., Falahati, K., Hartmann, E., Hilpert, M., Heinz, M., Hoffmann, M. C., Kofinger, J., Koglin, J. E., Kovacsova, G., Liang, M., Milathianaki, D., Lemke, H. T., Reinstein, J., Roome, C. M., Shoeman, R. L., Williams, G. J., Burghardt, I., Hummer, G., Boutet, S., & Schlichting, I. (**2015**). **Direct observation of ultrafast collective motions in CO myoglobin upon ligand dissociation**. *Science 350*(6259), 445-450. doi: 10.1126/science.aac5492

1. Introduction

Organisms from all domains of life use photoreceptors, light-sensitive proteins, to absorb visible photons for use as e.g. an energy source or carrier of information initiating intra- or intercellular signalling. Photoreceptors covalently or non-covalently bind one or more chromophores, which are small organic molecules with conjugated unsaturated bonds that are the primary site of photon absorption. One class of photoreceptors are rhodopsins with the chromophore retinal. Here, the energy contained in the absorbed visible-light photon (150-300 kJ mol^{-1}) drives isomerization of retinal about a double bond, an ubiquitous and fundamental reaction in photochemistry. In rhodopsins, this ultrafast reaction then triggers the specific physiological function of the protein. Animal rhodopsins function as G-protein-coupled receptors involved in visual and nonvisual phototransduction (visual rhodopsin[1] and e.g. extra-retinal pinopsin[2]), in the maintenance of the circadian clock (blue-light sensitive melanopsin[3]) and as photoisomerases.[4] In case of microbial rhodopsins found in *Archaea, Eubacteria,* fungi and algae, the function is light-energy conversion (e.g. proton pump bacteriorhodopsin[5], chloride pump halorhodopsin[6,7]) or signalling (e.g. sensory rhodopsin I[8,9] and II[10,11], ion channel channelrhodopsins[12-14]).[4*]

Despite little sequence identity between microbial and animal rhodopsins, they share a common architecture of seven transmembrane α-helices forming a pocket with the chromophore retinal bound covalently to the ε-amino group of a conserved lysine side chain, typically as a protonated Schiff base (PSB)[15,16] (Figure 1a,b). Retinal is a vitamin A aldehyde, a product of oxidative cleavage of the terpenoid beta-carotene. In the ground state, the active retinal configuration is all-*trans* and 11-*cis* in case of microbial and animal rhodopsins, respectively. Light excitation of the chromophore causes its isomerization from all-*trans* to 13-*cis* or from 11-*cis* to all-*trans.* This initiates large structural changes, *i.e.* helix motions, which then result in the rhodopsin-specific function, such as ion translocation, interaction with a soluble or transmembrane partner or G-protein activation.[17] In animal rhodopsins, the isomerized all-*trans* retinal does not return to its initial 11-*cis* configuration. It is "photobleached", requiring enzymatic re-isomerization. In microbial rhodopsins, however, the isomerized 13-*cis* retinal returns spontaneously back to an all-*trans* configuration at the end of the light-induced process, thus the process is a "photocycle"

[*] A synopsis of microbial rhodopsins is given in Section 6.1 in the Appendix.

(Figure 1c).[17] This spontaneous recovery and the abundance of all-trans retinal in mammalian cells have enabled the use of ion transporting microbial rhodopsins as biotechnological tools for precise spatial and temporal control of membrane potentials and intracellular cation concentrations. This new field, optogenetics,[18] has significantly impacted neuroscience by providing new ways to probe neuronal circuits. In optogenetics, microbial rhodopsins are overexpressed in targeted sections of the brain, where they are then activated by strong and precisely timed illumination in the freely moving animal.[19,20] The most efficient tools are based on channelrhodopsins, generating large light-induced currents. Cation channelrhodopsins (CCRs), used already in the seminal studies in 2005,[21] are the most frequently used depolarizing tools for neuronal excitation.[19] Neuronal inhibition, hyperpolarization, has been facilitated by the discovery of anion channelrhodopsins (ACRs) in 2015, replacing much less efficient tools based on chloride and proton pumps or CCR mutants.[14] The existence of natural ACRs was not only a breakthrough for optogenetics, but also drew a lot of attention in basic research, since both the ion selectivity and gating (open/close) mechanism in ACRs seem to be operating on different principles than in CCRs.[22,23] Thus, ACRs present a new and functionally distinct family of microbial rhodopsins.

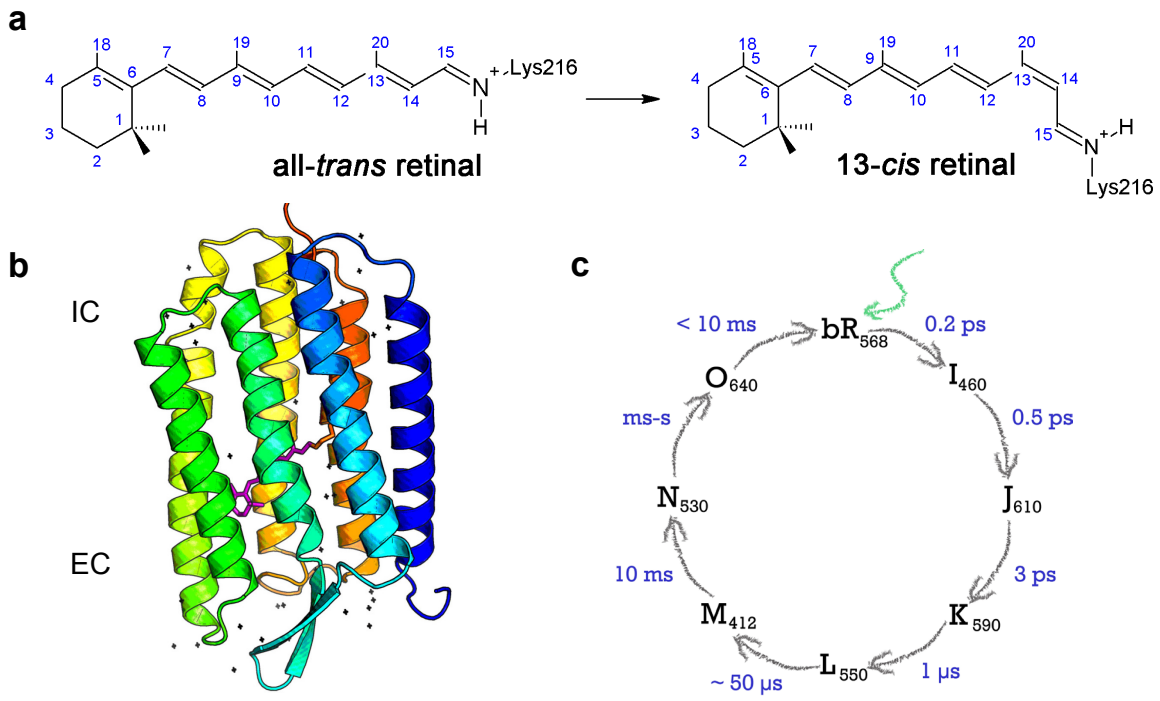

Figure 1. Rhodopsin structure and photochemistry exemplified for bacteriorhodopsin. **a**, Retinal bound to a conserved lysine as a protonated Schiff base. In microbial rhodopsins, the all-trans retinal isomerizes to 13-cis upon photon absorption. **b**, The heptahelical rhodopsin structure with covalently bound retinal (pink sticks, lysine in orange sticks). IC- intracellular side, EC – extracellular side. **c**, The absorption of a green/yellow photon (green arrow) triggers a functional photocycle encompassing several intermediate states (letters I to O). Their rise times are written in blue and the subscript of the intermediate name refers to the maximum absorption wavelength.

A general understanding of the protein-chromophore interactions that govern isomerization in rhodopsins and gaining insight about factors that determine the bond specificity and the quantum yield of the isomerization reaction is important from a fundamental point of view, given its widespread presence in photoreceptive systems. Additionally, optogenetics can benefit from this information, allowing targeted design of more powerful tools. The best understood and most studied microbial rhodopsin is bacteriorhodopsin, which was also investigated in this thesis.

1.1. Bacteriorhodopsin

Bacteriorhodopsin (bR) is the main component of purple membranes (PM), a specific membrane fraction from the archaeon *Halobium salinarum*. The PM contain about 25% lipid and 75% bR[23] present in a highly ordered 2D hexagonal lattice.[24] bR is a light-driven proton pump[25] that creates a chemiosmotic gradient for ATP synthesis.[26] Given bR's high biochemical and photochemical stability and high abundance in the PM, it quickly became an intensely studied model system with many firsts. With the aim of characterizing bR's structure and photocycle, numerous biophysical and biochemical techniques were pioneering with bR – Fourier-transform infrared spectroscopy,[27] solid state nuclear magnetic resonance,[28] various ultra-fast time-resolved spectroscopies (resonance Raman,[29] visible (VIS)[30] and infrared (IR) spectroscopy[31]) and membrane protein crystallization techniques.[32] It also became a paradigm for proton pumps, membrane proteins and light-driven-energy conversion in general.[33] bR was the first membrane protein to be sequenced, by Khorana[34], years after its alfa-helical structure spanning the membrane was determined to 6 Å resolution from electron micrographs. This was the first structure of an integral membrane protein, obtained in 1975.[35] Numerous technical improvements in electron microscopy led to a near-atomic resolution structure of bR at 3.5 Å in 1990, allowing building of all side chains.[36] This model was subsequently used for structure determination from X-ray crystallographic data of bR crystals diffracting to high resolution[37] - these could only be obtained when crystallization in lipidic cubic phase was invented, using bR.[32] Thereafter, also structures of various photocycle intermediates were determined, either by cryo-trapping of accumulating intermediates or by use of mutants accumulating specific intermediates[38] – starting with the M intermediate of a D96N mutant[39] and a low-temperature K intermediate (K_{LT})[40] followed by L[41], N[42] and O[43].

Proton pumping

This structural insight together with the wealth of spectroscopic data on bR and its intermediates accompanied by mutation studies and computational work[44] allowed to establish a picture of the proton pumping activity and its link to the photocycle. Light-adapted bR contains 100% of physiologically active all-*trans* retinal, whereas dark-adapted bR contains a ~ 50:50 mixture of all-*trans* and 13-*cis*-15-syn retinal.[45] The photon absorption in all-*trans* retinal triggers its isomerization to 13-*cis*-15-anti retinal and this process is complete in the red-shifted K intermediate appearing within ~ 3 ps at room temperature.[46] The now disordered water Wat402 is not stabilizing the PSB anymore and the pK_A of PSB and Asp85 decreases and increases,[47] respectively (in the ground state the pK_A of PSB is 11 units higher than that of Asp85[48,49]). As a consequence, PSB donates a proton to Asp85 (step 1, Figure 2) during the L to M transition.[50] This primary proton transfer breaks the hydrogen-bonding network extending to Arg82 and Arg82 turns to the extracellular side (step 2). It pushes a proton from a protonated water cluster (not visible in X-ray structures) to the proton release complex formed by Glu194/Glu204.[51] A unidirectional gate at Ser193 is opened, ultimately releasing a proton to the extracellular side (step 3).[52] This initiates large structural rearrangements opening the cytoplasmic side (CP) of the protein and marks a spectroscopically silent transition from M_1 (early M) to M_2 (late M) on a sub-ms timescale.[38] These rearrangements ensure unidirectionality of the proton-pumping in two ways – (i) the CP is open only after proton ejection to the extracellular; (ii) the structural changes lead to a decrease of the pK_A of Asp96,[53] which reprotonates the Schiff base (step 4), marking a transition from M_2 to N. During the lifetime of N Asp96 is reprotonated from the cytosol (step 5) and retinal reisomerizes, yielding an all-*trans* configuration in O. The last step is the reprotonation of the water cluster near the proton release site by Asp85 and the photocycle is completed by restoration of the ground state.[54] These findings are also supported by mutation studies showing a strongly perturbed pumping activity in D85A, D85N, D212N, R82Q mutants, where the D85N and D85A mutants are completely inactive in proton pumping.[55]

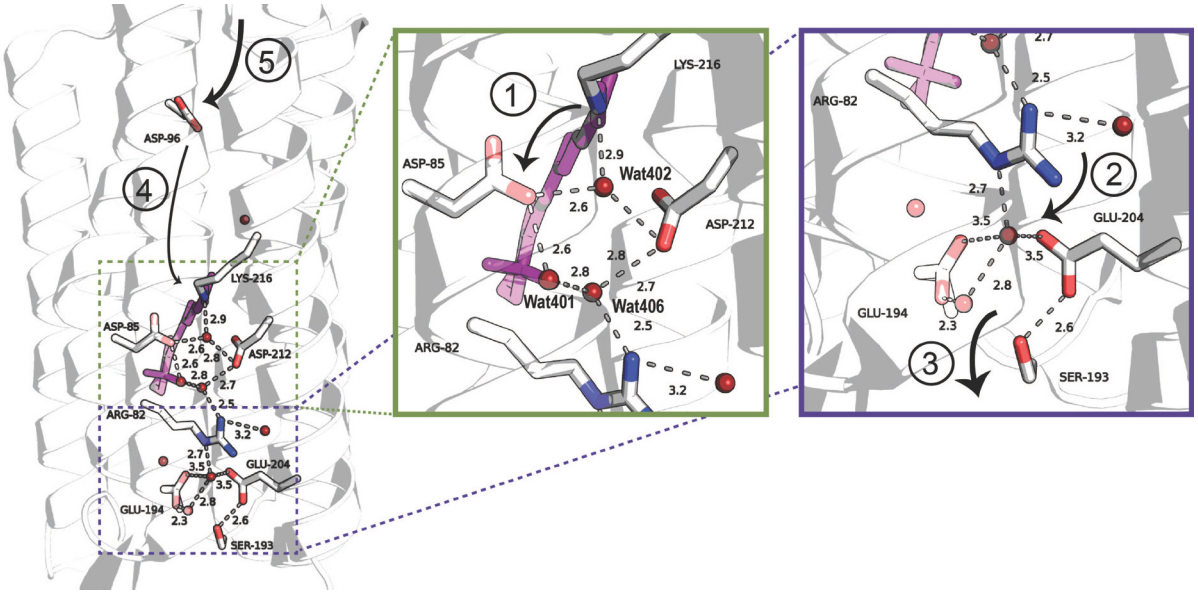

Figure 2. Proton pumping in bR. Residues and crystallographic waters involved in proton pumping connected by hydrogen bonds are shown (numbers refer to distances in Å). The green inset shows the pentagonal cluster (Wat402, Wat401, Wat406, Asp85 and Asp212) around the Schiff base and the violet inset shows the extracellular proton release site. The black arrows illustrate the proton transfer steps 1-5 as described in the text. Retinal is shown as purple sticks and waters as red spheres. Coordinates 1C3W were used to make this figure, inspired by Fig.1 in[54].

Retinal isomerization and other ultrafast events

While there is largely consensus on the proton transfer steps happening on the μs – ms timescale, the initial ultrafast steps after photon absorption by the chromophore are not so clearly understood. The ultrafast time domain could only be studied spectroscopically until very recently and no structures of the ultrafast intermediates are available. The ultrafast intermediates are:[56]

$$bR \rightarrow H\ (200\ fs) \rightarrow I_{460}\ (500\ fs) \rightarrow J_{610}\ (3\ ps) \rightarrow K_{590}$$

Retinal absorbs a photon and an electron from the highest occupied molecular orbital (HOMO) is promoted to the lowest unoccupied orbital (LUMO), exciting the molecule to the Franck-Condon region (H). Due to this excitation, a large change in the dipole moment (~10 D) immediately occurs in the all-*trans* retinal PSB[57,58] as the positive charge shifts from the PSB to the β-ionone ring.[59] The electronic change, a redistribution of charges, sets the nuclear positions of retinal atoms in motion by first reducing the double bond order,[60] where single bonds become shorter and double bonds become longer (the average of the difference in bond lengths of adjacent carbon-carbon bonds in a $(CH)_n$ chain is called bond length alternation).[61] The decay of H and rise of the fluorescent excited state I[62] is accompanied by the activation of high frequency stretching modes (~1650 – 1000 cm^{-1}; C=N stretch, ethylenic

C=C stretch, C-C stretch, methyl rocking).[56,61,63-65] Also lower frequency modes such as hydrogen-out-of-plane (HOOP, ~950 cm^{-1}) modes are activated[65] and torsional modes of even lower frequencies (~100 – 200 cm^{-1}) manifested as modulations of optical traces were observed on the sub-ps timescale, in bR and several other microbial rhodopsin.[66,67] Torsion around the C_{13}=C_{14} bond occurs with the rise of the J intermediate, an isomerized ground state photoproduct. The isomerization time constant of ~0.5 ps can be derived from the rise of the ethylenic band at ~1517 cm^{-1} in transient vibrational spectroscopy[65,68] and from the decay of the excited state I and rise of red-shifted J in transient optical spectroscopy.[30,69,70] The photoisomerization itself proceeds as immediate "flipping" since it occurs through a multidimensional conical intersection, which is a hypersurface where the S_1 excited state and S_0 ground state potential energy surfaces intercept.[71] In the crowded environment of the binding pocket, twisting of neighbouring double bonds was computationally predicted to facilitate a minimal volume isomerization.[72] The J-state is a highly twisted and vibrationally hot (unrelaxed) state that cools and relaxes during the transition to K.[73] During the lifetime of K, the retinal restores the original planarity and major conformational relaxation occurs on the ns time-scale, finally marking the end of the isomerization process.[74]

The sudden polarization (charge translocation) in retinal occurring immediately after photon absorption was predicted to change the electrostatic interactions with the protein.[60,75] This ultrafast dielectric response of the protein could indeed be observed experimentally[76] and computationally.[77] Specifically, changes in the amide I and amide II region on the sub-ps and ps-timescale were ascribed to polarization induced protein alterations[78] and these precede the isomerization reaction.[79] Both the charge translocation and the electrostatic protein response were also traced by near-UV absorption changes of Trp86 positioned next to retinal.[80,81] These absorption changes rise instantly and decay with the rise of the isomerized photoproduct, further supporting the role of the by charge translocation altered retinal-protein interactions in the isomerization process.[80,82] Yet, the mechanism by which the retinal photoreaction propagates into the protein remains unclear.

The photoisomerization in bR produces only the 13-*cis* retinal configuration and the quantum yield of the reaction is about 0.67, hence about 2/3 of the molecules forms the photoproduct J and 1/3 returns to the all-*trans* bR ground state.[83] This is in strong contrast to the photochemistry of a retinal PSB free in solution – all-*trans* retinal will isomerize significantly slower (~2 ps)[84] with a 2-3 lower quantum yield and primarily to 11-*cis,* but also 9- and 13-*cis*.[85] Clearly, the protein modulates the isomerization reaction. On the one hand, the highly confined protein binding pocket sterically limits the range of motion (Figure 3). This passive role explains the bond specificity, but not the dramatically increased quantum yield. On the other hand, an active role of the protein in guiding the reaction is suggestive – and as outlined above, ultrafast protein motion preceding the isomerization reaction has

been observed already. The possibility of an active protein contribution may be investigated by analysing structures of the ultrafast intermediates. Until recently, these were impossible to obtain due to the inaccessibility of <100 ps time-delays in time-resolved crystallographic experiments.[86] However, the advent of novel X-ray sources, the X-ray free-electron lasers, enables such experiments with a time-resolution down to sub-ps time-delays possible. A study investigating the ns-ms intermediates of bR has been recently performed at the X ray free-electron laser in Japan, showing an relaxed isomerized retinal and larger structural changes .[87]

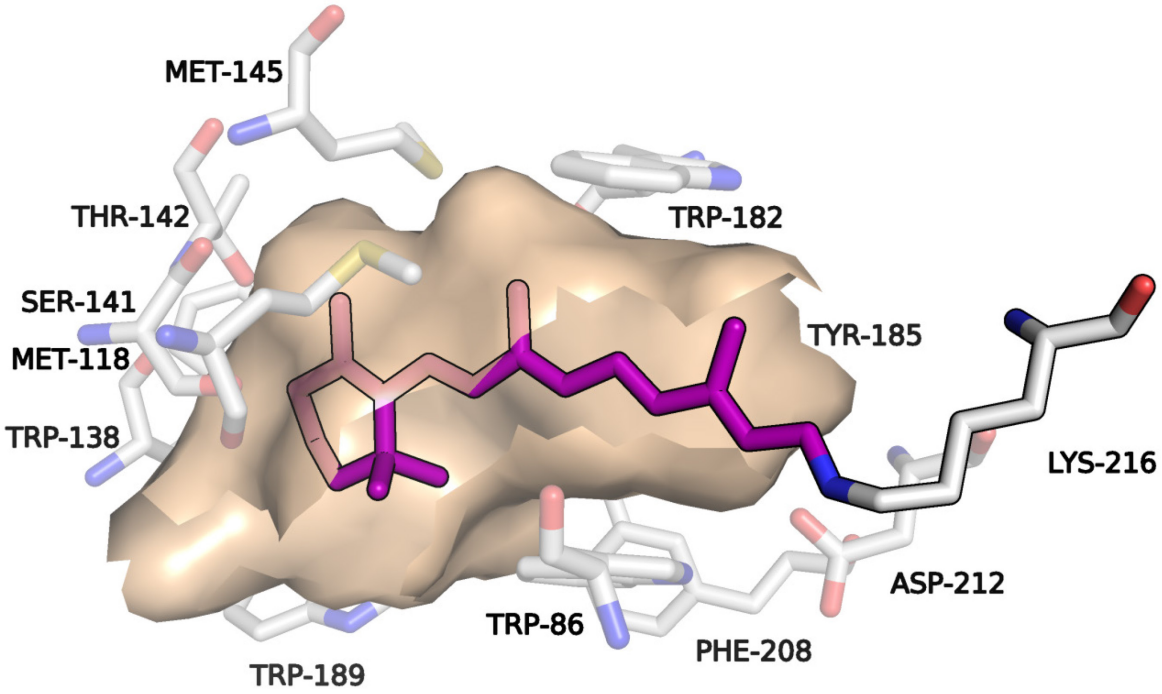

Figure 3. Retinal binding pocket in bR. Retinal is shown as purple sticks and the sufrace of residues lining the pocket is shown in beige. Bulky aromatic residues confine the space aroung retinal, in particular Tyr185 (only the surface visible) is known to sterically limit retinal motion.[88]

1.2. Serial femtosecond crystallography

X-ray free-electron lasers (XFELs) are novel X-ray sources with unprecedented properties that enable novel research in a variety of scientific fields.[89] An XFEL delivers as many photons in a single pulse (fs duration) as a 3rd generation synchrotron source in an entire second. Moreover the radiation is highly coherent.[90] For macromolecular crystallography, this 10^9–fold increase in peak brilliance means that high-resolution diffraction patterns can be collected from weakly diffracting objects such as tiny protein crystals,[91,92] including those of membrane protein crystals.[93] Importantly, the ultrashort pulse duration allows a diffraction pattern to be collected before significant manifestation of radiation damage, even at room temperature.[94,95] Thus essentially damage-free data can be obtained even of radiation-sensitive samples.[96,97] This is particularly important in the case of rhodopsins, since radiation damage can induce structural changes around the retinal, leading to misinterpretation.[98] XFELs also facilitate time-resolved (TR) measurements, including studies of irreversible reactions.[87,99-101] The short pulse duration enables temporal resolution down to the sub-ps range.[102-104] Also, the ability to use small crystals is crucial for both optically- or chemically-triggered reactions. Optical absorbance in a protein crystal is high due to the high protein concentration, and this limits optical penetration to a few μm.[102] Similarly, diffusion of chemicals into crystals is often the limiting step for triggering, with smaller crystals giving proportionally shorter diffusion times.[105]

However, the high intensity of the X-ray pulses also complicates data collection, since the pulse ultimately destroys the exposed sample (formation of a diffraction pattern prior to this destruction has been dubbed "diffraction before destruction"[95]). Consequently a fresh crystal (or crystal section) must be supplied for each exposure. These come at up to 120 Hz at the low-repetition rate first-generation XFELs, whereas MHz-repetition rates can be achieved at newer XFEL sources.[106-108] A serial approach to data collection, termed serial femtosecond crystallography (SFX), becomes mandatory.[109] SFX imposes unique challenges on all aspects of the experiment – from sample preparation, to sample delivery and to data acquisition and analysis.

In most SFX experiments, homogeneously-sized and well-diffracting microcrystals are required in large quantities. Thus, the crystallization process needs to be well optimized and understood in order to reproducibly yield the desired crystals. For proteins (same applies to DNA and RNA) that are crystallized from supersaturated protein and precipitant solutions, batch crystallization using seeding may be applied.[110] "Seeds" are prepared by crushing initial crystals and these crystallization nuclei are then added to subsequent crystallization set-ups, which ensures homogeneity and allows controlling crystal size (the more seeds, the smaller the crystals). Many membrane proteins are, however, crystallized in lipidic cubic phase

(LCP). LCP is a bicontinuous system of lipid bilayers obtained by mixing specific monoacyl glycerols (MAGs, most commonly monoolein, MAG 9.9) with aqueous solutions at specific ratios.[111] For crystallization, the target protein is reconstituted in these lipid bilayers and addition of precipitants drives crystal formation.[112] For SFX experiments, crystallization conditions need to be optimized for large-scale crystallization set-ups in gas-tight containers, such as glass syringes or plastic tubes.[87,113] The scaling-up step from the geometry yielding few initial well-diffracting crystals to one yielding thousands of well-diffracting is challenging and may not always work (see Appendix 6.2).

1.2.1. Sample delivery for serial crystallography

Various approaches have been developed for delivering crystalline samples serially to the interaction region with the XFEL beam. The most established technique is injection, where an injector is used to attain a liquid jet or viscous stream from samples of low or high viscosity, respectively. A liquid jet is produced by a gas-dynamic virtual nozzle (GDVN),[114,115] where the aqueous sample suspension exiting the inner capillary (50 – 100 µm inner diameter) is focussed by a fast flowing sheath gas in the outer capillary to a microscopic jet of typically 3-5 µm in diameter flowing at 10-50 m/s.[116] Relatively high sample flow rates are needed to maintain a stable jet, thus the sample consumption is rather high at low X-ray repetition rate XFELs, since the majority of the sample is not probed by the X-ray pulses. At MHz X-ray repetition rate XFELs, the sample is probed much more frequently, which significantly reduces the sample quantity required for a data set. However, MHz data collection requires that the sample is replenished at a much faster rate, which was so far only accomplished with very fast liquid jets flowing at ~ 100 m/s.[117,118] At the low X-ray repetition rate XFELs, the required sample quantities can be dramatically reduced by using high viscosity extrusion (HVE) to produce a slowly flowing viscous stream (Figure 4a). This can be either employed for samples that are naturally viscous, e.g. LCP-grown crystals, or for scarcely available crystals grown in solution, which are then embedded into a viscous carrier matrix. Beside injection, high-throughput serial sample delivery can be also achieved with fixed-target approaches, where crystals are immobilized on a substrate in special features or just randomly distributed on the support which is then scanned by the X-ray beam.[119-122] A general overview of properties of these three sample delivery method groups is presented in Table 1. Further, a number of other methods evolved, such as goniometer-based approaches[123,124] or pulsed droplet ejection.[125-127]

Additionally, some of these sample delivery techniques have been ported to synchrotrons. Here, serial data collection approaches are particularly useful, as they spread the radiation dose across numerous separate crystals and thereby reduce radiation damage, allowing e.g. room temperature data collection. Serial data collection will be even more advantageous at

next-generation synchrotrons, diffraction-limited storage rings (DLSRs)[128]. Numerous existing synchrotrons are upgrading to DLSRs, e.g.: Swiss Light Source (SLS)-II,[129] European Synchrotron Radiation Facility-Extra Brilliant Source in Grenoble,[130] PETRA IV in Hamburg,[131] Spring-8 in Japan[132] and new DLSRs were constructed in Lund, SE (Max IV) and Argentina (Sirius). Compared to current synchrotrons, they offer radiation with significantly higher brightness and coherence. This will enable measurements from even smaller crystals, which require serial data collection to minimize radiation damage. SFX-derived sample delivery techniques can be employed, as they enable convenient high-throughput collection of diffraction patterns from hundreds or thousands of small crystals at room[133-138] or cryogenic[139] temperatures. TR measurements including those of irreversible reactions, similarly to TR-SFX, can also be performed, albeit with lower time-resolution. From the injection techniques, HVE is particularly suitable due to the low velocity of the extruded streams, as demonstrated at several synchrotrons.[133,134,137,138]

Table 1. General properties of different types of sample delivery techniques.

Parameters	Liquid jets	Viscous jets	Fixed targets
sample translation speed	~ 10-100 m s^{-1}	up to several mm s^{-1}	defined by motors
jet diameter	≤ 5 µm	defined by the capillary ID (e.g. 50, 75, 100 µm)	N/A
flow rate	~5 - 50 µL min^{-1}	tens of nL to several µL min^{-1}	N/A
X-ray background	generally low	matrix-dependant	design- and sample thickness- dependant
suitable crystal size	≤ ~10 µm	< capillary ID	if features: feature-dependant; no features: any size
sample consumption	X-ray rep. rate dependant (mg to sub-g)	sub-mg possible*	sub-mg possible*
sample efficiency at ≤120 Hz XFELs at MHz XFELs	 low high	 high unfeasible	 high high
X-ray efficiency at ≤ 120 Hz XFELs at MHz XFELs	 high high	 high rep. rate decrease necessary	 high motor-speed dependant#
achievable TR with optical triggering	≤ few µs	≤ several s	Unrestricted**
suitability for mixing	yes	no	being explored
suitability for synchrotron use	currently not##	yes	yes

* Optically triggered TR experiments require more sample since not only the X-ray affected section, but the entire optically illuminated section of the jet needs to be displaced between the exposures.
# If the translation motors can be fast enough, MHz operation is possible, otherwise the rep. rate has to be decreased.
** For irreversible reactions, unwanted illumination of large chip sections has to be mitigated in order to make efficient use of the chip.
May be feasible at diffraction limited storage rings with high brilliance (µm-sized focus, µs exposure time). The exposure must be short enough to capture the fast moving crystal as essentially "still" and contain sufficient photons for high resolution diffraction.
This table was published in Grünbein & Nass Kovacs, 2019.[140]

Viscous matrices for high viscosity extrusion (HVE)

The suitability of HVE for serial crystallography strongly depends on the viscous matrix in which macromolecular crystals are immersed. Consequently a suitable HVE matrix must fulfil a number of requirements. First, it must have the viscosity and flow properties needed to form a stable stream when injected. Secondly, it must be inert to or compatible with the crystals and their mother liquor. Third, it must neither affect the diffraction properties of the crystals nor produce strong X-ray background by itself, as the stream is invariably much thicker than the crystals it carries. Ideally, it should also be compatible with injection into both atmospheric pressure and vacuum to be applicable to all XFEL diffraction chambers. To date, several such matrices have been identified. They fulfil these requirements to varying extents, usually depending on their chemical nature – whether it is the lipid bilayer forming LCP or a hydrophilic or hydrophobic system. The requirement of stable injection properties is not only important for reliable delivery of pristine sample for each X-ray exposure, but is essential for time-resolved experiments, where larger sections illuminated by the pump laser need to be cleared (Figure 4b-e).

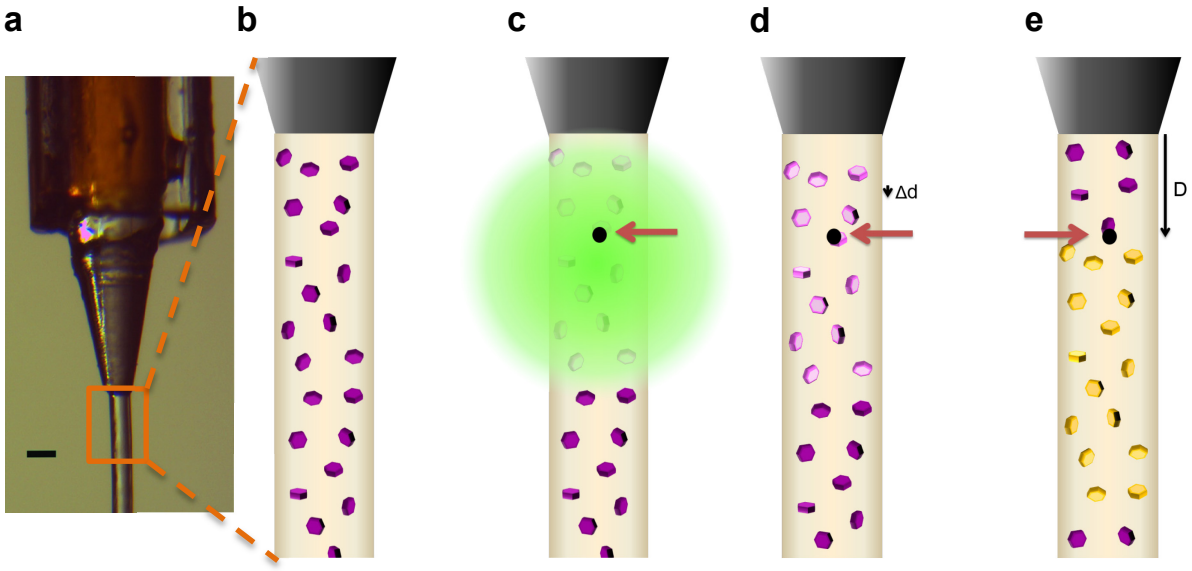

Figure 4. High viscosity extrusion. a, A HVE nozzle. A viscous stream is extruded from the inner coned capillary, while gas is flowing in the outer square glass capillary. The scale bar represents 100 µm. **b-e**, Schematics of the time-course of a time-resolved optically triggered SFX experiment. The running stream containing purple hexagonal crystals (**b**) is illuminated by an optical pump (green) which photo-activates the crystals (shown as pink, **c**). **d**, After the desired time-delay Δt, the crystals are probed by the X-rays (red arrow pointing to the black interaction spot). During Δt, the jet advances by Δd. This is negligible for ultrafast experiments, but has to be considered for longer (ms) time-delays. **e**, For the next X-ray exposure, the initially photoactivated (now yellow) crystals need to be displaced by at least the distance D so that fresh crystals are present for the next exposure, disregarding whether it is a pumped or unpumped snapshot (the image shows a situation with unpumped crystals). Panel **a** was published in Grünbein & Nass Kovacs, 2019.[140]

1.3. Aim of this work

Rhodopsins are capable of efficiently channelling the energy of the absorbed photon into protein structural changes, thereby executing their biological function. The first step in the process is retinal photo-isomerization around a double bond, initiating structural changes that allow - depending on function - protons, but also larger ions, such as chloride ions, to translocate through the protein to the other side of the membrane. Despite a large body of rhodopsin research, until recently many mechanistic questions requiring structures of intermediates could not be addressed due to technical limitations.

The mechanism of the widespread photo-isomerization around a double bond and the factors affecting it pose a fundamental open question in photobiology and photochemistry. The isomerization of retinal bound to opsin is highly efficient and bond-specific – which is in contrast to the inefficient and unspecific isomerization of the free retinal in solution. The aim of this work had been to investigate the role of the protein in this ultrafast process.

This question was to be addressed primarily by obtaining time-resolved crystallographic structures of the sub-ps and ps events following photon absorption in bacteriorhodopsin. This would provide insight into:

- The structural changes in the retinal evolving before and during the isomerization. These could so far only be inferred from spectroscopic measurements.
- The structural changes occurring in specific protein residues. Ultrafast changes in the protein have been observed spectroscopically, but could not be assigned to specific residues.
- The movement or disorder of structured water molecules that participate in the proton pumping steps at the μs-ms timescale. Weakening of hydrogen bonds had been observed spectroscopically before, but information on distance changes was missing.

It should be possible to obtain these structures using time-resolved serial femtosecond crystallography. This is an emerging and thus a technically still evolving method. At the start of this thesis, no time-resolved SFX experiments had been performed on protein crystals in LCP. Thus, specifically for this experiment, the following technical challenges needed to be addressed:

- Large quantities of bR microcrystals grown in LCP and diffracting to a high resolution needed to be reproducibly prepared
- Reliable HVE injection conditions ensuring a stable stream velocity needed to be established for the TR-SFX experiment

    - This involved identifying viscous matrices that can be added to LCP to stabilize the stream velocity. These could be also used on their own as carriers of crystals grown in supersaturated solutions, enabling sample-efficient HVE injection for these systems.
- An efficient protocol for light-adaptation of the microcrystals perfectly compatible with all boundary conditions of the SFX experiment needed to be designed and implemented

To know whether the isomerization reaction proceeds in the bR microcrystals on a similar timescale as in the purple membranes, which would allow relating our results to the large body of literature, ultrafast transient IR and VIS spectroscopy was to be employed to measure the ultrafast intermediates. This is technically highly challenging and had not been done for bR crystals yet (and neither for any other LCP-grown crystals), as crystals are optically thick and scatter light strongly. This had to be addressed by developing a dedicated sample preparations protocol and the measurements were to be performed in collaboration with Karsten's Heyne group at Freie Universität Berlin, including Till Stensitzki and Yang Yang.

Further, these experimental results were to be interpreted in light of quantum mechanical (QM) calculations performed by Tatiana Domratcheva (our department). This would provide a theoretical framework for possible interpretations of the origin of the observed structural changes. Also, especially when the crystallographic density is not sufficiently well defined to allow for only one chromophore model, fitting the density with computed energetically optimized structures can provide further clues about likely conformations.

This interdisciplinary study should provide unpreceded insight into the means by which protein controls the cofactor's ultrafast photochemistry. Further, the technical advances established using the model system bacteriorhodopsin may then be applied to study new classes of retinal proteins, such as ACRs. Here, structures of both the ultrafast and ms-intemediates would provide valuable information on ion selectivity and channel gating. Therefore, the expression, purification and crystallization of ACRs was to be explored in this thesis, with the aim of a TR-SFX experiment in the future.

2. Materials and Methods

2.1. Materials

Products used in this work with their respective suppliers are listed in the tables below. Table 2 lists the chemicals and enzymes, Table 3 consumables and crystallization screens, Table 4 buffers and growth media and Table 5 the equipment used in this work.

Ultrapure water from ELGA PURELAB Ultra system (ELGA LabWater, Veolia Water Technologies, Celle) was used for preparations of aqueous solutions.

Table 2. Chemicals and Enzymes grouped by their manufacturer/supplier.

Product	Manufacturer/ Supplier
all-*trans* retinal, ampicillin sodium salt, APS, Bis-Tris, EDTA, glacial acetic acid, HEPES, imidazole, methanol (LC-MS grade), MES, PEG 2000, PEG 550 MME sucrose, TEMED, Tris	Sigma-Aldrich (Steinheim, Germany)
$CaCl_2$, HCl_{aq}, KCl, KOH_{aq}, KOH_s, K_2HPO_4, KH_2PO_4, methanol, $MgCl_2$, Na_2HPO_4, NaH_2PO_4, NaCl, $NaOH_{aq}$, $(NH_4)_2SO_4$, isopropanol, sodium acetate	Merck (Dramstadt, Germany)
DTE, DTT, EDTA, glycerol, IPTG, urea	GERBU (Heidelberg, Germany)
Bacto agar, Bacto tryptone, Bacto yeast extract, agar	Becton Dickinson Biosciences (Heidelberg, Germany)
Agarose, bromophenol blue, SDS	Serva (Heidelberg, Germany)
GelRed nucleic acid stain	Biotium (Hayward, CA, USA)
GeneRuler 1kb DNA ladder, PageRuler Prestained Protein ladder, InVision™ His-Tag In-Gel Stain, Sf-900 III SFM (insect cell medium), *Aat*I restriction enzyme	Thermo Fisher Scinetific (Waltham, MA, USA)
InstantBlue (coomassie stain)	Expedeon (Over, UK)
cOmplete EDTA-free protease inhibitor	Roche Diagnostics (Mannheim, Germany)
ProtoGel (acrylamide : bis-acrylamide 37.5:1, 30% in H_2O)	National Diagnostics (Atlanta, GA, USA)
DDM (Sol-grade and anagrade), DM (anagrade), OG (sol-grade and anagrade)	Anatrace (Maumee, OH, USA)
DDM (>99% and >99.5%), OG (>99% and >99.5%)	Glycon (Luckenwalde, Germany)
Monoolein	Nu-Chek Prep (Elysian, MN, USA)
MAG 7.7., MAG 7.9	Avanti Polar Lipids (Alabaster, AL, USA)
Enzymes and related reagents:	

In-Fusion HD Cloning Kit CloneAmp™ HiFi PCR Premix Stellar™ Competent Cells	Clontech/ Takara (Saint-Germain-en-Laye, France)
*Eco*RV, *Eco*NI, *Bam*HI, *Nco*I CutSmart buffer	New England Biolands (Ipswich, MA, USA)
TEV Protease	provided by Kerstin Anikó Seifert or Elisabeth Hartmann in the department

Table 3. Consumables and crystallization screens grouped by their manufacturer/supplier.

Product	Manufacturer/ Supplier
Amicon Ultra centrifugal filter units (MWCO: 30, 50 and 100 kDa), Ultrafree centrifugal filter units (pore size 5.0 µm)	Merck Millipore (Darmstadt, Germany)
Baysilone Paste, mittelviskos	Bayer AG, Leverkusen, Germany
BD Plastipak disposable syringes with Luer lock	Becton Dickinson, Heidelberg, Germany
Centrifugal tubes 15 mL and 50 mL	Sarstedt, Nümbrecht, Germany
CrystalQuick™ LP Plates, 96 wells	Greiner Bio-One (Kremsmünster, Austria)
Dialysis tubing (MWCO:12-14 kDa)	neoLab (Heidelberg, Germany)
Gas-tight syringes, volumes 100 µL (1710 RN) and 250 µL (1725 RN)	Hamilton (Bonaduz, Switzerland)
HisPur Ni-NTA agarose resin	Thermo Fisher Scientific (Waltham, MA, USA)
LCP Sandwich Set	Marienfeld (Lauda-Königshofen Germany)
Qiagen plasmid Mini and Midi Kit	Qiagen (Hilden, Germany)
PD-10 desalting columns	GE Healthcare, Uppsala, Sweden
Reaction Tubes (0.5, 1.5, 2.0 mL)	Eppendorf (Hamburg, Germany)
SuperClear™ Plates, 24-well	CrystalGen (Commack, NY, USA)
Syringe Filters (0.22 µm, 0.45 µm), Serological Pipets	TPP Techno Plastic Products, Trasadingen, CH
Wizzard® Plus SV Miniprep DNA Pur System	Promega (Madison, WI, USA)
Crystallization screens:	
JCSG Core I, II, III, IV Suite, PEG, Classics, $AmSO_4$ Suite, Cubic Phase I and II Suite	Qiagen (Hilden, Germany)
Wizard™ I and II	Emerald (Bainbridge Island, WA, USA)
Additive Screens, Detergent Screens	Hampton Research (Alison Viejo, CA, USA)
MemMeso™, PGA Screen™, MemGold™, MemGold2™	Molecular Dimensions (Suffolk, UK)

Table 4. Composition of microbial growth media and buffers which were in-house prepared. The growth media were prepared by the institute's media kitchen. TAE and Laemmli buffer and the SDS loading dye were prepared by technicians of the department.

Name	Composition
LB medium	10 g/L tryptone 5 g/L yeast extract 10 g/L NaCl pH 7.0
LB-Agar	25 g/L Standard-I 15 g/L agar
TAE buffer	40 mM Tris 20 mM acetic acid 1 mM EDTA
Laemmli buffer	25 mM Tris/HCl pH 8.0 200 mM glycine 0.1 % (*w/v*) SDS
4 × SDS loading dye	25 mM Tris/HCl pH 6.8 400 mM DTE 8.2 % (*w/v*) SDS 40 % (*w/v*) glycerol 0.1 % (*w/v*) bromophenol blue

Table 5 Equipment

Product	Manufacturer/ Supplier
Äkta Purifier FPLC System, HiLoad™ 16/600 Superdex™ 75 pg, Superose™ 6 10/300 GL	GE Healthcare (Uppsala, Sweden)
BRANSON Sonifier 250 and W-450	G. Heinemann Ultraschall- und Labortechnik (Schwäbisch Gmünd, Germany)
Centrifuges and rotors	Eppendorf (Hamburg, Germany) Beckman Coulter Inc. (Palo Alto, USA) Sorvall/Kendro Laboratory Products (Langenselbold, Germany)
ChemiDoc™ MP CCD detection system, Power Pac 300 electrophoresis power supply	Bio-Rad (Hercules, CA, USA)
CrystalCap Magnetic Ported Mounted Cryo Loops	Hampton Research (Alison Viejo, CA, USA)
ELGA-Purelab ultra system	ELGA LabWater (Celle, Germany)
Heraeus B6 microbial incubator	Kendro laboratory products, (Newtown, CT, USA)
INFORS Multitron Pro Shakers	INFORS HT (Bottmingen, Switzerland)
Luna-II™ Automated Cell Counter, Counting Slides and	Logos Biosystems, Villeneuve d'Ascq, France

Trypan Blue Stain	
Microfluidizer M110-S	Microfluidics (Newton, MA, USA)
Modular Flake-Ice Machine MF36	Scotsman Europe (Pogliano, Italy)
Mosquito® nanolitre pipettor	TTP LabTech Ltd. (Melbourne, UK)
NanoDrop ND-1000 Spectrophotometer	NanoDrop Technologies, Thermo Fisher Scientific
Olympus CX 41 microscope	Olympus Deutschland GmbH, (Hamburg, Germany)
Pipetman P pipettes (P2, P10, P20, P100, P200, P1000)	Gilson (Limburg-Offheim, Germany)
ProgResR C3 microscope camera	Jenoptik AG (Jena, Germany)
PTC-200 DNA Engine® thermocycler	MJ Research Inc. (Waltham, MA, USA)
Rock Imager®	Formulatrix (Bradford, USA)
Stereomicroscope Leica MZ 16	Leica Mikrosysteme GmbH (Wetzlar, Germany)
Thermomixer®, New Brunswick™ Innova® 44 Shakers	Eppendorf GmBH (Wesseling-Berzdorf, Germany)

2.2. Molecular biology methods

2.2.1. Ligation-independent cloning of ACR constructs

Genes encoding full-length proteins ACR1 (111593, 438 aa) and ACR2 (146828, 438 aa) were codon optimized for the insect cell line *Spotoptera frugiperda* and synthesized by GeneArt (Thermo Fisher Scientific, Waltham, MA, USA) and supplied in the pMK-RQ and pMA-T cloning vectors, respectively. The dual-purpose vector pIEx/Bac™ for protein expression in *Spodoptera*-derived insect cells by transient transfection or by generation of baculovirus recombinants was obtained from Miroslaw Tarnawski, who already cloned GFP as a N- or C-terminal fusion protein flanked with a tobacco etch virus (TEV) cleavage site and 10 × His-Tag into the vector (pIEx/Bac-1-CGFP and pIEx/Bac-1-NGFP). ACR1 and ACR2 were subcloned into these vectors as full-length genes and C-terminally truncated variants (295 aa and 291 aa resp.)[14] with GFP at the N- or C-terminus using In-Fusion® HD Cloning Kit (Taraka Bio USA, Inc., Mountain View, USA), following manufacturer's instructions and yielding eight different constructs schematically shown inFigure 5.

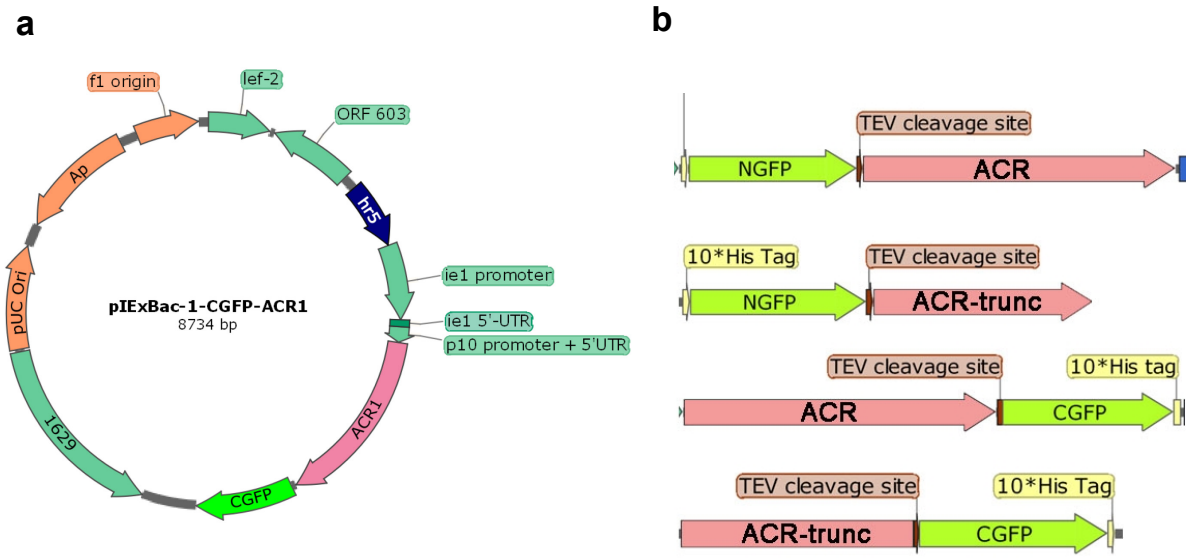

Figure 5. a, ACR1 and ACR2 genes in the pIExBAC-1 vector (example CGFP-ACR1). b, Schematics of the 4 constructs of each ACR used for expression tests - ACR1 and ACR2 full-length and truncated versions connected via a TEV cleavage site to an N or C terminal GFP fusion flanked with a 10 × His-tag

Oligonucleotides (Table 6) for the amplification via polymerase chain reaction (PCR) were generated using the Primer Design tool for In-Fusion® HD Cloning and synthetized by Eurofins MWG Operon (Ebersberg, Germany).

Table 6. Oligonucleotides used for amplification of the vectors and genes

Code	Name	Sequence
C	VEC_CGFP_FW*	GGATCCGAGAACCTGTACTT
Ca	VEC_CGFP_RV*	GGATTGTAAATAAAATGTAA
N	VEC_NGFP_FW*	TAAGTGATTAACCTCAGGTTATACA
Na	VEC_NGFP_RV*	GGCACCTTGGAAGTACAGGT
1	CGFP_ACR1_FW	ttttatttacaatccATGTCCTCCATCACTTGCG
1a	CGFP_ACR1_f_RV	caggttctcggatccAGCGGAGTCGTCGTGTTC
1b	CGFP_ACR1_t_RV	caggttctcggatccAGTCTCGCCAGCACGAG
2	CGFP_ACR2_FW	TTTTATTTACAATCCATGGCTTCCCAGGTGGTG
2a	CGFP_ACR2_f_RV	CAGGTTCTCGGATCCGCACATGGAGTGGTCAGC
2b	CGFP_ACR2_t_RV	caggttctcggatccACGACCGAACATACGGATGT
3	NGFP_ACR1_FW	tacttccaaggtgccATGTCCTCCATCACTTGCGAC
3a	NGFP_ACR1_f_RV	gaggttaatcacttaAGCGGAGTCGTCG
3b	NGFP_ACR1_t_RV	gaggttaatcacttaAGTCTCGCCAGCACGAGCG
4	NGFP_ACR2_FW	tacttccaaggtgccATGGCTTCCCAGGTGGT
4a	NGFP_ACR2_f_RV	gaggttaatcacttaGCACATGGAGTGGTCAGC
4b	NGFP_ACR2_t_RV	gaggttaatcacttaACGACCGAACATACGGATGTT

*Designed and provided by Miroslaw Tarnawski

PCR reaction mixtures were prepared according to the CloneAmp™ HiFi PCR Premix Protocol using 1 ng of template and 7.5 pmol of forward primer (C, N or 1-4) and 7.5 pmol of reverse primer (Ca, Na or 1a-4a for full-length constructs of 1317 bp or 1b-4b to generate truncated variants of 885 and 873 bp for ACR1 and ACR2, respectively) to obtain two linearized vectors and the 8 linearized inserts. Cycling conditions for the PCR reactions performed in the DNAEngine thermocycler are listed in Table 7.

Table 7. PCR cycling conditions

Step	Temperature	Time	No. cycles
Denaturation	98°C	10 s	
Annealing	55°C	15 s	35
Elongation	72°C	15 s/kb for inserts, 5s/kb for vectors	

DNA amplification and integrity was confirmed by agarose gel electrophoresis and DNA was purified from cut-out gel slices using the PCR clean-up Gel extraction Kit (Macherey-Nagel, Düren, Germany) following manufacturer's instructions. To clone the inserts into the vectors, the In-fusion HD Cloning Kit (Takara) was used and the cloning reaction was set up

as described in the manual using 50-75 ng of linearized vector and 50-75 ng of insert DNA. For each completed reaction, 50 µl of *E.coli* Stellar™ Competent Cells (Takara) were transformed with 2.5 µl of the reaction mixture, following the transformation protocol. Transformed cells were plated on ampicillin supplemented LB agar plates prepared by the media kitchen and incubated overnight at 37°C. The next day, for each of the eight constructs, three single colonies were picked and used for plasmid amplification and purification. To verify that the desired constructs were obtained, purified plasmids were subjected to a restriction digest and DNA sequencing.

Restriction digest

For all four ACR1 constructs, *Eco*RV and *Eco*NI restriction enzymes were used, except for NGFP-ACR1 where *Aat*I and *Eco*NI were used. For NGFP-ACR2, NGFP-ACR2-t and CGFP-ACR2-t, *Eco*Rv and *Nco*I were used. For CGFP-ACR2, *Bam*HI and *Nco*I were used. 0.3-0.5 µg DNA were digested at 37°C for 30 min in the CutSmart buffer (New England Biolabs) and the fragments were separated by agarose gel electrophoresis.

2.2.2. Site-directed mutagenesis

The E68R mutant of CGFP-ACR1-t was prepared according to Quick Change II Site-Directed Mutagenesis Kit (Agilent) using primers CTA CCT GCC CAC CAC CCG GAT GAT CAC CTA CTCC and GGA GTA GGT GAT CAT CCG GGT GGT GGG CAG CTAG. The reaction was set up using 20 ng of CGFP-ACR1-t template and 125 ng of each primer. Cycling conditions are listed in Table 8. Stellar Competent cells were transformed with 1 µl of reaction mixture.

Table 8. Cycling conditions of the polymerase chain reaction

Segment	Cycles	Temperature	Time
1	1	95°C	30s
2	17	95°C	30s
		55°C	1 min
		68°C	8:30 min

2.2.3. General methods

Agarose gel electrophoresis

DNA was separated by charge and/or size with agarose gel electrophoresis. The gel was prepared by dissolving 1% (*w/v*) agarose in TAE buffer by microwave heating. For gel casting, 40 mL or 100 mL of the molten gel supplemented with 1 × GelRed Nucleic Acid Gel Stain (Biotium, Hayward, CA, USA) was poured into a PerfectBlue Mini tray (7 × 8 cm or 10 × 10 cm tray) gel system (PeqLab, Erlangen, Germany) containing a comb. Upon solidification, the comb was removed and the gel was immersed in 1 × TAE buffer. DNA samples mixed 5+1 with a 6 × Gel loading dye, purple (New England Biolabs, Ipswich, MA, USA) were loaded into the wells, as well as the GeneRuler 1 kb DNA ladder for size estimation (Thermo Fisher Scientific, Waltham, MA, USA). Size separation was performed at 110 V for 30 min and the gel was imaged in the ChemiDoc MP system (Biorad, Hercules, CA, USA). If needed, DNA was purified from cut-out gel slices using the PCR clean-up Gel extraction Kit (Macherey-Nagel, Düren, Germany) following manufacturer's instructions.

Plasmid amplification and purification

Plasmid DNA was purified from an overnight culture grown at 37°C in a shaking incubator from a single cell *E.coli* colony inoculating LB medium supplemented with ampicillin at 100 µg/ml. For restriction digest and sequencing purposes, the Wizard® *Plus* SV Minipreps DNA Purification System Kit and protocol was used. For transfection of insect cells, sterile plasmid DNA was prepared using the Qiagen Plasmid Midi Kit and protocol in which the final step of DNA redissolution in water was performed under sterile conditions in a laminar flow box. Plasmid DNA concentration was determined spectrophotometrically by measuring the absorbance at 260 nm.

Sequencing

For sequencing, 15 µl of plasmid DNA at 50 ng/µl was sent to Eurofins MWG Operon (Ebersberg, Germany). The corresponding two primers used for sequencing of each construct are listed in Table 9.

Table 9 Primers used for sequencing.

Name	Sequence	Used for
ie1_promotor_FW	AGTTGCAAGTTGACACTGGC	all CGFP fusions
NGFP_FW	TGTACATCATGGCCGACAAG	all NGFP fusions
ACR1_FW	AGCGTCTGAAGCTGATGCGTAT	CGFP-ACR1-f and –t incl. E68Q NGFP-ACR1-f and -t
ACR2_FW	TGGTGTTCACCATCTTCCAAG	CGFP-ACR2-f and -t NGFP-ACR2-f and -t

2.3. Culturing of insect cells for protein expression

The insect cell line *Spodoptera frugiperda* 21 (IPLB-Sf21-AE) (Sf21) provided by Kazuhiro Yamada was used for expression of ACR1 and ACR2 constructs. Miroslaw Tarnawski provided the wild type *Autographa californica* nuclear polyhedrosis virus (AcNPV) purified from DH10Bac *E.coli* cells for transient expression tests and also the linearized bacmid BAC10:KO_{1629} [141] for recombinant expression. All work was performed under sterile conditions in a laminar flow hood. Every three months, a new aliquot of cells was thawed and used for culturing.

2.3.1. Cell culture

The insect cells were cultivated in the SFM III Media (Thermo Scientific) at 27° and shaken at 100 rpm in all experiments (except for plates, which were not shaken). Every 2-3 days, the cells were subcultured by dilution with fresh media to a cell density of 0.4-0.6 × 10^6 cells/mL to maintain exponential growth. Cells were counted using the Luna-IITM Automated Cell Counter and the viability of >95 % was periodically confirmed by staining with Trypan Blue Stain 0.4 %, following manufacturer's instructions.

2.3.2. Transient transfection (''transfection/infection'')

Transient transfection by the AcNPV was performed for expression screening of all eight ACR constructs using the dual purpose vector pIEx/Bac-1. A confluent layer of Sf21 cells (2 mL) in a 6-well plate was transfected with 200 µl of 2 µg DNA mixed with the Xtreme Gene Transfection reagent as described in the reagent manual and incubated for 20 h. Then, the culture was infected with 150 µl of wild type AcNPV virus. This induced protein expression by activating the AcNPV derived ie1 immediate early promotor and hr5 enhancer contained in the pIEx/Bac-1 vector. After another 72 h of incubation, the cells were imaged under a fluorescence microscope to detect GFP fluorescence. The culture was harvested by centrifugation (2000 rpm, 4°C, 15 min). The pellet was washed with 150 mM NaCl, 20 mM Tris pH 7.5, flash frozen and stored at -20°C until further analysis by in-gel fluorescence and Fluorescence Size Exclusion Chromatography (FSEC).

2.3.3. Recombinant baculovirus generation and amplification

Higher levels of heterologous gene expression can be achieved by production of a target gene-containing baculovirus by in *vivo* recombination. 5 µg of the bacmid and 2 µg of DNA in 200 µl media were mixed with 8 µl Xtreme Gene Transfection reagent and incubated for 20-30 min at RT. Then, a confluent layer of Sf21 cells (2 mL) in one well of a 6-well plate was infected with the mixture. 5 days after infection, virus generation was confirmed by determination of cell viability and protein expression was confirmed by fluorescence

microscopy. The cells were harvested as described above, and the supernatant containing the p_0 recombinant baculovirus generation was kept sterile and stored at 4°C for up to six months.

The p_0 generation was amplified by infecting a 50 mL Sf21 cells suspension culture at a density of 2×10^6 cells/mL with 0.5-1 mL of the p_0 generation. 5 days after infection, the cells were imaged and the viability was determined prior to harvesting. The sterilely handled supernatant containing the p_1 baculovirus generation was filtered with a 0.22 µm filter and stored at 4°C for up to six months.

The above amplification step was repeated once more to generate a final p_2 baculovirus stock. All steps were as for p_1 generation, except that 8 mL of p_1 generation was used to infect 400 mL of Sf21 cells at a density of 2×10^6 cells/mL. The p_2 baculovirus stock was used for protein expression.

2.3.4. Protein expression

Protein expression was performed in multiple 3 L conical screw-cap glass flasks (Pyrex). 400 mL of Sf21 cells at a density of 2×10^6 cells/mL were supplemented with 5 µM all-trans retinal (prepared as a 44 mM stock in ethanol) and infected with 50 – 70 mL p_2 baculovirus stock. The cultures were harvested after 3 days of incubation. The supernatant was discarded and the washed pellet was flash frozen and stored at -20°C until further use. The level of protein expression could be visually estimated from the intensity of orange colour of the pellet.

2.4. Protein purification

2.4.1. Purification of bacteriorhodopsin

bR from the overproducing *Halobacterium salinarum* stain R_1S_9 was expressed by Ramona Schlesinger's group (FU Berlin) and obtained as purified PM.

Purification was performed as described previously [134] with slight modifications [142]. Briefly, PM were pelleted by ultracentrifugation (50 000 rpm, rotor Ti70, 30 min, 4 °C) and resuspended to a final bR concentration of 0.9 mg/mL in 50 mM K_2HPO_4/NaH_2PO_4 pH 6.9, 1.7 % (*w/v*) *n*-octyl-*β*-D- glucoside (OG; Anagrade, Anatrace). The suspension was sonicated for 2 min (1 s on/ 2 s off, 40 % amplitude) and for 1 min (1 s on/ 2 s off, 60% amplitude) and solubilized for 24 h at RT in the dark. Then, the pH was adjusted to 4.4 with HCl, the insoluble fraction was pelleted by ultracentrifugation (50 000 rpm, rotor Ti70, 30 min, 4 °C) and the soluble fraction was concentrated to 5-8 mg/mL and injected onto a size exclusion

chromatography column HiLoad™ 16/600 Superdex™ 75 pg (GE Healthcare, Uppsala, Sweden) equilibrated in 25 mM K_2HPO_4/NaH_2PO_4 pH 5.6, 1.2 % β-OG. The absorption was monitored at 280 and 560 nm and the second peak was collected and concentrated to 35-40 mg/mL for crystallization in LCP. The protein concentration was determined spectrophotometrically at the maximum at 560-570 nm using the extinction coefficient of 63 000 M^{-1} cm^{-1}.

2.4.2. Purification of anion channelrhodopsin

Cell pellets were resuspended in 150 mM NaCl, 20 mM Tris pH 7.5 supplemented with cOmplete EDTA-free tablets and lyzed by two passages at 850 psi in a microfluidizer (Microfluidizer M110-S). The membranes were pelleted by ultracentrifugation (T29 rotor, 40 min, 40 000 g, 4°C), washed in 20 mM Tris pH 7.5, 500 mM NaCl, 8% glycerol (Buffer A) and again centrifuged. The washed pellet was resuspended in Buffer A supplemented with 2 % DDM for solubilization (2 h, stirring, cold room). The solubilized fraction was separated from the insoluble one by ultracentrifugation (Ti70, 30 min, 50 000 rpm, 4°C). The supernatant (orange) was incubated with Ni-NTA beads (about 1 ml resin for 1.4 ml protein solution) equilibrated in Buffer A supplemented with 0.05 % DDM for overnight binding in batch. The next day, the beads were washed 3 × with 3 bead volumes of Buffer A supplemented with 0.05% DDM and 30 mM imidazole. The protein was eluted on a column with Buffer A supplemented with 0.05% DDM and 500 mM imidazole. The eluate was dialyzed against 20 mM Tris pH 7 (at 7°C), 300 mM NaCl, 0.025 % DDM (Buffer B) in the cold room for 2 hours, after which the buffer was exchanged, 1 mM DTT was added to the buffer and to the protein solution, to which also the TEV protease was added for overnight cleavage of the GFP and His-tag. The next day, the sample was loaded on a Ni-NTA column equilibrated with Buffer B. The orange cleavage mixture was separated into yellow-green GFP and TEV binding to the column and red ACR1-t eluting in the flow-through. The eluate was loaded onto a gel filtration column equilibrated in 50 mM K/Na Pi, pH 5.8, 300 mM NaCl, 0.025 % DDM. The absorbance was monitored at 280 nm and 500 nm. A single peak at 500 nm eluting at 16 ml was collected, purity analyzed by SDS-PAGE and the appropriate fractions were pooled and concentrated for crystallization to A_{515nm} = 5 - 6 at 1 mm, using centrifugal concentration units with a MWCO of 50 kDa. To decrease the detergent content, the concentrated protein was diluted 20 × with buffer without DDM and again concentrated to the initial value.

2.5. Biochemical and biophysical protein analysis methods

Expression detection by in-gel fluorescence imaging and fluorescence-detection size exclusion chromatography (FSEC)

Expression and solubilisation of ACR-GFP constructs were analysed by in-gel fluorescence imaging of SDS-PAGE gels (see below) and initial samples from transient expression were also analysed by FSEC to judge protein folding and dispersity. Cells were resuspended in 200 µl 20 mM Tris pH 7.5, 500 mM NaCl, lyzed by two cycles of freeze-and-thaw and solubilized with 1 % *w*/*v* DDM for 1 h at 4°C. The insoluble fraction was pelleted by ultracentrifugation (rotor TLA-100, 40 000 rpm, 30 min, 4°C) and 30 µl of each sample were injected onto a gel filtration column (Superose 6 10/300, GE Healthcare) equilibrated in 20 mM Tris pH 7.5, 150 mM NaCl, 0.03 % DDM and the absorbance was monitored at 260 nm, 280 nm, and 515 nm. The total and solubilized fractions were taken for SDS-PAGE analysis with GFP-fluorescence imaging.

For detergent screening, detergents DDM, decyl maltoside (DM), OG and Cymal-5 were used for solubilisation at 1 % *w*/*v*.

Sodium dodecyl sulfate polyacrylamide gel electrophoresis (SDS-PAGE)

SDS-PAGE under denaturing and reducing conditions was performed as described by Laemmli.[143] The separating gel contained 375 mM Tris/Cl pH 8.8, 0.1 % SDS, 10–15 % acrylamide:bis-acrylamide (37.5:1) mixture, 1.5 mM APS and 0.05 % TEMED. The stacking gel contained 125 mM Tris/Cl pH 8.8, 0.1 % SDS, 4.5 % acrylamide:bis-acrylamide (37.5:1) mixture, 2.2 mM APS and 0.1 % TEMED.

Samples were mixed with 1 × SDS loading dye and the PageRuler Prestained ladder (Thermo Fisher Scientific) was used for molecular mass estimation. The electrophoresis was performed at 120 V for 60-70 min. For in-gel GFP-fluorescence detection (excitation 395 nm, emission 509 nm), the gel was immediately imaged in the ChemiDoc MP system (Biorad, Hercules, CA, USA). Thereafter, the gel was stained with InstantBlue (Expedeon, Over, UK) and imaged. The molecular mass of proteins used in this work is listed in Table 10.

Blue native PAGE

Separation of proteins in their oligomeric state by Blue native PAGE, where Coomassie blue G250 is used to provide negative charges to the protein surface without denaturation, was performed as described.[144] 1 µl of ACR1-t sample was 10 × diluted into the buffer (250 mM NaCl, 50 mM MES pH 6.6) with 0.025 % or 0.0125 % or no DDM and incubated overnight in the cold room. Next, the samples were centrifuged (table top centrifuge, 10 min, 15 000 rpm, 4°C) and the supernatant was mixed with 15 µl of sample buffer and loading buffer mixture

(75 µl + 10 µl, resp.) and loaded onto a 4 – 16 % gradient gel (SERVA*Gel*™), together with the NativeMarkProtein ladder (Invitrogen). After the run, the finished gel was stained with Instant Blue and imaged.

Spectrophotometric determination of protein concentration

Protein concentration was determined according to Lambert-Beer's Law using the NanoDrop ND-1000 spectrometer. For glucose isomerase and thermolysin, absorbance and extinction coefficient at 280 nm was used, whereas for bR the values at 570 nm were used. For ACR1-t, samples for crystallization were set to the same concentration based on the optical density at 515 nm.

Table 10. Absorption maxima (Amax), extinction coefficients (ε) and molecular mass of proteins used in this work.

Protein	A_{max}	ε [M^{-1} cm^{-1}]	Molecular Mass [Da]
bR	570 nm	62 000	26 800
CGFP-ACR1			79 300
CGFP-ACR1-t			62 700
ACR1-t	515 nm		33 300
CGFP-ACR2			78 600
CGFP-ACR2-t			62 000
GFP with 10x His-tag			29 500
NGFP-ACR1			79 400
NGFP-ACR1-t			62 800
NGFP-ACR2			78 700
NGFP-ACR2-t			62 100
Thermolysin	280 nm	58220	34 600
Glucose isomerase	280 nm	45 660	43 000

Retinal extraction and High Pressure Liquid Chromatography (HPLC) separation

Retinal extraction and HPLC separation was used to determine the relative amounts of all-*trans* and 13-*cis* retinal in a given retinal protein sample.[145,146] In case of LCP samples, the first step was to mix 8 µl of LCP+F-127 paste thoroughly with 165 µl ice-cold 75 % (*w/w)* ethanol by vigorous pipetting. Phase separation of the emulsion was performed by centrifugation (1 min, 4 °C, 21130 x g, Eppendorf Centrifuge 5424 R) and the retinal isomers in the upper hexane layer were immediately separated by HPLC on a 125 x 4.6 mm ID Prontosil 120-3-Diol normal phase column (CS-Chromatographie Service GmbH) equilibrated in 9:1 hexane:ethyl acetate and running at a 1.5 mL/min flowrate. The 13-*cis* isomer eluted in the first peak and the all-*trans* isomer in the second peak, as confirmed by

comparing the retention times with an all-*trans* retinal standard (Sigma, R2500). The relative quantities of both isomers were calculated using integrated peak areas and 13-*cis* and all-*trans* extinction coefficients of 1365 and 1690, respectively, at 360 nm in hexane.[146]

2.6. Crystallization

Bacteriorhodopsin

bR was crystallized in LCP using monoolein (NuChek Prep) and gas-tight Hamilton syringes (1710 or 1725 RN) connected by a coupler (TTP Labtech). A string of LCP was extruded into a Hamilton syringe filled with precipitant (30 or 32 % PEG 2000, 0.1 M K2HPO4 /NaH2PO4 pH 5.6) as described previously.[113,134] Very densely packed purple hexagonal plate-shaped bR crystals (20-50 µm for 30 % PEG and 10-30 µm for 32 % PEG in the longest dimension) appeared in a strongly birefringent mesophase within days.

Anion channelrhodopsin

Concentrated and washed ACR1-t was reconstituted in LCP using monoolein (NuChek Prep) and gas-tight Hamilton syringes (1710 or 1725 RN) connected by a coupler (TTP Labtech). Sparse matrix screens were set up in LCP sandwich plates (Marienfeld, Hampton Research) at 20°C as described.[112]

Thermolysin

Lyophilized thermolysin (TRL) from *Geobacillus stearothermophilus* (No. P1512, Sigma) was dissolved in 50 mM NaOH at a concentration of 25 mg/ml and crystallized as described earlier[147] except that seeding was used to control crystal size. Crystals were grown by batch approaches in 1.5 ml microtubes. 200 µl protein and 200 µl precipitant (40% PEG 2000, 0.1 M MES pH 6.5, 5 mM $CaCl_2$ containing crystal seeds) solutions were mixed rapidly. Crystals reached their final size (50-130 µm × 5-10 µm × 5-10 µm) overnight. After settling to the bottom of the microtube, they were washed with storage solution (20% PEG 2000, 0.1 M MES/NaOH pH 6.5, 5 mM $CaCl_2$).

Glucose isomerase

Crystalline glucose isomerase (GI) suspension was purchased from Hampton Research (HR7-102), repeatedly dialyzed against 10 mM HEPES/NaOH pH 7.0, 1 mM $MgCl_2$ and filtered through a 0.22 µm filter. Crystals were prepared by rapidly mixing 200 µl of protein (80 mg/ml) and 200 µl of precipitant (2.6 M $(NH_4)_2SO_4$, 0.1 M Tris/HCl pH 7.5, 1 mM $MgCl_2$, containing crystal seeds) solutions. Spherical crystals (10-15 µm × 10-15 µm × 10-15 µm) grew overnight. After settling to the bottom of the microtube, the crystals were washed several times with storage solution (1.4 M $(NH_4)_2SO_4$, 0.1 M Tris/HCl pH 7.5, 1 mM $MgCl_2$).

Lysozyme

Hen egg-white lysozyme (HEWL) crystals (30 µm × 20 µm × 20 µm) were prepared by Ilme Schlichting as described earlier[133]. The storage solution was 8% (*w*/*v*) NaCl, 0.1 M HOAc/NaOH pH 4.0.

2.7. Gel preparations and characterization

Care was taken to prepare the gels to be as dust–free as possible, to minimize the risk of clogging problems during injection and to prevent microbial contamination as some gels can serve as growth media. All solutions used for preparations were filtered with a 0.22 µm filter and sterile plastic ware was used when possible.

2.7.1. Carboxymethyl cellulose sodium salt gel preparation

Carboxymethyl cellulose sodium salt ultra-high viscosity (NaCMC; No. 21904, Sigma) forms a rigid gel in water starting at a 2.5 % (*w*/*v*) concentration and viscosity increases with concentration until the solubility limit is reached, which lies slightly above 10 % (*w*/*v*) concentration. A 7 % (w/v) stock gel was prepared by sprinkling 7 g of NaCMC over 100 ml ultra-pure water in a 600 ml beaker in order to have a large water surface coming in contact with the polymer. To prevent evaporation and dust accumulation, the beaker was sealed with Parafilm® M which was perforated with a needle 3-5 times. The mixture was heated (60-70 °C) and occasionally carefully homogenized with a spatula to help uniform swelling, while minimizing the trapping of bubbles. A homogenous thick gel formed within 2 days at room temperature and was stored for weeks at 4 °C to prevent growth of microorganisms. An alternative and faster protocol is to slowly add NaCMC to vigorously stirred water in a large beaker. Once all powder has been added, stirring speed is decreased and the mixture is heated (60-70 °C) under vacuum for 1 hour. Stirring and heating is subsequently switched off and the gel is left overnight in vacuum to completely hydrate and to remove residual bubbles that may disturb injection.

Prior to embedding crystals in the gel, the gel was equilibrated with the crystal storage solution. To this end, the stock gel was transferred with a spatula into a 10 ml plastic syringe and 5 g of the stock gel was extruded through a 4 mm diameter needle into a 25 ml beaker and 5 ml of 1-2X storage solution were added (1X storage solution for TRL and GI crystals, 2X storage solution for HEWL crystals). The mixture was heated for 1-2 h (60-70 °C) and allowed to swell overnight. The gel equilibrated with precipitant solution was then transferred into a 10 ml plastic syringe to allow convenient filling of Hamilton syringes, which were then used to evenly mix 45 µl of the gel with 1-5 µl of crystal pellet using a coupler. Care was taken to avoid trapping bubbles at any stage.

2.7.2. Pluronic® F-127 gel preparation

Pluronic® F-127 (P2443 Sigma) forms a rigid thermoreversible gel in water at 20 – 35 % (w/w) concentration, which is liquid at 4°C and solid at room temperature. A 35 % (w/w) stock solution was prepared by adding 16 g of F-127 to 29.7 ml cold water in a 50 ml plastic tube. Only gentle mixing with the spatula is possible, as F-127 readily creates foam. Therefore, the mixture was allowed to dissolve in the cold room and was gently stirred only 1-2 times per day to better mix the pelleted/ clumped polymer into the gelling liquid. This process typically took three days, creating a clear viscous liquid (similar to liquid honey in viscosity), which was stored in a closed tube to avoid dehydration. To embed TRL, GI and HEWL crystals, the cold 35% F-127 stock solution was poured into a 5 ml plastic syringe for transfer 50 µl into a Hamilton syringe. This was then coupled to another Hamilton syringe filled with crystal storage solution (12.5 µl 1X, 2.5 µl 1.5 X, 12.5 µl 2X in case of TRL, GI, and HEWL, respectively) and homogenized. The entire content was then moved to the syringe that originally contained the storage solution, the syringes were decoupled and the empty syringe was filled again with the same volume of storage solution. It was then reattached to the other syringe and the mixture was again homogenized. In this manner, the storage solution was added from "both ends" to facilitate complete homogenization, which was confirmed by extruding a small amount of the gel through the coupler from both ends and from the middle of the coupled syringes, making sure that no droplets indicating liquid were present. Notably, once the gel was mixed with storage solutions or with other tested chemicals (except for the TRL storage solution that contains 20% PEG 2000), the thermoreversible properties disappeared and the gel was irreversibly solid, likely due to the increased ionic strength. 45 µl of the gel was then mixed with 2.5-5 µl of the crystal pellet using coupled Hamilton syringes and loaded into the HVE injector. In the case of the in meso grown bR crystals, the crystal-containing and strongly birefringent mesophase from multiple syringes was harvested and pooled. For the diffraction experiment, 25 µl of this mesophase were mixed with 25 µl of 35% F-127, yielding a transparent phase within minutes. For stream velocity measurements, F-127 was mixed 1+3 with the LCP. A similar Pluronic compound, Pluronic® F-108 (No. 542342 Aldrich), prepared as a 40% stock gel, can be mixed with LCP in an analogous manner.

2.7.3. Preparation of previously described media

The synthetic grease Super Lube® (No. 21030, Synco Chemical Co.) was mixed with crystals as has been described.[148] Briefly, 95 µl of grease and 5 µl of crystal pellet were mixed with a spatula on a glass slide and transferred to a 250 µl Hamilton syringe using a spatula. A hydrophilic matrix consisting of 5.6 % (w/v) ultra-low gelling agarose (No. A5030 Sigma) and 30% glycerol[149] was prepared by heating the mixture to 100 ˚C using a ThermoMixer C

(Eppendorf). Hyaluronic acid (No. H5388, Sigma) was prepared as a 12 % (w/v) aqueous mixture.[150]

2.7.4. Characterization of chemical compatibility

The precipitant solutions for the compatibility tests were: 2.5 M Li_2SO_4, 2.5 M $MgSO_4$, 3.6 M $(NH_4)_2SO_4$, 4 M NaCl, 70 % (w/v) PEG, 50 % (w/v) PEG 2000, 50 % (w/v) PEG 4000, 50 % (w/v) polypropylene glycol (PPG) 400, 80 % (v/v) ethanol, 50 % 2-Methyl-2,4-pentanediol (MPD). If needed, the pH of PEGs, PPG and salts was adjusted to neutral with 1 M Tris HCl pH 7.5.

The carboxymethyl cellulose gel equilibrated with the precipitant solution was prepared by mixing 2 g of 7% (w/v) stock NaCMC gel with 2 ml of precipitants solutions listed above. To test compatibility of 35% F-127, 100 µl was mixed with 50 or 100 µl of precipitant solution listed above using two coupled glass syringes. Homogeneity, viscosity and injection properties were visually estimated by manually extruding the mixture through the coupler (410 µm inner diameter).

2.7.5. Stream velocity measurements

To determine the velocity of the extruding stream, movies of the stream were recorded at 60 Hz with a high speed camera (Photron FASTCAM SA-Z equipped with a Navitar 12 X zoom lens) for a chosen stream flow rate (0.3-5.9 µl/min). In the movies, a feature in the extruded stream (e.g. a crystal) was tracked with time as it moved downstream. Length scales in the movie image had been explicitly calibrated against a standard calibration slide and the frame speed of the camera was very well defined. Accordingly the stream velocity could be computed very accurately by measuring the displacement of the tracked feature from frame to frame. Typically, 3-5 of these points were averaged to obtain an average velocity value at a given flow rate. The average stream velocities were then plotted against tested flow rates and fitted with simple linear regression. The crystal concentration in F-127 and NaCMC samples was 5 % (*v/v*) and 2.5-5 % (*v/v*), respectively.

2.8. Serial synchrotron crystallography data collection and analysis

The HVE injector was mounted on the goniometer head of the X10SA (PXII) beamline at the SLS pointing vertically downward to benefit from gravitational force on the extruding stream.[133] The inner diameters (ID) of the capillaries were chosen according to crystal size and desired stream velocity, for F-127 and NaCMC samples 100 µm and 150 µm capillaries were used, respectively. For comparison data sets in grease, the same ID capillary was used as for the sample under comparison. Sample consumptions and stream velocities are listed in Table 11. By means of a Shimadzu 20AD HPLC pump amplified by the intrinsic piston factor of the HVE injector[133] a pressure of 350-700 psi was applied to the sample. The pressure of the guiding helium-sheath gas was typically 5-15 psi. Still diffraction data (no oscillation) were collected at room temperature in the high flux undulator setting using the full beam (3.4×10^{12} photons s^{-1} in 50×10 µm^2) and a wavelength of 1.033 Å, except for the HEWL in grease data, which was collected at 0.954 Å (2.4×10^{12} photons s^{-1} in 50×10 µm^2). The PILATUS 6M detector was operated in a continuous shutterless mode and still diffraction patterns were recorded at 10 Hz (exposure time 100 ms). The diffraction data were identified, indexed and integrated with *nXDS*.[151] The program uses an Ewald offset correction factor to estimate reflection intensities recorded on still exposures and implements post-refinement to improve all diffraction parameters and scaling and correction factors.[151] *nXSCALE* was used for scaling of data streams from the same sample, but collected with different parameters. Background profiles were calculated by Thomas Barends determining the median intensity in all pixels over 50 evenly spaced images of a data set. The resulting background images were then radially integrated after applying a beamstop mask.

Table 11. Sample injection parameters

Sample	Crystal size (µm)	Nozzle inner diameter (µm)	Flow rate (µl/min)	Measured stream velocity (µm/s)
bR-LCP+F-127	20-50	100	0.09	50
bR-LCP	20-50	100	0.15	Very variable
GI in F-127	10-15	100	0.15	50-60
GI in grease	10-15	100	0.06	130-290
TRL in F-127	60-130	100	0.15	60-70
TRL in grease	60-130	100	0.06-0.15	125-280
TRL in NaCMC	60-130	150	0.6	240-270
TRL in grease	60-130	150	0.15	150-170
HEWL in NaCMC	20-30	150	0.3	50-70
HEWL in grease	20-30	100	0.06-0.15	120-200

2.9. Time-resolved serial femtosecond crystallography data collection and analysis

2.9.1. Injection and pre-illumination

The bR crystal-loaded mesophase (pooled from multiple syringes) was mixed with an equal volume of monoolein (Nu-Chek Prep) and diluted (4+1) with Pluronic F-127 40% *(w/v)* to improve flow properties of the stream.

Pre-illumination

Samples were loaded into a 340 µl reservoir of our High Viscosity Extrusion (HVE) injector[133] equipped with a 76 mm long UV-VIS transparent capillary (100 µm ID) over which a cylindrical metal mask was slid into place. A 22 mm long window in this sleeve admitted continuous pre-illumination light perpendicular to the plane defined by the sample stream and the X-ray beam. The bR microcrystals were pre-illuminated as they flowed through this illuminated region. Since back-lighting of the interaction point for the off-axis camera required a hole on this side of the nozzle shroud, the terminal 4-5 mm of the mask was left solid to provide a fully defined "dark zone" near the HVE exit to allow the crystals to return to the bR ground state prior to being photoexcited with an optical pump laser pulse entering colinearly with the X-ray beam (downstream of the HVE tip and passing behind the "dark zone" mask; Figure 6). With a sample flow rate of 1.9 µl/min, the stream velocity in the capillary averaged 4 mm/s. Thus the microcrystals spent 5.5 s in the illuminated section and 1-1.25 s in the dark section of the capillary. The 520 nm pre-illumination laser (Oxxius LBX-525-800-HPE-PP) was coupled into a continuous 10 m multimode fibre (Thorlabs, FT1500UMT, 1.5 mm core diameter, TECS clad), which entered the vacuum chamber through a custom-built clamping O-ring seal. The polished end of the fibre was positioned 90 mm from the sample stream. At this distance the intrinsic angular spread of light emerging from the fibre slightly over-filled the 22 mm long pre-illumination slit in the masking sleeve. By running the fibre directly into the vacuum chamber and using its polished end as the light source, optical losses were considerably reduced relative to the use of standard fibre-optic vacuum feedthroughs. The spot from the pre-illumination laser was measured to be ~4 cm in diameter at 90 mm from the fibre end. The laser power was set to 200 mW (measured output of the multimode fibre after passing through the vacuum feedthrough). The nozzle shroud itself was specially constructed with a long narrow slit on the pre-illumination side, allowing the pre-illumination light to fully fill the slit in the sleeve mask while still minimizing the amount of light entering the shroud. To measure the pre-illumination efficacy in house or on-site in the vacuum chamber, the sample from the

mounted, illuminated and aligned HVE injector was extruded into a black Eppendorf tube and immediately subjected to retinal extraction and separation in the dark.

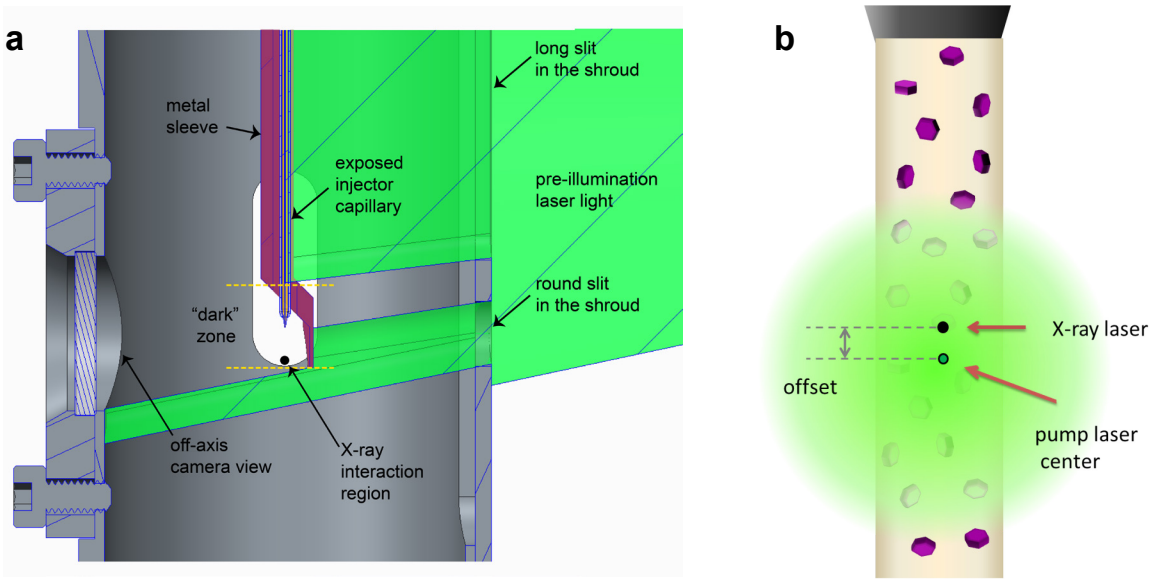

Figure 6. Experimental layout. a, Cross-sectional drawing of the injector nozzle in the shroud in the scattering chamber (view along the X-ray and optical pump laser axis). The long upper slit in the shroud allows the pre-illumination light (green) to propagate onto the injector capillary. The lower round slit allows the green light to weakly illuminate the interaction region (with the nozzle moved slightly up) for imaging the sample in the free jet with the off-axis camera. The capillary is equipped with a metal sleeve (purple) that allows the green light to enter the capillary but blocks the light in the last 4-5 mm upstream of the interaction region ("dark zone", yellow dashed lines). This figure is an adaptation of a drawing originally provided by Bruce Doak for the publication Nass Kovacs *et al.*. **b,** The LCP stream with purple bR crystals is pumped by a green optical laser, the centre of which was offset by 25 um downstream of the X-ray interaction region in the TR-SFX experiment.

Light scattering from a circular sample jet

The refractive index of LCP was measured with a refractometer to be 1.42 at 532 nm. Using this value, scattering of light from the surface of a circular LCP jet was determined with ray tracing simulations. A collimated light beam perpendicularly impinged on a 100 µm diameter jet cross section and the reflection was calculated using Fresnel equations. To determine the scattering of light by LCP containing bR microcrystals, the transmittance of an empty cuvette, a cuvette filled with a 65% glycerol solution (refractive index as LCP), filled with LCP prepared from monoolein and water supplemented 4+1 with F-127 and filled with bR crystals in LCP prepared as used in SFX, respectively, was measured using a Jasco V-760 spectrophotometer. In case of bR crystals, the absorbance is then determined by scattering and absorption. To disentangle these two components of the signal, the crystals were completely bleached by UV radiation prior to measuring the spectra. After bleaching, only the scattering component contributed to the measured signal.

2.9.2. Data collection

The diffraction experiment was performed in the microfocus chamber of the Coherent X-ray Imaging (CXI) instrument of the Linac Coherent Light Source (LCLS) at SLAC National Accelerator Laboratory[152] in July 2017 (proposal LP55). Diffraction data was collected using 9.8 keV photons. The photon pulse length was ~30 fs, the average pulse energy was 3.4 mJ and the X-ray focus was ~1.3 μm in diameter. The X-ray beam was attenuated to ~14 % transmission. Taking into account the beamline transmission of ~50 %, this resulted in a pulse energy of ~0.2 mJ at the sample position. Time-resolved SFX data were collected at 10 Hz with nominal time-delays between the optical pump and probing FEL pulses of 0.5, 1, 3 and 10 ps. For the 0.5 ps data, a timing tool was used to determine the exact time-delay between the optical pump and X-ray probe.[153] In addition, two so-called dark data sets were collected at 120 Hz from pre-illuminated but not pumped bR microcrystals, to analyse whether or not the light-adapted sample had returned to the all-*trans* ground state. These "dark" data sets also served as reference for the time-resolved data of photoexcited bR. To check whether the short-lived intermediates represent functional steps of the bR photocycle, a 33 ms time-delay dataset was collected, corresponding to an M-like intermediate at 30 Hz repetition rate. All diffraction patterns were recorded using a Cornell-SLAC Pixel Array Detector (CSPAD)[154] that was operated in dual-gain mode with a low and high gain in the low and high resolution region of the detector, respectively.

Femtosecond pump laser excitation of bR crystals in the TR-SFX experiment

The bR microcrystals were photoactivated using circularly polarized 532 nm laser light from an optical parametric amplifier pumped by a Ti-Sapphire laser regenerative amplifier system. The laser pulses were stretched to 145 ± 5 fs. The laser beam had a Gaussian profile; the laser focus was 99 μm ($1/e^2$) at the sample stream position. To allow for accurate timing, the sample stream was kept at the same position along the beam direction using an optical camera. The optical laser was collinear with the X-ray beam. The centre of the pump laser was offset 25 ± 5 μm downstream of the X-ray focus for all (sub)-ps pump probe measurements (Figure 6b). Thereby a shorter stretch of illuminated microcrystal-containing LCP stream must clear the interaction region before the next pump probe cycle can be initiated. The laser pulse energy was ~5.9 μJ.

Photon/retinal calculations

The pulse energy E of ~5.9 μJ, beam radius r=49.5 μm and pulse length T of 145 fs result in a peak power density P of 1.06 TW/cm^2 using the formula

$$P = \frac{2E}{T\pi r^2}$$

Given the laser offset of 25 µm from the centre of the Gaussian pump beam, this decreases the power density in the X-ray interaction region by a factor of 0.6, resulting in 634 GW/cm^2. As about 20% of the light is scattered by the sample, this pump laser intensity available for the crystal is $P_{xta\ l}$= 507 GW/cm^2. To estimate the number of photons per retinal, the photon energy E_p of a 532 nm photon is calculated using the wavelength, the Planck constant h = 6,626 × 10^{-34} J s and speed of light c = 3 × 10^8 m/s

$$E_p = \frac{hc}{\lambda}$$

E_p of 3.73 × 10^{-19} J is then used to obtain the number of photons per area $N_p/A = P_{xtal} \times T/ E_p$, yielding 2 × 10^{21} photons/m^2. The number of retinals per area N_{ret}/A is obtained from the crystallographic unit cell dimensions α=β=90°, γ=120°, a=b=62 Å, c=111 Å, given a volume of 3.7 × 10^{-25} m^3. With 6 bR molecules, thus 6 retinals, in a $P6_3$ unit cell, the density of retinals is

6 / 3.7 × 10^{-25} = 1.6 × 10^{25} m^{-3}. Therefore, in a crystals of average thickness of 5.9 µm, the N_{ret}/A is 1.6 × 10^{25} × 5.9 × 10^{-6} = 9.4 × 10^{19} retinal/m^2. The ration of N_p/N_{ret} is then 2 × 10^{21} / 9.4 × 10^{19}, yielding an average of ~21 photons/retinal in the TR-SFX experiment.

Data analysis

CASS was used for identification of images containing diffraction patterns, online monitoring of diffraction quality, background subtraction and for file conversion.[155] CrystFEL version 0.6.3 was used for indexing and integration.[156] Q-weighted structure factor amplitude difference electron density maps[157] were calculated using custom-written scripts. As the occupancy of the illuminated states was only 10-15%, extrapolated structure factors were calculated, in which the occupancy of the illuminated state is extrapolated to 100%.[158,159] Because traditional reciprocal-space refinement against these extrapolated structure factor amplitudes proved unstable, real-space refinement against extrapolated density maps was performed using Phenix dev-3063.[160,161] Maps and structures were inspected using Coot[162] and Pymol. Pymol was used for making figures. The given torsion angle and atom-atom distance values from the refined sub-ps coordinates were obtained using a custom written python script. This also yielded the oscillation frequencies, which were also obtained when describing the data with a damped sinusoid[102] in the Grafit Data Analysis Software (Version 7), using the equation

$$A\sin(2\pi t\tilde{\nu}c + \phi)\, e^{-at} + b$$

where A is the amplitude, t is time, $\tilde{\nu}$ is the wavenumber, c is the speed of light, ϕ is the phase, a is the damping constant and b is the offset. Although a damped sinusoid could be fitted, negligible damping is indicated, likely due to the short observation window. Both methods gave same results within the error.

2.9.3. Transient ultrafast spectroscopy

Microcrystal preparation for ultrafast spectroscopy experiments

bR microcrystals grown in LCP were pooled directly from Hamilton syringes into a 1.5 ml centrifuge tube and gently centrifuged to collect the LCP in an upper layer above the precipitant. The LCP was then transferred into a 300 µl tube and centrifuged for 1-3 hours at maximum speed in a table top centrifuge. Residual precipitant was at the bottom and the upper LCP layer was separated into a lower layer highly enriched with crystals and a top layer consisting of LCP essentially without crystals. After removing the latter with a spatula, the enriched microcrystalline layer was used for spectroscopy. For IR measurements in D_2O, precipitant was first removed using a syringe from 200-500 µl of the LCP collected by gentle centrifugation. Then, it was resuspended in 1.5 ml D_2O crystallization buffer (32% (*w/v*) PEG 2000, 0.1 M K_2HPO_4 /NaH_2PO_4 pD ~ 5.6) by vortexing and recollected by gentle centrifugation. This step was repeated 3-5 times and then an enriched crystal layer was prepared as described above.

Ultrafast VIS and IR spectroscopy on bR microcrystals

For VIS measurements, enriched bR microcrystals in LCP were mixed with monoolein and F-127 until clear (2.5+1+1) and mounted between two CaF_2 windows, where a 50 µm and 100 µm spacer for the crystals and PM at pH 5.6 was used, respectively. For IR measurements, directly the highly enriched bR microcrystals in LCP and PM were mounted between two CaF_2 windows each using a 25 µm spacer. The VIS set-up was essentially as described previously[163] and further details are provided in Nass Kovacs *et al.*, which also includes the IR set-up description. The power titration was performed in the range 12 – 180 GW cm^{-2}.

3. Results

This work aimed at investigating light-induced structural changes in microbial rhodopsins initiated by retinal isomerization. Both the structures of ultrafast and later intermediates occurring along the photocycle would provide missing insight into how the protein harnesses the energy absorbed by the bound retinal to fulfil biological functions.

These structures can now be obtained at novel X-ray sources, XFELs, which enable time-resolved SFX experiments with up to sub-ps time-resolution and essentially radiation damage-free data collection at room temperature. Time-resolved SFX experiments require very stable injection, which in the case of HVE heavily depends on the viscous matrix used. Therefore, means of adjusting and controlling the injection properties of viscous matrices, such as LCP, were explored in this thesis. Further, new viscous matrices suitable for SFX were identified, which would allow more in-solution grown crystals to be amenable for SFX using HVE.

Microcrystals of bR grown in LCP were used to study the structural changes occurring on the ultrafast timescale in a TR-SFX experiment. High-resolution crystal structures of the sub-ps and ps intermediates following photon absorption were obtained. The structures were also used for QM calculations which provided a rational framework for interpretation. To be able to correlate the results with the large body of spectroscopic literature, ultrafast spectroscopy on the crystals was performed.

Developing HVE-based TR-SFX with a model retinal protein into a mature and optimized technique makes investigations of less readily available (retinal) proteins affordable. This is the case of the newly discovered anionchannelrhodopsin family, where structures of the intermediates would facilitate understanding of the distinct gating and selectivity mechanism. Therefore, production and characterization of ACR1 was carried out with the aim of a future TR-SFX experiment.

Another aim of this thesis was to obtain SFX structures of the ns-ms intermediates of the halorhodopsin photocycle. This would provide information on the yet unknown pathway by which the large chloride ion is translocated through the protein to the inside of the cell. Unfortunately, well-diffracting crystals could not be obtained in large quantities. A summary of this project is given in Appendix 6.2.

3.1. Viscous matrices for HVE in serial crystallography

The main advantage of HVE is the low sample consumption in case of low repetition rate data collection, which makes this serial sample delivery technique the method of choice even to microcrystalline samples attainable only in small quantities.[133] The applicability of HVE directly depends on the properties of the viscous matrix used. Given the diversity of protein crystal properties, the availability of a broad variety of viscous matrices is important as it maximizes the chances of finding an appropriate one for a given microcrystalline sample. Several viscous matrices have been characterized to date. They can be classified based on their chemical nature defining most of their properties – the bicontinuous bilayer mesophase LCP and hydrophilic and hydrophobic systems.

LCP is frequently used for HVE due to its inherent viscous consistency and the fact that many membrane proteins, such as G-protein coupled receptors, can be crystallized in it and then directly injected into the XFEL beam.[113] The viscosity of the crystal-loaded LCP can easily be adjusted to have appropriate injection properties.[113] Moreover, it has acceptable X-ray background and can be used at atmospheric pressure and also in vacuum. For *in vacuo* use, to prevent evaporative cooling and thereby an unwanted phase transition of the matrix, either the sample is flowed faster (several mm s^{-1}) or shorter lipids such as MAG 7.9[113] are added to the sample post-crystallization. LCP can also be used to deliver non-LCP crystallized samples, for example if sample scarcity limits the use of other injection methods. In these cases, crystals can be embedded in LCP post-crystallization,[133,164] although this may not always be possible. Specific chemicals such as MPD or high concentrations of salts and PEGs or low pH may not be compatible with the formation of LCP.[165] While LCP-SFX remains highly successful for *in meso* grown crystals,[166-169] given its delicate and composition-sensitive nature, other viscous matrices for embedding of non-LCP crystallized samples have also been explored.

The hydrophobic matrices comprise mineral oil-based grease,[148] vaseline[133] and nuclear grade grease.[170] Hydrophobic matrices are immiscible with aqueous mother liquors and therefore largely circumvent this mother liquor-matrix compatibility issue making them very versatile in this respect. In particular mineral-oil based grease has proven to be compatible with numerous protein crystal systems.[170-174] However, the general draw-backs of these matrices are relatively high X-ray background, possible dehydration of the sample and sometimes unreliable injection at room temperature (curling and adhesion of the stream to the nozzle tip/sides). Notably, at least for the mineral-oil based grease, these injection difficulties appear not to arise in vacuum.

The undesired high background of hydrophobic matrices drove the search for matrices towards the chemically different class of hydrogels. To date, several of these have been

described† – agarose,[149] hyaluronic acid,[150] hydroxyethyl cellulose[170] and PEG 8 000 000[137]. As these are largely composed of water, the background is generally lower than that of hydrophobic matrices. The use of hydrogels in vacuum is possible with the addition of cryoprotectants such as glycerol.[149] However, their hydrophilic nature and resultant miscibility with mother liquors also raises compatibility issues. Consequently the choice of hydrogel to use for a specific crystalline sample is a matter of testing and optimization.

Thermoreversible hydrogels such as Mebiol®[175] are liquid at low temperature and solid at room temperature; they are therefore attractive embedding materials as described before.[133] Poloxamers are a related copolymer series of thermoreversible hydrogels composed of triblocks of $PEG_{(x)}$-$PPG_{(y)}$-$PEG_{(z)}$ with the trade name Pluronic®.[176] In particular the F-127 compound has been used for e.g. crystallization,[177] treatment of burns[176] and pharmaceutical formulations.[178] The latter field together with the food industry also heavily employs a cellulose derivative, carboxymethyl cellulose sodium salt (NaCMC) as a thickening and gelling agent.[179,180] These two compounds, in addition to other frequently used gels in science or industry, such as polysaccharides gellan gum, agarose, kappa carrageenan and polypeptide gelatine, were subjected to an initial screening. Best results in terms of formation of a viscous and elastic gel in the presence of high concentrations of chemicals were obtained for F-127 and NaCMC. It was then tested whether F-127 and NaCMC could be used as injection matrices for serial crystallography using both vapour diffusion- and *in meso*-grown (bR) protein crystals. The vapour diffusion-grown crystals were chosen such that together they were representative of most crystallization solutions – thermolysin (TRL) was crystallized at high PEG concentration, glucose isomerase (GI) was crystallized in ammonium sulfate and lysozyme (HEWL) was representative of a high salt and low pH crystallization condition. Next, the following matrix properties were characterized: (1) compatibility with macromolecular crystals and their crystallization solutions; (2) visco-elastic properties supporting the formation of a stable stream upon extrusion; (3) X-ray background and impact on the diffraction quality of crystals; and (4) compatibility with the desired experimental set-up which can require high or low flowrates, be in vacuum or at ambient pressure etc.

3.1.1. Chemical compatibility

Hydrophilic injection matrices are miscible with protein crystallization precipitants, but mixing can alter their visco-elastic properties critical for injection and change their solubility, resulting even in precipitation. Therefore, vigorous testing of matrix – precipitant

† Hydroxyethyl cellulose and PEG 8 000 000 were published almost at the same time as results from this work.

compatibility is an essential first characterization step of any hydrophilic injection matrix. The concentrations of NaCMC and F-127 needed for the formation of a sufficiently viscous matrix suitable for injection were determined (2.5 % (*w/v)* for NaCMC, 20 % (*w/w)* for F-127 in water). Next, a highly concentrated stock gel of each compound was prepared (7 % (*w/v)* for NaCMC, 35 % (*w/w)* for F-127). The stock gels were then mixed with a selection of common crystallization reagents including salts, polymers and organic solvents. If the resulting mixture was chemically compatible (homogenous, viscous, translucent, without precipitated material), it was subjected to a simplified injection test comprising manual extrusion through a 410 µm inner diameter needle. If injection was feasible, as judged by the stability and viscosity of the extruded material (viscous enough to form and maintain a continuous stream uninterrupted by droplets or inhomogeneity), the observed injection properties were visually rated as good (+) or very good (++)(Table 12 and Table 13). Then, protein crystals were embedded in each of the two media equilibrated with the corresponding crystal storage solutions and it was checked with a light microscope whether or not the embedded crystals were stable (no cracks, no dissolution) for at least two hours. For the *in meso*-grown bR crystals, the gel was directly mixed with the harvested crystal-loaded LCP that contained only residual quantities of the crystallization precipitant which were readily absorbed by the gel.

Table 12. Compatibility of carboxymethyl cellulose sodium salt with various precipitants

Compound	Type of precipitant	Final tested concentration	Injection
Lithium sulphate	Salt	1.25 M	+
Magnesium sulfate		1.25 M	+
Ammonium sulfate		1.8 M	+
Sodium chloride		2 M	+
Polyethylene glycol 400	Polymer	35% (w/v)	++
Polyethylene glycol 2000		30% (w/v)	++
Polyethylene glycol 4000		25% (w/v)	++
Polypropylene glycol 400		25% (w/v)	++
Ethanol	Volatile organic liquid	35% (v/v)	+
2-Methyl-2,4-pentanediol (MPD)	Non-volatile organic liquid	25% (v/v)	+

NaCMC displays a very broad chemical compatibility and forms a stable stream even at high concentrations of the tested crystallization precipitants (Table 12). Embedded GI, TRL and HEWL crystals in NaCMC equilibrated with storage solutions were inspected under a light microscope and looked intact (clear sharp edges) for at least 6 h after embedding.

F-127, in contrast to NaCMC, tolerates only NaCl and low molecular weight PEG/PPG at high concentration. Other compounds, such as $(NH_4)_2SO_4$, are compatible only at lower concentrations (Table 13). Crystals of GI, TRL and HEWL in F-127 equilibrated with the appropriate storage solution appeared visually intact (clear sharp edges) for at least 2 hours after embedding. The birefringent mesophase with grown bR crystals quickly became transparent upon mixing with F-127 and crystals remained in a non-birefringent phase for at least 18 h.

Table 13. Compatibility of Pluronic F-127 with various precipitants

Compound	Type of precipitant	Final tested concentration	Injection
Ammonium sulphate	Salt	0.25 M	+
Sodium chloride		2 M	++
Polypropylene glycol 400	Polymer	25% (w/v)	+
Polyethylene glycol 400		23% (w/v)	++
Polyethylene glycol 2000		7% (w/v)	+

When comparing the chemical compatibility of NaCMC and F-127 to established hydrophilic injection matrices, NaCMC and F-127 can tolerate higher concentration of NaCl (2M) than agarose (1M). Moreover, NaCMC is also compatible with higher concentrations of $(NH_4)_2SO_4$ (1.8 M) than agarose (1.25 M)[149]. The compatibility of NaCMC and F-127 with PEGs and organic solvents listed in Table 12 and Table 13 cannot be directly compared with agarose as no detailed information was provided on the concentrations used in the latter case[149]. Likewise, only limited comparisons can be made with hyaluronic acid, as it was only equilibrated with the crystallization solution (presumably final concentrations 7% (w/v) sodium chloride, 2% (w/v) PEG 6000 and 0.05 M sodium acetate (pH 3.0)) of lysozyme and water in case of proteinase K crystals, respectively.[150] No further precipitant compatibilities were described, possibly due to the very high cost of the compound. Little information is also provided on the chemical compatibility of hydroxyethyl cellulose[170] and PEG 8 000 000[137].

3.1.2. Injection

The formation of a stable stream upon extrusion is another critical requirement for a useful injection matrix. The stream needs to run continuously, both mechanically (no bubbles, liquid droplets or other breaks) and temporally, i.e. with constant velocity. The latter has two aspects: First, in general, a stable and appropriate stream velocity ensures that sample exposed to and subsequently damaged by the X-ray beam proceeds out of the interaction zone before the next X-ray exposure ensues at the chosen data collection rate (*f*). Second, time-resolved experiments, for example using an optical pump — X-ray probe scheme for

data collection, have additional requirements (see scheme in Figure 4). The probed crystals can be activated only by the pump pulse that preceded the probe pulse by a desired time-delay (Δ t), and these pumped crystals must clear the X-ray probe region before the next probe pulse arrives (Δ t + 1/*f*). This requirement sets a *minimal* stream velocity for a given *f*. In addition, a *maximal* velocity limit is set by the requirement that the pumped crystal has not moved beyond the X-ray probe region before the associated pump pulse arrives at Δ t. This is particularly critical in case of long time-delays (Δ t in the ms range) and high repetition rates (*f* in the 60 – 120 Hz range, with $1/f > \Delta t$). In the ideal case, data collection is performed at the maximal possible repetition rate *f* for maximal time-efficiency and the velocity of the stream is adapted accordingly, by adjusting the flow rate. However, if the extruded stream is stable only within a narrow range of velocities, the repetition rate needs to be decreased. Thus, knowledge of the stability of the stream velocity and its dependency on flow rate is important. So far, these parameters have been largely disregarded.[87] Previous characterizations of injection media described in more or less detail their chemical compatibility and X-ray background based on serial data collection at synchrotron[133] or XFEL[148-150] sources, but not their flow properties. For instance, the grease matrix[148] has very unstable injection properties, affecting efficient use of beam time and sample and complicating time resolved experiments.

Therefore, to obtain this important information on the injection properties of the media the dependence of the stream velocity (in mm/s) on the flow rate (in µl/min) of the NaCMC and F-127 matrices with embedded crystals was examined to judge their suitability also for time-resolved experiments by identifying the range of stable stream velocities. Importantly, injection with no or small embedded crystals (<10 µm) is typically more stable compared to injection with larger crystals (> 20 µm), which disturb the extrusion more. Movies of the streams extruding at given flow rates were recorded and the stream velocities were calculated by measuring distances that given particles travelled within a certain time frame. The measurements were performed at ambient pressure in air using our HVE injector. Injection at ambient pressure is more challenging than in vacuum, since the latter seems to ameliorate attachment of extruding material to the nozzle tip (a common problem with grease injection). On the other hand, evaporative cooling of the extruded material *in vacuo* can hamper data collection. Dehydration of both NaCMC and F-127 when injected into vacuum (8.6 mbar) was observed, which can be prevented by the addition of stabilizers or cryoprotectants. For example, F-127 mixed with LCP (ratio 1+3) or NaCMC supplemented with 20% glycerol can be injected into vacuum without freezing problems.

3.1.2.1. Carboxymethyl cellulose sodium salt (NaCMC)

NaCMC forms stable streams with a wide range of precipitants. As an injection matrix, however, NaCMC is particularly sensitive to the size of embedded crystals, with larger crystals notably disturbing the stream stability. In order to enable using NaCMC for this regime of larger crystals, which may be necessary for synchrotron experiments, the injection conditions for this challenging case were optimized by applying the following measures 1) decreasing crystals concentration (from 5% (*v/v)* to 2.5% or less); 2) choosing a larger ID nozzle (150 μm)[‡] and 3) decreasing the precipitant concentration if possible. In this way stable injection was achieved for all three samples (GI, HEWL, TRL). The velocity of the stream depends linearly on the flow rate and the generally small standard deviation indicates that the velocity is stable (Figure 7a). This demonstrates that flow rate settings can indeed be used to control stream velocity over a very large range (0.13 - 4.90 mm/s). The dependence of the stream velocity on the flow rate varies slightly between samples due to small differences in jet diameter – the larger the stream diameter, the slower the stream at a given flow rate.

The stream diameter depends on the crystal size and on the precipitant. Given this variability it is necessary to optimize sample preparation and injection for each sample individually, starting with the three parameters listed above. Due to the stable injection properties (constant velocity and stream diameter), jet velocities can be estimated reasonably well based on the diameter of the stream and the known flow rate, thus allowing live feedback during the experiment at the synchrotron / XFEL.

3.1.2.2. Hydrogel Pluronic® F-127

F-127 has specific viscoelastic and textural properties (spreadability, creaminess) that support formation of very stable streams. Precipitant, crystal size and concentration have less impact on stream stability and velocity for F-127 than for NaCMC (Figure 7b). The velocities showed a linear dependence on the flow rate and are stable for a large range (0.12 - 6.53 mm/s). The dependence of the velocity of the flow rate is nearly identical for the TRL and HEWL samples but differs slightly for the GI sample as ammonium sulfate alters the visco-elastic properties of F-127 in a concentration-dependent manner. Importantly, F-127 can also be added post-crystallization to a crystal-loaded birefringent mesophase in order to adjust both the injection and mesophase properties or to dilute the sample in one step. This is a simpler and more viable protocol than adding liquid paraffin[87], where first the dilution or

[‡] Using nozzles with larger IDs typically requires lowering the crystal concentrations as the stream diameter together with the focal size of the X-ray beam defines the volume that contains ideally one crystal per X-ray exposure.

mesophase adjustment with LCP is performed and only then the injection additive paraffin is added. This not only takes time but requires multiple mixing steps which can also damage the crystals. Indeed, the addition of F-127 to bR crystals in LCP allowed to finely control the stream velocity by the flow rate (Figure 7c) and stabilized the erratic flow behaviour observed for bR crystals in pure LCP (Figure 7d). The optimal mixing ratio of LCP and F-127 is 3+1 to 1+1 by volume, the more F-127 is added, the thicker the resulting stream and therefore the lower its velocity.

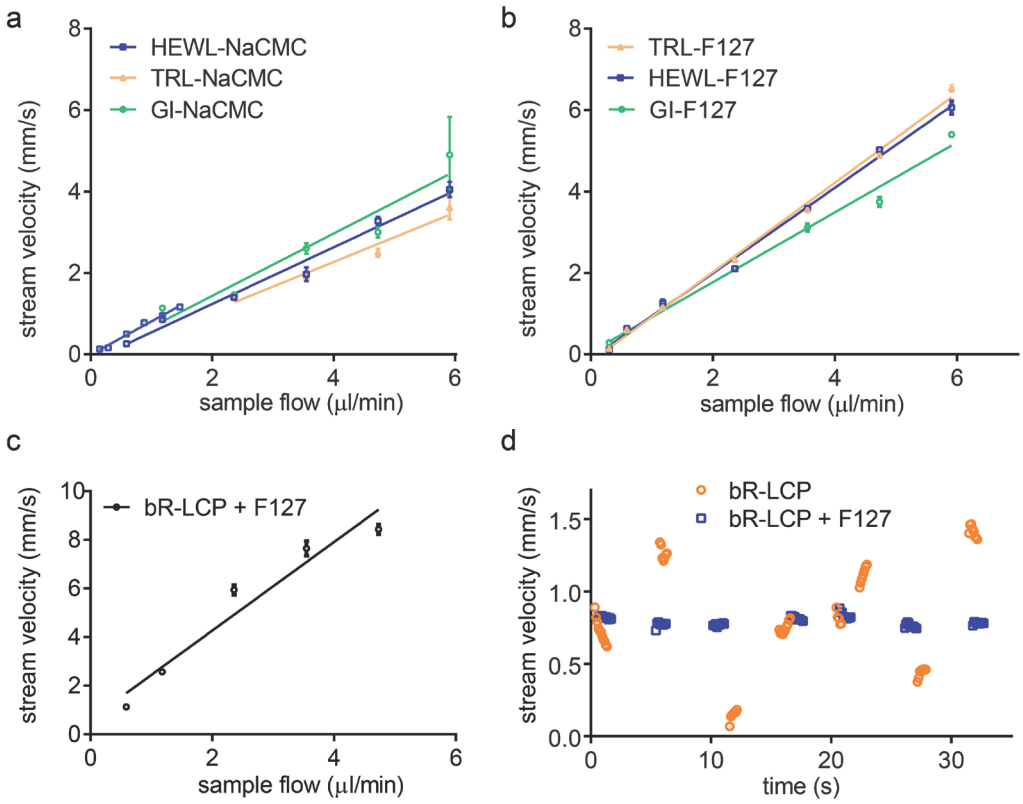

Figure 7. Measurements of stream velocity and its dependence on the flow rate (a-c) and time (d). a-c, The average velocities at various sample flow rates were plotted and fitted with a simple linear regression. The standard deviation is plotted for all velocity values, but it is not displayed if it is smaller than the size of the symbol. Stream velocities of NaCMC (**a**) and F-127 (**b**) as measured for different flow rates for various embedded crystals (GI, HEWL and TRL, represented by green dots, blue squares and yellow triangles, respectively). Embedded HEWL crystals in NaCMC were measured in both small and large sample reservoir injectors, hence the two blue plots covering lower and higher flow rates in part (**a**). **c**, Stream velocity of bR-LCP mixed with F-127 (in a 3+1 ratio) measured at different flow rates. **d**, At a constant flow rate (0.3 and 0.35 µl min^{-1} for the bR-LCP sample without and with F-127, respectively) at intervals of approximately 5 s, 5–10 instantaneous stream velocities were calculated and plotted for both samples. Data points for bR-LCP and bR-LCP with F-127 are represented as orange circles and blue squares, respectively. This figure was published in Kovacsova *et al.*[142]

For comparison, the two published hydrophilic injection matrices described in the literature, hyaluronic acid[150] and agarose[149] were tested in the ambient pressure injection setup using 100 µm ID nozzles. Injection of 12% *(w/v)* aqueous hyaluronic acid could easily be reproduced based on the description by Sugahara and co-workers, who used it for XFEL data collection at ambient pressure at SACLA[150]. Conrad *et al.* used agarose as a carrier medium for XFEL data collection in vacuum and at ambient pressure at the CXI endstation of LCLS at SLAC[149]. Injection of 5.6 % agarose with 30% glycerol was in line with their observation that injection at ambient pressure is much more unstable. A stable gel-stream was frequently disrupted by liquid droplets, indicating that the mixture was not homogenous, despite extensive mixing.

3.1.3. Serial crystallography data collection – diffraction and background

The serial crystallography experiments were performed at the Swiss Light Source, X10SA (PXII) beamline using the HVE injector[133] to compare NaCMC and F-127 to the standard high viscosity embedding medium grease.[148] X-ray background and crystal diffraction quality were measured, in all cases with soluble protein crystals embedded in the carrier matrix. The combination of F-127 and LCP with membrane protein crystals of bR was compared to plain LCP with bR crystals.

NaCMC has very low background scattering with a weak diffuse ring at 2.6 – 4 Å. This is similar to other hydrophilic matrices (hyaluronic acid[150], agarose[149], hydroxyethyl cellulose[170], PEG 8 000 000[137]) and much lower than for grease even when using larger stream diameter (for 150 µm ID capillary: NaCMC: Ø220-230 µm; grease: Ø135-145 µm in Figure 8a,b). The background of F-127 is comparable in magnitude to grease and LCP (for 100 µm ID capillary: F-127: Ø200-230 µm; grease: Ø80-100 µm Figure 8c, d, e, f). The resolution range of the F-127 diffuse ring is around 2.8 – 5 Å and differs from grease's diffuse ring around 4.3 – 6 Å which is dominated by a strong Debye-Scherrer ring at 4.9 Å. High resolution diffraction from all samples was observed and complete data sets were collected in two hours using less than 0.5 mg crystalline protein for each data set. The crystallographic analysis of a similar number of indexed diffraction patterns collected from the corresponding grease and NaCMC/F-127 embedded samples, as well as the LCP and LCP+F-127 embedded samples, yield similar data quality (crystallographic data statistics are listed in Table 14).

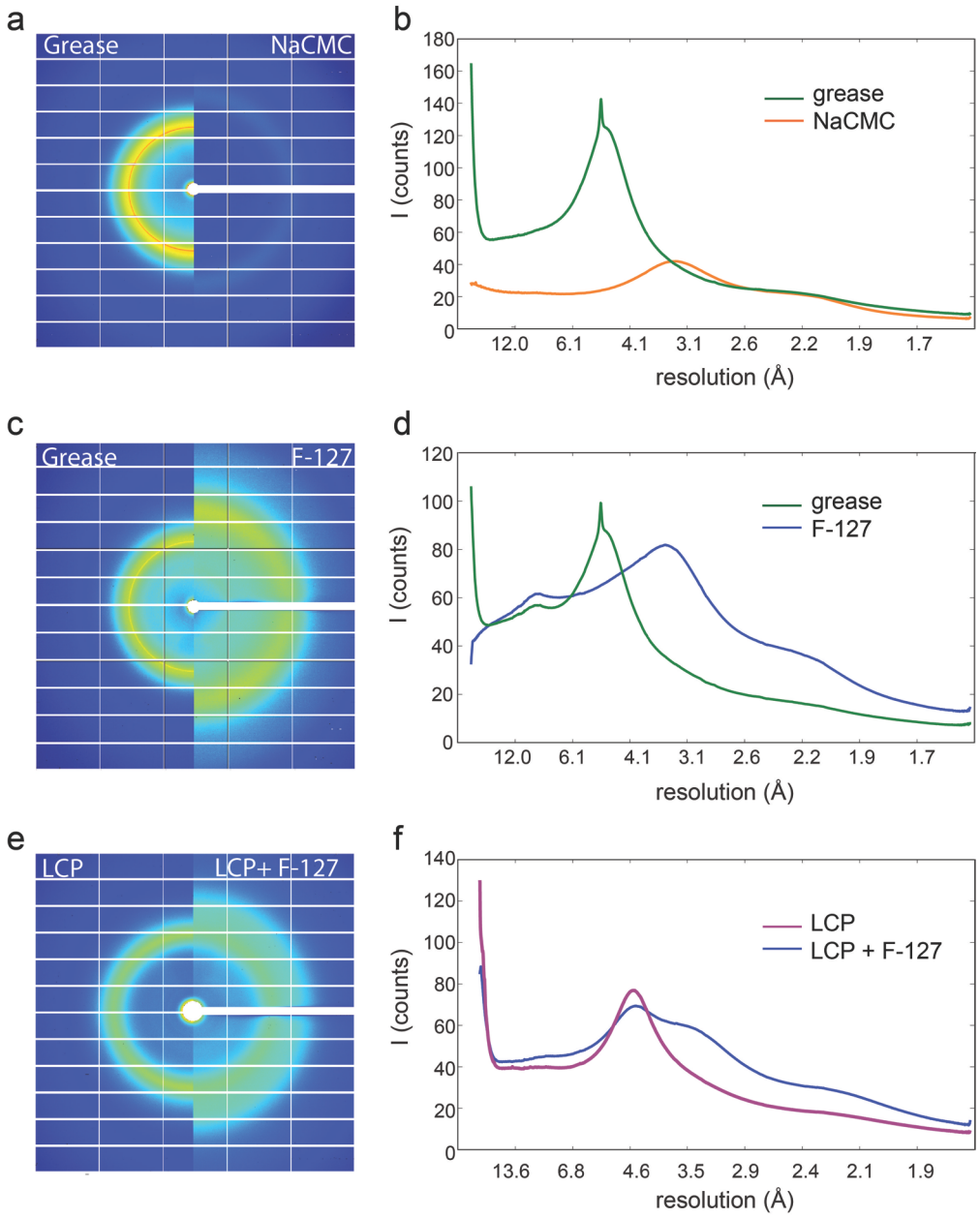

Figure 8. Background scattering of different media. Background scattering of NaCMC (**a, b**) and F-127 (**c, d**) compared with grease, and LCP compared with a 1:1 LCP and F-127 mixture (**e, f**). **a, c, e**, Median background images of NaCMC (**a**) and F-127 (**c**) compared with grease and F-127+LCP compared with LCP (**e**). Each image is composed of two halves, that on the left being that of the standard medium (grease or LCP) and that on the right being that of the tested medium. **b, d, f**, Radially integrated background images plotted against resolution. The green line represents grease (**b, d**), the orange line NaCMC (**b**) and the blue line F-127 (**d**). In f, the purple line represents LCP and the blue line represents LCP+F-127. The following capillary diameters were used, yielding the measured stream diameters: **a**, **b**: capillary ID 150 µm, NaCMC diameter 220–230 µm, grease 135–145 µm; **c**, **d**: capillary ID 100 µm, F-127 diameter 200–230 µm, grease 80–100 µm; **e**, **f**: capillary ID 100 µm, LCP+F-127 diameter ~200 µm, LCP ~100 µm. This figure was prepared by Thomas Barends for Kovacsova *et al.*[142]

Table 14. Crystallographic statistics for all serial diffraction data sets

Data set	HEWL - NaCMC	HEWL - grease	GI – F-127	GI – grease	TRL – NACMC**	TRL - grease	TRL – F-127	TRL - grease	BR- LCP – F-127	BR - LCP
Nozzle diameter	150 µm	100 µm	100 µm	100 µm	150 µm	150 µm	100 µm	100 µm	100 µm	100 µm
SLS Beamline	PXII	PXII	PXII	PXII	PXII	PXII	PXII	PXII	PXII	PXII
Wavelength (Å)	1.033	0.954	1.033	1.033	1.033	1.033	1.033	1.033	1.033	1.033
Space group	$P4_32_12$	$P4_32_12$	I222	I222	$P6_122$	$P6_122$	$P6_122$	$P6_122$	$P6_3$	$P6_3$
Unit cell parameters: a, b, c (Å)	79.0, 79.0, 38.1	79.0, 79.0, 38.1	93.0, 98.6, 101.8	93.0, 98.7, 101.9	93.0, 93.0, 130.0	93.0, 93.0, 130.0	93.0, 93.0, 130.2	93.1, 93.1, 130.0	62.2, 62.2, 110.7	62.2, 62.2, 109.6
α β γ (°)	90, 90, 90	90, 90, 90	90, 90, 90	90, 90, 90	90, 90, 120	90, 90, 120	90, 90, 120	90, 90, 120	90, 90, 120	90, 90, 120
No. collected images	26310	23818	24412	28084	62926	20456	11188	18156	13285	42457
Hit rate	36 %	91 %	86 %	57 %	91 %	94 %	55 %	58 %	93 %	98 %
No. crystal hits/ indexed images*	9472/ 5362	21715/ 5348	20961/ 8603	16122/ 8593	57226/ 4556	19222/ 4529	6124/ 4549	10533/ 4529	12383/ 4229	41701/ 4218
Indexing rate§	57 %	25 %	41%	57%	8%	24%	74%	43%	34%	10%
Resolution range	25.0-1.9	25.0-1.9	25.0-2.0	25.0-2.0	25.0-2.3	25.0-2.0	25.0-2.0	25.0-2.0	25.0-2.3	25.0-2.3
Completeness (%)	99.9 (100)	99.9 (100)	99.9 (100)	99.9 (100)	99.9 (100)	99.9 (100)	99.9 (100)	99.9 (100)	99.9 (100)	99.9 (100)
Multiplicity	328.5 (262.3)	252.2 (180.7)	197.1 (119.5)	185.8 (112.8)	570.4 (470.3)	241.2 (154.9)	353.3 (217.8)	277.3 (167.8)	149.3 (106.4)	191.6 (130.7)
‹I/σ (I)›	11.0 (5.1)	9.5 (8.6)	5.3 (1.7)	5.1 (2.6)	10.0 (2.2)	4.9 (3.3)	5.3 (0.9)	5.3 (2.3)	6.5 (2.8)	6.5 (1.9)
R_{mrgd-F}	18.3 (47.7)	15.1 (17.3)	31.5 (123.9)	27.2 (70.2)	23.6 (104.7)	23.4 (48.4)	43.3 (242.7)	31.0 (89.1)	24.3 (73.5)	28.9 (120.1)
$CC_{1/2}$	94.4 (84.8)	87.7 (89.9)	90.8 (48.2)	81.2 (50.9)	96.9 (74.9)	82.3 (59.8)	92.6 (42.5)	84.8 (50.5)	94.3 (67.6)	94.9 (62.1)
Overall Wilson B factor ($Å^2$)	29.9	20.2	28.1	22.4	40.3	16.4	34.0	22.2	42.2	47.8

* A similar number of randomly chosen images was taken for comparison

** Worse statistics due to very high stream velocity required for stable flow under the conditions of the experiment

§ Differences in indexing rates are related to sample preparation. A too high crystal concentration in the sample resulted in many multiple-lattices containing diffraction images in the data set (as manifested by a very high hit rate). These were not always indexed by nXDS, thus giving a low indexing rate.

3.2. Ultrafast light-induced events in bacteriorhodopsin using time-resolved serial crystallography

3.2.1. Sample preparation, injection and pre-illumination

Time-resolved SFX experiments require large quantities of well-diffracting microcrystals. To this end, large quantities of bR protein were purified and bR crystals were prepared using the crystallization condition published previously with minor modifications (Figure 9).[134] Pluronic F-127 was used as an additive to improve injection properties. The target stream velocity was 4 mm/s. At a 10 Hz X-ray repetition rate the stream will displace by 400 µm in the 100 ms between consecutive X-ray exposures (see Figure 4, D = 400 µm). This displacement is sufficient to prevent light-contamination from a 100 µm diameter optical laser spot centred 20-30 µm downstream of the X-ray spot, as verified during the TR-SFX experiment by an absence of light-induced structural changes data from unpumped images.

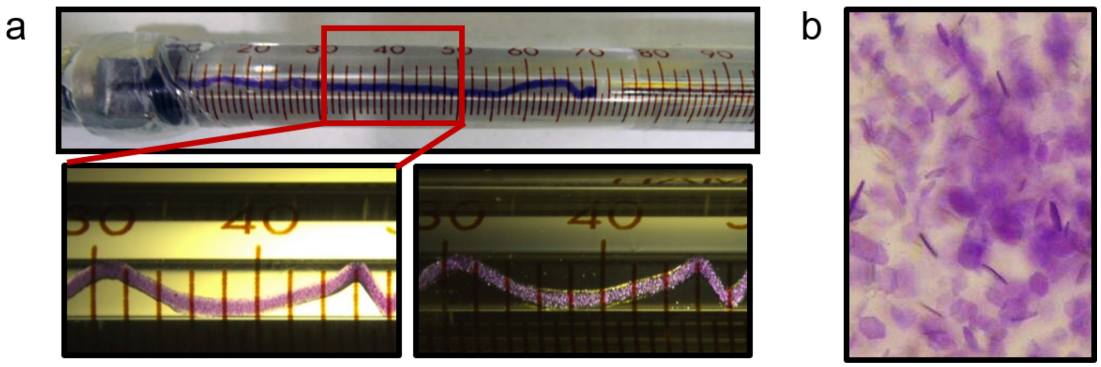

Figure 9. Large-scale LCP crystallization. a, A 100 µL Hamilton syringe filled with a crystal-loaded LCP string (purple) surrounded by mother liquor. The inset shows a microscope picture of the purple crystals under illumination with white light (left) and with polarized light (right). **b,** The purple hexagonally-shaped bR crystals of ~ 20 µm in the longest dimension.

Depending on the light conditions, bR contains different quantities of all-*trans* and 13-*cis* retinal, ranging from 100% all-*trans* retinal in fully light-adapted bR to a ~50:50 mixture of both configurations in the fully dark-adapted sample. Complete light-adaptation can be achieved by continuous illumination for at least several seconds. As only the all-*trans* retinal undergoes the functional photocycle, maximal light-adaptation of the bR microcrystals was necessary. One possibility for light adaption is to illuminate the crystals when they are in the Hamilton syringe just before injector loading.[87,181] However, the typical time needed to proceed from injector loading to actual data collection is about 15-30 min. Given the dark-adaptation half-life of about 20 min in bR microcrystals, diffraction data would then be collected on an essentially dark-adapted sample. Moreover, due to the high optical density of bR crystals, it is necessary that the sample be sufficiently thin to ensure that most crystals to

be exposed to light (ID 1.4 mm for a 100 µl syringe). For these reasons, it was decided against performing the light-adaptation of bR microcrystals in the syringe prior to injector loading and instead, a protocol for on-line pre-illumination was developed. Here, the crystals are loaded into the injector first and then illuminated while travelling through the transparent injector capillary (ID 100 µm) equipped with a metal sleeve having a 22 mm window for illumination (Figure 6). The relative content of the retinal stereoisomers was determined by retinal extraction and HPLC separation. This yielded an average composition of a non-illuminated, dark-adapted sample to be 40-45 % all-*trans* and 55-60 % 13-*cis* retinal (Figure 10a). Pre-illumination increased the all-*trans* retinal content considerably, to about 65-80 % (Figure 10b). 100% all-*trans* retinal was never observed in the crystalline sample, likely due to two reasons. First, during the 3-5 min that it took to collect enough injected material for analysis, the sample that was already in the collection tube started to dark-adapt, decreasing the average all-trans content to at least ~ 90-95 %. Second, the sample likely contains small amounts of aggregated, not crystallized protein. This is deduced from optical spectra showing a small peak at around 370 nm. It is very small in the protein solution spectrum and increases in the crystallized bR sample spectrum with respect to the main peak at ~ 570 nm. In retinal extraction, both crystallized and uncrystallised protein contribute to the signal the analysis. If some of the aggregated protein contains 13-cis, e.g. because light-adaptation is not functional anymore, this will shift the results towards a higher 13-*cis* content.

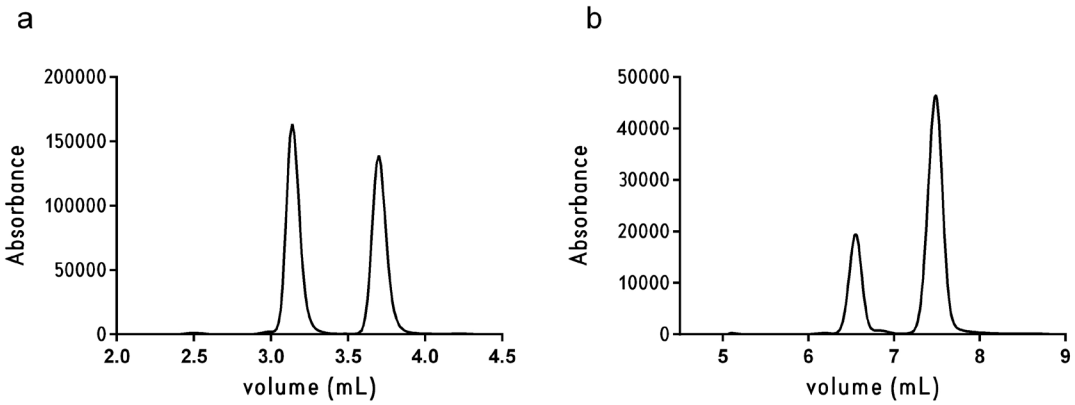

Figure 10. Chromatograms of the retinal extraction. a, A dark-adapted microcrystalline bR sample with 13-*cis* and all-*trans* retinal eluting at 3.13 mL and 3.70 mL and a peak area of 702518 and 637415, respectively. This gives a relative composition of 58 % 13-*cis* and 42 % all-*trans* retinal. **b**, After online pre-illumination of the microcrystalline bR sample, the retinal composition shifted to 32 % 13-*cis* and 68 % all-*trans* retinal (elution volume 6.54 mL and 7.48 mL and peak area 151534 and 403394, respectively).

Light-scattering from a circular jet

Based on experimental and theoretical work, the relative amount of optical light scattered from a 100 µm circular bR-LCP jet was estimated to be about 20 %, where ~ 14 % are due to

the bR crystals, ~ 2 % are due to LCP and ~ 5 % are due to reflection at the various interfaces of the circular jet.

3.2.2. Analysis of crystal structures

The TR-SFX diffraction experiment was performed in an optical pump- X-ray probe set-up at the CXI endstation at the LCLS XFEL source in Stanford, CA, USA. Crystallographic data of the bR ground state (unpumped/ dark) and of the intermediates at following time-delays we obtained: 12 sub-s time-points (0.24, 0.33, 0.39, 0.43, 0.46, 0.49, 0.53, 0.56, 0.59, 0.63, 0.68 and 0.74 ps), 1 ps, 3 ps, 10 ps and 33 ms. The sub-ps time points were all collected at a nominal time-delay of 0.5 ps. There is an intrinsic shot-to-shot variation of ~250 fs in the synchronization of the arrival of the X-ray and the optical pulse. Therefore, information from a diagnostic beamline tool, the timing tool, was used to determine the exact time delay for each image. The sorted 40 000 images were then binned into 12 overlapping bins containing 10 000 images each. Given the nominal setting of 0.5 ps, the data is more finely sliced in this region. The crystallographic statistics are in Table 15.

The resolution of the diffraction data is 1.8 Å, which is a prerequisite for being able to observe small structural changes. In line with previous work, the ground state structure contains a largely planar all-*trans* retinal (Figure 11a) that is connected via the PSB to an extensive H-bonding network (Figure 11b). The pentagonal cluster formed by Wat402, Asp85, Asp212, Wat 401 and Wat406 is well resolved, and so are the other internally bound water molecules. The structure is in good agreement with other ground state bR structures, either from synchrotron sources (e.g. the first high resolution bR structure (RMSD of Cα 0.460)),[182] or from the XFEL (RMSD of Cα 0.140).[87]

High-quality umpumped data and a correct ground state structure are important for several reasons. First, the unpumped data is used to calculate difference electron density maps from the pumped and unpumped data. The intensity differences between these two data sets are used to calculate extrapolated density maps of the time-resolved data. Second, the unpumped data is also a two-fold negative control. Under continuous illumination of bR, the M intermediate is accumulated. M is characteristic of large structural changes and decays at ~ 100 ms in the crystal.[87] The absence of these light-induced changes in the unpumped data means that there is no unwanted laser light illumination (contamination) in the set-up. This can either originate from the pre-illumination laser, if e.g. the “dark zone” would not provide enough time for the crystals to decay to the ground state before they reached the X-ray interaction region. Or, if the data is collected in a laser-on laser-off sequence, the light contamination can originate from the pump laser (for a graphical explanation see Figure 4).

Table 15. Crystallographic statistics

	dark, cell 1	dark, cell 2	33 ms		1 ps	3 ps	10 ps
Data collection							
Space group	$P6_3$	$P6_3$	$P6_3$		$P6_3$	$P6_3$	$P6_3$
No. indexed images	22,485	69,518	9,022		11,590	9,739	8,997
Cell dimensions (Å)							
a, *b*, *c* (Å)	61.7, 61.7, 109.2	62.1, 62.1, 110.5	62.1, 62.1, 109.6		61.7, 61.7, 109.3	62.0 62.0, 110.3	61.7, 61.7, 109.4
α, β, γ (°)	90, 90, 120	90, 90, 120	90, 90, 120		90, 90, 120	90, 90, 120	90, 90, 120
Resolution (Å)	20-1.7	20-1.8	20-2.1		20-1.8	20-1.9	20-1.8
	(1.8-1.7)	(1.9-1.8)	(2.2-2.1)		(1.9-1.8)	(2.0-1.9)	(1.9-1.8)
R_{split}	0.069	0.057 (0.623)	0.143		0.108	0.124	0.119
	(0.543)		(0.714)		(0.793)	(0.751)	(0.607)
CC*	0.999	0.999	0.995		0.997	0.996	0.996
	(0.920)	(0.893)	(0.862)		(0.845)	(0.854)	(0.901)
I / σI	9.9 (2.0)	11.6 (1.8)	5.3 (1.5)		6.8 (1.4)	5.9 (1.4)	6.4 (1.7)
Completeness (%)	100 (100)	100 (100)	100 (100)		100 (100)	100 (100)	100 (100)
Redundancy	476 (380)	795 (237)	144 (92)		231 (165)	141 (90)	187 (134)
Estim. twinning fraction (ML)	0.032	0.054	0.066		0.068	0.046	0.074
Refinement				**Real-space refinement**			
Resolution (Å)	20-1.7	20-1.8	20-2.1	Map resolution (Å)	20-1.8	20-1.9	20-1.8
No. reflections	25882	22376	13984	*f*	0.15	0.10	0.10
R_{work} / R_{free}	0.186/0.214	0.179/0.216	0.192/0.244	Model/map fit (CC_{mask})	0.8408	0.8104	0.7785
No. atoms				No. atoms			
Protein	1786	1786	2024	Protein	1786	1786	1786
Ligand/ion	21 (retinal)	21 (retinal)	42 (retinal A, B)	Ligand/ion	21 (retinal)	21 (retinal)	21 (retinal)
	206 (lipids)	206 (lipids)	206				
Water	43	38	39	Water	36	36	36
B-factors (Å^2)							
Protein	28.7	33.1	36.3				
Ligand/ion	19.4 (retinal)	23.6 (retinal)	24.5, 24.5 (retinal A,B)				
	47.0 (lipids)	50.3 (lipids)	52.9 (lipids)				
Water	39.7	45.0	46.3				
R.m.s. deviations				R.m.s. deviations			
Bond lengths (Å)	0.006	0.007	0.007	Bond lengths (Å)	0.005	0.005	0.005
Bond angles (°)	1.082	1.047	1.121	Bond angles (°)	0.901	0.910	0.792

	0.24 ps	0.33 ps	0.39 ps	0.43 ps	0.46 ps	0.49 ps
Data collection						
Space group	$P6_3$	$P6_3$	$P6_3$	$P6_3$	$P6_3$	$P6_3$
No. indexed images	10,000	10,000	10,000	10,000	10,000	10,000
Cell dimensions (Å)						
a, *b*, *c* (Å)	62.1, 62.1, 110.5	62.1, 62.1, 110.5	62.1, 62.1, 110.5	62.1, 62.1, 110.5	62.1, 62.1, 110.5	62.1, 62.1, 110.5
α, β, γ (°)	90, 90, 120	90, 90, 120	90, 90, 120	90, 90, 120	90, 90, 120	90, 90, 120
Resolution (Å)	20-1.8 (1.9-1.8)	20-1.8 (1.9-1.8)	20-1.8 (1.9-1.8)	20-1.8 (1.9-1.8)	20-1.8 (1.9-1.8)	20-1.8 (1.9-1.8)
R_{split}	0.120 (0.751)	0.119 (0.768)	0.119 (0.786)	0.118 (0.789)	0.118 (0.788)	0.120 (0.779)
CC*	0.996 (0.868)	0.996 (0.864)	0.996 (0.854)	0.996 (0.847)	0.997 (0.845)	0.996 (0.845)
$I / \sigma I$	6.0 (1.4)	6.1 (1.4)	6.0 (1.4)	6.0 (1.4)	6.0 (1.4)	6.0 (1.4)
Completeness (%)	100 (100)	100 (100)	100 (100)	100 (100)	100 (100)	100 (100)
Redundancy	139 (97)	139 (97)	138 (96)	138 (96)	138 (96)	137 (96)
Estim. twinning fraction (ML)	0.070	0.067	0.094	0.096	0.097	0.091
Real-space refinement						
Map resolution (Å)	20-1.8	20-1.8	20-1.8	20-1.8	20-1.8	20-1.8
f	0.15	0.15	0.15	0.15	0.15	0.15
Model/map fit (CC_{mask})	0.8364	0.8365	0.8374	0.8321	0.8387	0.8368
No. atoms						
Protein	1786	1786	1786	1786	1786	1786
Ligand/ion	21 (retinal)	21 (retinal)	21 (retinal)	21 (retinal)	21 (retinal)	21 (retinal)
Water	36	36	36	36	36	36
R.m.s. deviations						
Bond lengths (Å)	0.007	0.005	0.006	0.005	0.006	0.006
Bond angles (°)	0.986	0.905	0.944	0.873	0.954	0.954

	0.53 ps	0.56 ps	0.59 ps	0.63 ps	0.68 ps	0.74 ps
Data collection						
Space group	$P6_3$	$P6_3$	$P6_3$	$P6_3$	$P6_3$	$P6_3$
No. indexed images	10,000	10,000	10,000	10,000	10,000	10,000
Cell dimensions (Å)						
a, *b*, *c* (Å)	62.1, 62.1, 110.5	62.1, 62.1, 110.5	62.1, 62.1, 110.5	62.1, 62.1, 110.5	62.1, 62.1, 110.5	62.1, 62.1, 110.5
α, β, γ (°)	90, 90, 120	90, 90, 120	90, 90, 120	90, 90, 120	90, 90, 120	90, 90, 120
Resolution (Å)	20-1.8 (1.9-1.8)	20-1.8 (1.9-1.8)	20-1.8 (1.9-1.8)	20-1.8 (1.9-1.8)	20-1.8 (1.9-1.8)	20-1.8 (1.9-1.8)
R_{split}	0.120 (0.790)	0.119 (0.827)	0.120 (0.841)	0.119 (0.863)	0.121 (0.864)	0.122 (0.858)
CC*	0.996 (0.840)	0.996 (0.827)	0.996 (0.821)	0.986 (0.863)	0.986 (0.832)	0.986 (0.858)
I / σI	6.0 (1.4)	5.9 (1.3)	5.9 (1.3)	5.9 (1.3)	5.9 (1.3)	5.9 (1.3)
Completeness (%)	100 (100)	100 (100)	100 (100)	100 (100)	100 (100)	100 (100)
Redundancy	137 (96)	136 (95)	136 (95)	136 (95)	134 (94)	133 (93)
Estim. twinning fraction (ML)	0.097	0.090	0.067	0.101	0.090	0.089
Real-space refinement						
Map resolution (Å)	20-1.8	20-1.8	20-1.8	20-1.8	20-1.8	20-1.8
f	0.15	0.15	0.15	0.15	0.15	0.15
Model/map fit (CC_{mask})	0.8374	0.8374	0.8347	0.8257	0.8395	0.8398
No. atoms	1786	1786	1786	1786	1786	1786
Protein	21 (retinal)	21 (retinal)	21 (retinal)	21 (retinal)	21 (retinal)	21 (retinal)
Ligand/ion	36	36	36	36	36	36
Water						
R.m.s. deviations						
Bond lengths (Å)	0.006	0.006	0.005	0.005	0.005	0.005
Bond angles (°)	0.934	0.942	0.891	0.862	0.901	0.889

This table was prepared by Thomas Barends for the manuscript Nass Kovacs *et al.*

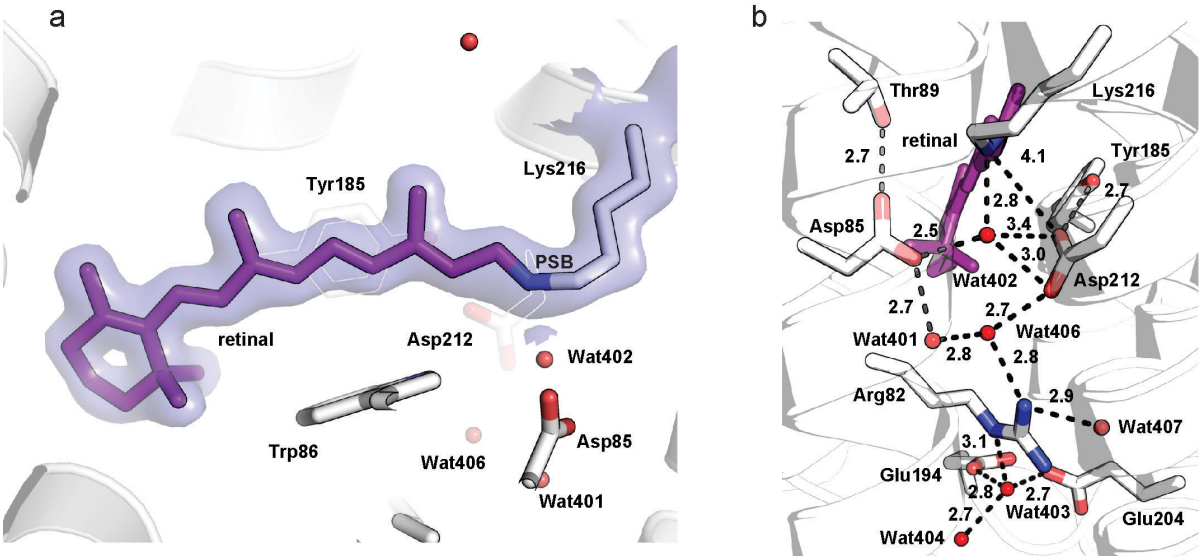

Figure 11. Crystal structure of the ground state. a, View on the retinal (purple) with surrounding residues and water molecules (red spheres). The electron density map shown as a purple surface is contoured at 1.0 σ. **b**, The hydrogen-bonding network surrounding retinal and extending to the extracellular proton-release site. Distances are given in Å.

Light-induced sub-ps structural changes

Changes in the retinal

Structural rearrangements in the retinal are observed already in the structure of the first time-point of 0.24 ps. The planarity of the retinal polyene chain is distorted, which is most pronounced at the twisted double bond C13=C14, and further at double bonds C9=C10 and C15=N and in distortion of the Lys216 side chain (Figure 12a,b). The C14 atom displaces in time from the retinal plane in an exponential fashion (τ ~245 fs, Figure 12c) as the torsion around the C13=C14 bond proceeds. The torsion angles of the C13=C14 double bond and neighbouring double bonds are listed in Table 16. The change in the torsion angle -C13=C14- progresses steadily until 0.49 ps (-126°), which is the most twisted sub-ps value, and the subsequent sub-ps values decrease and rather stagnate in a less twisted (~ -134°) configuration. The angle represents an average of the light-induced changes occurring at this bond and as some molecules will form 13-*cis* and some will decay back to all-*trans*, this average represents a mixture of conformations, not one real structure.

Further, the change in values of following torsion angles in the retinal in time could be described with a sinusoidal function. Oscillatory modulations are observed both locally, as in the torsion angle between the β-ionone ring and the polyene chain (C18-C5=C6-C7) with a frequency of ~120 cm^{-1}, and globally, as the motion of the entire retinal skeleton was manifested in the low frequency oscillation of the torsion angle between terminal methyl groups (C18 and C20; angle C18-C5-C13-C20) of ~90 cm^{-1} (Figure 12d, e)

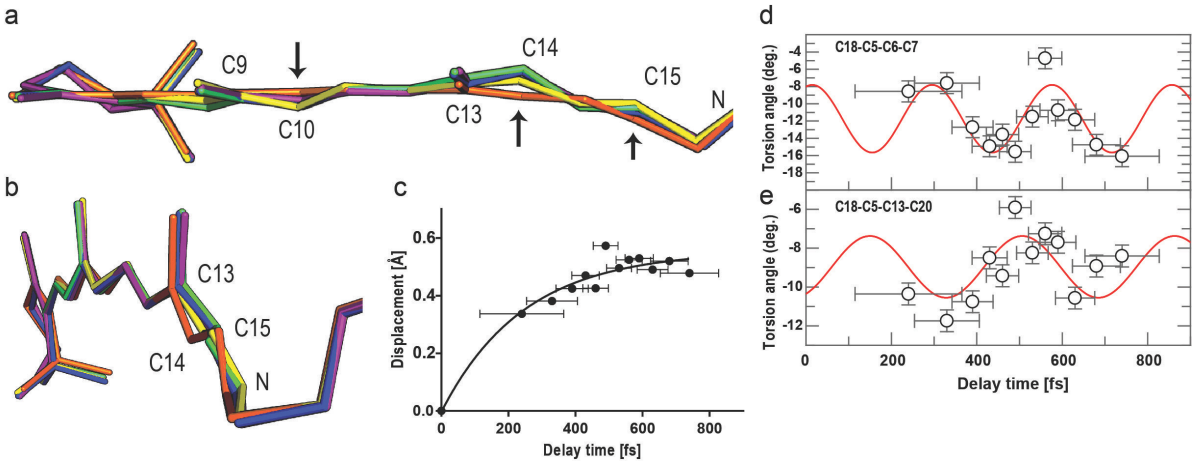

Figure 12. Structural changes in the retinal on the sub-ps timescale. a, Top view on the retinal. Structure in orange, yellow, green, blue and violet shows the ground state, 0.24 ps, 0.49 ps, 0.56, 0.68 ps structure, respectively. The black arrows highlight the light-induced retinal twisting at specific positions (C10, C14, C15). **b**, Side view on the retinal, colours as in a. **c**, Exponential displacement of the retinal C14 atom in time from the dark-state retinal plane. **d, e,** The torsion angles between the β-ionone ring and the beginning (C18-C5=C6-C7 torsion angle, **d**) and end (C18-C5-C13-C20 torsion angle, **e**) of the polyene chain are plotted in time. The oscillatory modulation of the angles with frequencies of 119±-9 cm^{-1} (**d**) and 93±14 cm^{-1} (**e**) further visualize the twisting of the entire retinal.

Table 16. Torsion angle values.

Delay time [fs]	C10-C11=C12-C13[°]	C12-C13=C14-C15 [°]	C14-C15=N-C [°]
0	-177.6	-178.0/-150.0*	-156.7
240	-167.9	-150.5	-157.5
330	-164.4	-147.1	-160.9
390	-164.9	-141.6	--167.6
430	-163.6	-137.5	-170.1
460	-168.7	-133.6	-172.0
490	-179.0	-126.2	-178.2
530	-173.1	-131.4	-179.2
560	-170.9	-133.4	-179.9
590	-171.1	-134.2	-179.0
630	-168.0	-134.9	-178.4
680	-183.6	-134.4	-171.5
740	-183.5	-135.1	-168.8
1000	-177.8	-112.0	-159.4
3000	-180.0	-100.0	-164.4
Direction of twisting	Counter-clockwise (CCW)	Clockwise (CW)	Counter-clockwise (CCW)

*the first value is obtained when refining with constraints to be comparable with literature, the second when refining with loose restraints as in all sub-ps and ps datasets presented here.

Changes in the protein

A sub-ps temporal evolution of positions of residues and waters involved in the proton release (on the μs/ms timescale) and residues lining the retinal binding pocket is observed in the data (Figure 13, Figure 14). The Wat402 displaces from its initial position by 0.3 Å and 0.6 Å at 0.24 ps and 0.39 ps, resp., increasing the PSB–Wat402 distance within 0.4 ps from 2.8 Å to 3.2 Å and one of the Wat402-Asp212 distance increases from 3.4 Å to 3.9 Å at 0.49 ps, likely breaking the hydrogen bond (Figure 14). The Asp85-Wat401 hydrogen bond increases from 2.7 Å to 2.9 Å at 0.49 ps. At the extracellular site, the distances of Wat403 to its hydrogen-bonding partners are increased – the distance to Arg82, Glu194 and Wat404 changes from 2.7 Å, 2.8 Å and 2.7 Å to 3.3 Å, 3.0 Å and 2.9 Å, resp.

The PSB–Wat402 distance oscillates in time with a frequency of ~80 cm^{-1} (Figure 13b), similar to the oscillation of the retinal skeletal torsions and the Lys216 χ_4 torsion angle (both ~90 cm^{-1},Figure 12d, e, Figure 13c). To accommodate the shifted Wat402, the carboxylate group of Asp85 reorients within 0.24 ps; the Asp212 χ_2 torsion angle as well as distances between the carboxylate oxygen atoms of Asp212 and Wat402 show an oscillatory behaviour (~80 cm^{-1}, Figure 13d, e, Supplementary Fig. 1a). These displacements likely cause the rearrangements of Wat401 and Wat406, propagating the motion to Arg82 (Supplementary Fig. 1b) and to Glu194 and Glu204: the distances between their carboxylate groups and Wat403/Wat404, which are part of the proton release group on the extracellular side[183], are modulated with frequencies of ~80-100 cm^{-1} (Figure 13f, Supplementary Fig. 1c-g). Oscillations in the positions of residues lining the retinal include Trp86 (χ_1 and χ_2 oscillation period ~150 cm^{-1} and ~125 cm^{-1}, respectively) and Tyr185 (χ_1 oscillation period about 80 cm^{-1}) as well as Met118 and Met145 lying within 4 Å of the retinal (Figure 13g-i and Supplementary Fig. 1h-j). Met118 χ_2 and χ_3 and Met145 χ_2 oscillate with ~100 cm^{-1}, ~100 cm^{-1} and ~90 cm^{-1}, respectively. A singular value decomposition on the maps using only a region within 5 Å around the retinal was performed, revealing oscillations with frequencies around 83 cm^{-1} and 113 cm^{-1}, further supporting the observed oscillations in the coordinates.

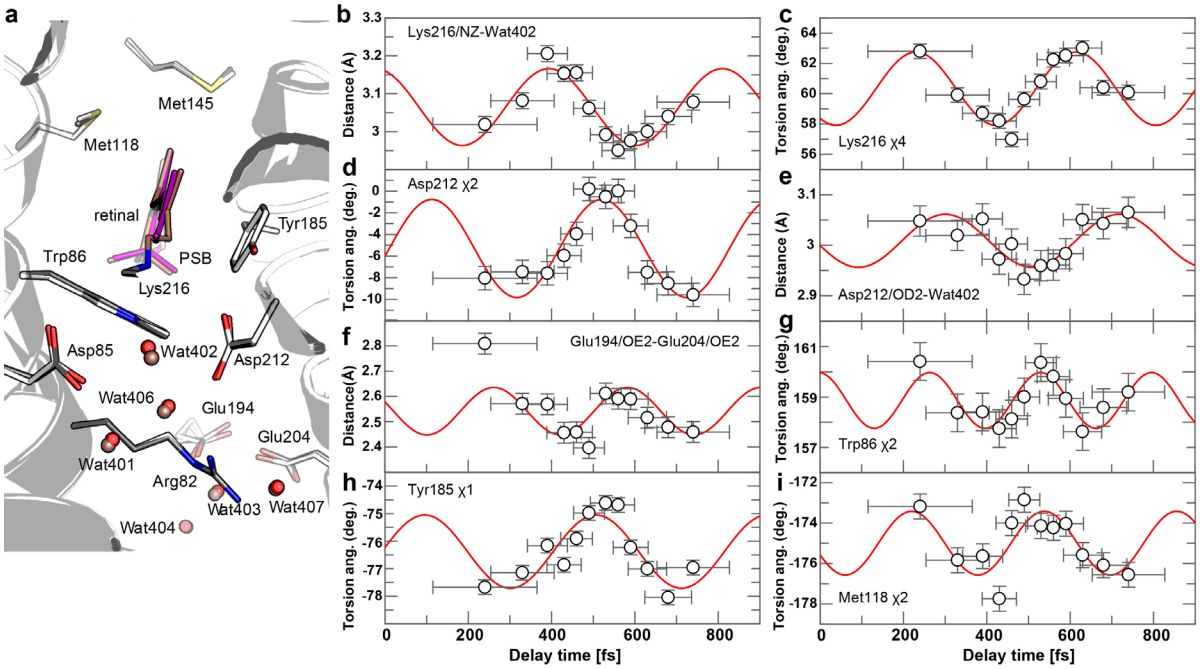

Figure 13. Motions of the water network and surrounding residues on the sub-ps timescale. a, View along the retinal chain towards the extracellular site. The dark-state and 0.49 ps structures of retinal (purple and dark-salmon sticks, resp.), of selected side chains (white and dark grey sticks, resp.) and of water molecules (red and dark-salmon spheres, resp.) are superimposed. In the all-*trans* dark state, the protonated Schiff base (PSB) forms a hydrogen bond (HB) with Wat402 (2.8 Å), which is wedged between counter ions Asp85 (2.5 Å) and Asp212 (3.0 Å). These are part of an extensive network of HB extending to the extracellular side (EC) of the membrane. Upon photoexcitation, displacements of waters (Wat402, Wat401, Wat406, Wat403, Wat407 and Wat404) and HB connected residues (Asp85, Asp212, Arg82, Glu194, Glu204) and nearby residues (Trp86, Tyr185, Met118) are observed. **b-f**, Within the hydrogen-bonding network, these displacements likely propagate from the PSB region towards the EC as coupled motions, as observed in the oscillatory modulations of torsion angles and distances. **b**, Upon photoexcitation of the retinal, the PSB-Wat402 distance initially increases within the first 0.4 ps to 3.2 Å, and then seems to oscillate with time with a frequency of 80±5 cm^{-1}. (**c**) Oscillation of the Lys216 χ_4 torsion angle with a frequency (87±6 cm^{-1}) similar to the retinal skeletal oscillations. **d**, **e**, Asp212 χ_2 angle and Asp212/OD2-Wat402 distance oscillation of 82±6 cm^{-1} and 80±9 cm^{-1} respectively. **f**, The distance of Glu194/OE2 and Glu204/OE2 undulates with a frequency of 104±17 cm^{-1}. **g-i**, Residues lining the retinal cavity also show oscillatory modulation of their torsion angles with following frequencies: Trp86 χ_2 (125±9 cm^{-1}, g), Tyr185 χ_1 (81±9 cm^{-1}, h), Met118 χ_2 (105±12 cm^{-1}, i).

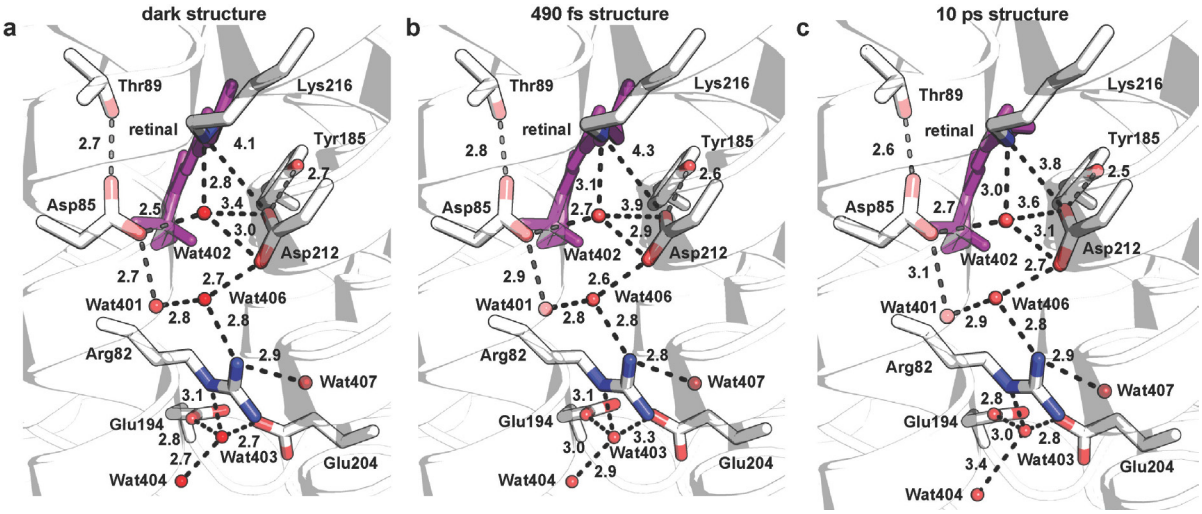

Figure 14. Evolution of distances between residues and waters along the proton pathway in time. Retinal is shown in pink and waters as red spheres. Distances are given in Å, those discussed in the text are shown in green. **a**, The dark structure. **b**, The 490 fs structure. **c**, The 10 ps structure.

Structural changes on the ps-timescale

The quality of the 3 ps and 10 ps data allows observation of light-induced structural changes directly in Fourier-transform difference maps in addition to extrapolated density maps (Figure 15). However, the data is too weak to determine the torsion angle solely from the electron density. Therefore, the initial coordinates were quantum mechanically optimized by Tatiana Domratcheva (our department) and geometric parameters from this QM-model (torsion angle -41˚) were used for subsequent refinement of the X-ray data, yielding a torsion angle of -68˚. Yet, the density can also very well accommodate the unrefined QM model. The torsion of the bond is accompanied by tilting of the methyl group C20 towards Tyr185 by almost 1 Å, which decreases the distance between C20 and the hydroxyl group of Tyr185 from 4.2 Å to 3.6 Å at 10 ps (Figure 15). Further motion is likely limited sterically.

Nonetheless, modifications of the hydrogen-bonding network spanning from the retinal to the extracellular site are apparent (Figure 14). As in the sub-ps data, the position of Wat402 is shifted at 10 ps, yet it partly moved back to be closer to the PSB (3.0 Å as compared to 3.2 Å at 0.39 ps). At 10 ps, it is also closer to Asp212 (the distance to the more distant Asp212 oxygen is 3.6 Å as compared to 3.9 Å at 0.49 ps), which forms a stronger bond with Tyr185 now (2.5 Å as compared to 2.7 Å in the dark structure). The Asp85-Wat401 distance keeps elongating, reaching 3.1 Å as compared to 2.7 Å in the dark structure.

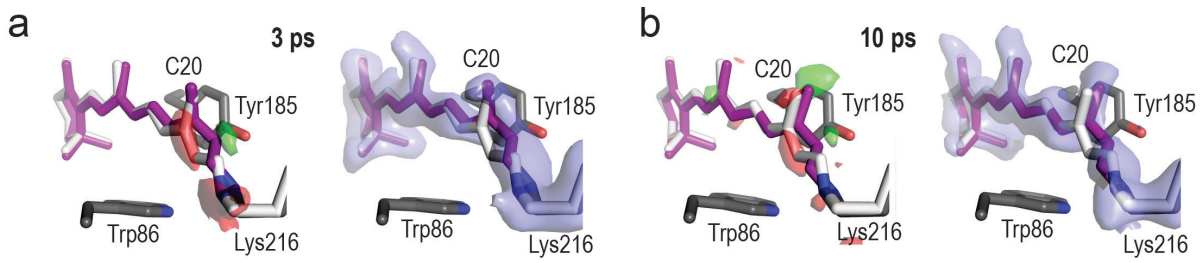

Figure 15. Structure of the retinal in bacteriorhodopsin on the ps timescale. a, View along retinal at time delays of 3 ps (**a**) and 10 ps (**b**); the retinal is shown in purple, and the dark-state structure as white sticks. Extrapolated electron difference maps (green, +3σ and red, -3σ) show clear deviations from the dark-state structure at the C20 methyl group as well as around the C13=C14 bond. Both the C20 methyl group and the C14 atom shift towards residue Tyr185 (shown as grey sticks). The 10 ps structure was refined using geometric parameters from a QM-optimized model resulting in a -68˚ torsion angle, corresponding to a twisted 13-cis conformation of retinal. Thomas Barends prepared this figure for the manuscript Nass Kovacs *et al.*

The 33 ms-structure

A later well-characterized intermediate of the photocycle was collected to test whether or not the high optical pump laser intensity used for photoexcitation allows the induced ultrashort reaction intermediates to proceed along the photocycle.

Due to technical reasons, a 33 ms time-delay structure was collected, which resembles the M-intermediate[4] (Figure 16), in line with the photocycle (Figure 1c). The rise of the M intermediate marks the deprotonation of the Schiff base and protonation of Asp85, perturbing the hydrogen bonding network in the extracellular half of the protein.[50] Arg82 rearranges and a proton is released from the extracellular release site, initiating larger structural changes that mark a transition to the late M intermediate on a sub-ms timescale.[38] The most prominent structural changes in the 33 ms-structure with respect to the ground state are the completely isomerized retinal moving the Lys216 side chain and a part of helix G, disorder of the water network (Wat402, Wat401, Wat406, Wat501), shifting of Trp182, Thr78 and Phe219 and, importantly, the flipping of Arg82 towards the extracellular site. The structural changes are in good agreement with an XFEL M-structure collected after a pump probe time-delay of 1.7 ms[87] (Figure 16c).

[4] Maximal occupancy in the crystal occurs at ~ 1 ms (Nango *et al.*, 2016).

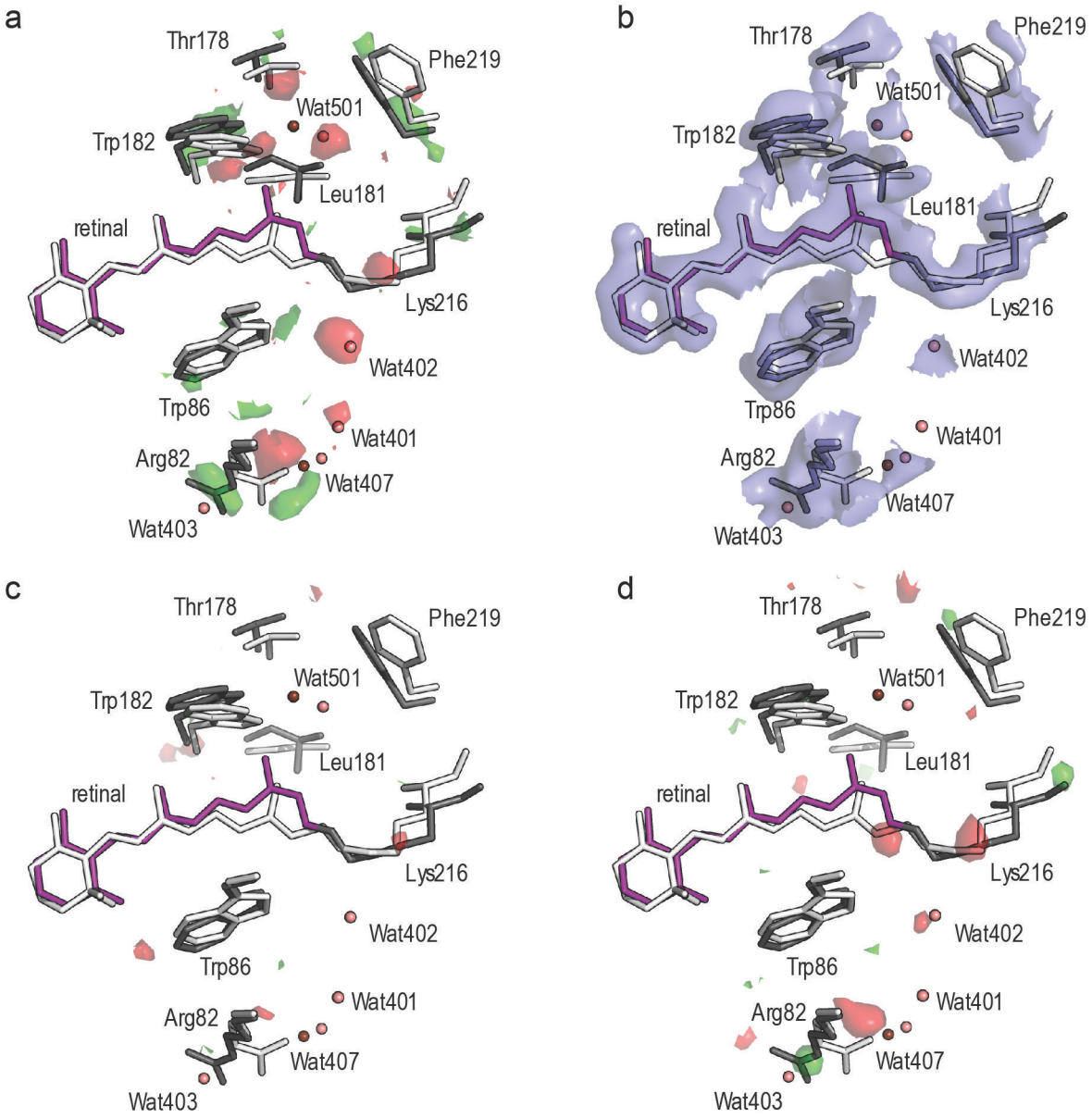

Figure 16. The M/ M-like structures. The ground state retinal and protein residues are shown as white sticks, whereas the 33 ms time-point state retinal and protein are shown as purple- and grey sticks, respectively. **a**, **b**, Close-up of the retinal and its surroundings in the 33 ms time point structure. In **a**, the q-weighted 33 ms - dark difference electron density map is shown, contoured at +3.0s (green) and -3.0s (red). In **b**, the 15% extrapolated electron density map is shown, contoured at 1.0 s (blue). **c**, F_o-F_o difference electron density map between our 33 ms structure and the 1.725 ms structure (5B6Z)[87] showing good agreement between the structures (no differences). **d**, $F_{extrapol}$-$F_{extrapol}$ difference density map between our 33 ms structure and the 8.3 ms structure (6G7L) reported recently[181], showing a larger contribution of light-induced changes in our structure. For **c** and **d**, water molecules from the dark state and pumped structures are shown as salmon and dark red spheres, respectively.

3.2.3. Transient ultrafast time-resolved spectroscopy

Ultrafast time-resolved spectroscopy on bR microcrystals was performed in order to establish whether the lifetimes of the intermediates and the isomerization time constant in the crystals are similar to those in PM. Additionally, to assess the impact of the pump laser intensity on the spectral signatures of both systems, a pump laser dependence or "power titration" was carried out.

Both time-resolved visible pump – visible probe (VIS) and visible pump – infrared probe (IR) spectroscopic measurements were performed. The preparation of the bR microcrystalline samples required developing a dedicated protocol given the following spectroscopic boundary conditions. The microcrystals scatter visible light strongly, contributing to a relatively high background level causing a poor signal to noise ratio in VIS measurements. While this is not such an issue for IR measurements, here the water content needs to be minimized to reduce water absorption in the region of interest as this also causes a high background level. In both cases, background decreases with the sample thickness, however in order to yield sufficient signal, this requires a higher crystal concentration than available from the crystallization set-ups. Therefore, the bR microcrystals were separated from the surrounding LCP matrix by centrifugation. This highly enriched bR microcrystal layer was then directly suitable for IR measurements. In case of VIS measurements, the enriched layer was adjusted with monoolein and F-127 until optically clear. Most IR experiments were performed in the region of 1480 cm^{-1} to 1570 cm^{-1} where photoproduct formation at about 1513 cm^{-1} and ground state bleach at 1527 cm^{-1} can be observed.[68] As H_2O has a local absorption maximum in this region,[184] it was exchanged for D_2O in these samples prior to the centrifugation step.

In the VIS measurements, the 400-700 nm region was probed, with the main features being ground state bleach (GSB) at 550-620 nm, excited state absorption (ESA) at 420-520 nm and photoproduct formation at 600-720 nm. Photoproduct formation was observed for the entire intensity range 35 – 130 GW/cm^2 (Figure 17). However, at higher excitation intensities, the isomerization time increases from ~0.5 ps to 0.7±0.1 ps and a spectral red-shift to ~670 nm in the photoproduct region is observed at 15 ps (Figure 18). At 50 ps, the maximum returns to ~650nm, representing the quasi-static 13-*cis*/all-*trans* difference spectrum (Figure 17d). The position of the ESA does not change, but at high pump power intensities, indications of an additional ESA in the 660-680 nm range (ESA2) were observed (Figure 17b-d). Further, a third ESA was observed at 460-480 nm (ESA3) from 2 ps on (Figure 17b-d). Both ESA2 and ESA3 have a 15-20 ps lifetime. All these features were observed with similar kinetics in microcrystals, however with a decreased signal-to-noise ratio (Figure 19). Under low excitation conditions, the isomerization time in crystals is ~0.6 ps.

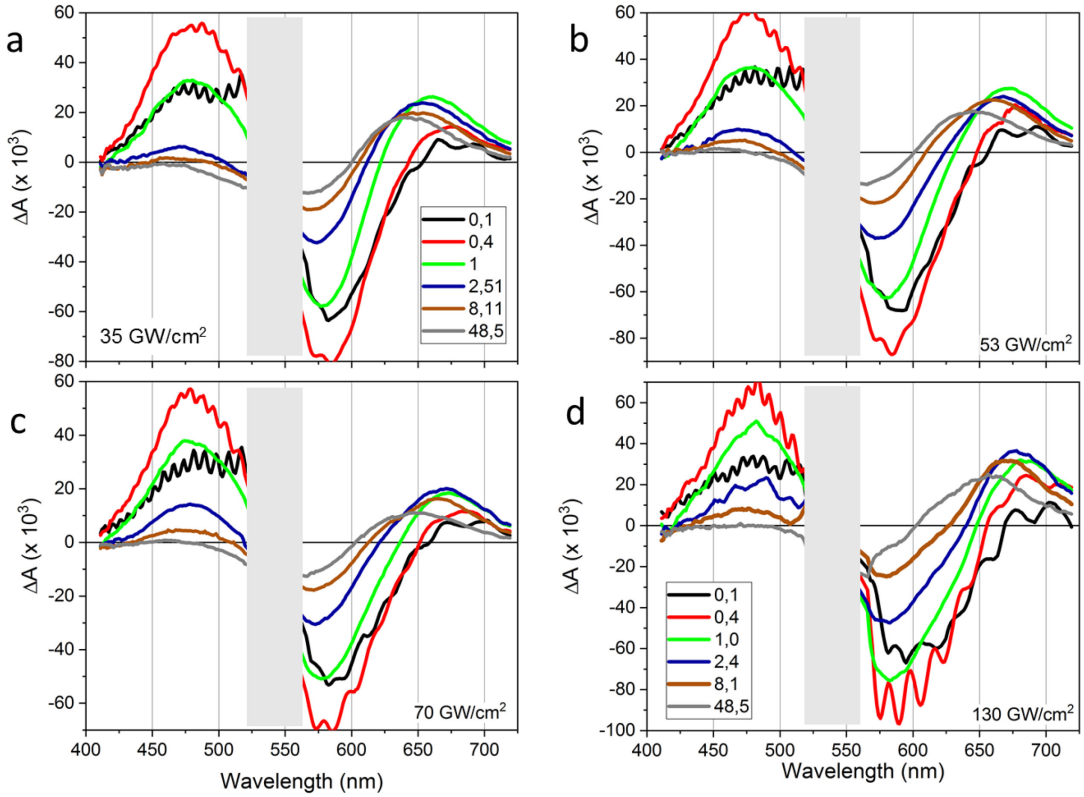

Figure 17. Comparison of spectral dynamics in the VIS domain upon excitation at 535 nm of bR in purple membranes with a peak intensity of (a) 35, (b) 53 , (c) 70 and (d) 130 GW/cm^2. Delay times in ps are as indicated in the legend. Excited state absorption - ESA region: 420-520 nm. Ground state bleach - GSB: 550-620 nm, Photoproduct – PP: 600 – 720 nm. Data in the region 520-565 nm are affected by pump beam scattering. With increasing peak intensity, the PP band after 1.0 ps keeps its maximum in the 660-680 nm range, before relaxing to ca. 635 nm at 50 ps. This indicates that the usual J→K transition, occurring within 3-5 ps at low intensities (panel **a**) is overlaid by an additional absorption in the 660-680 nm range (ESA2), the amplitude of which increases for higher intensities. It is assigned to ESA of the S_1 state of Trp86. Another ESA (ESA3), with similar temporal characteristics is observed as a weak signal centred at 470-480 nm for delay time ≥ 2 ps (panels **b-d**). Oscillatory features in the early delay time spectra are an artefact of the chirp correction procedure. This figure including the caption was prepared by Stefan Haacke for the manuscript Nass Kovacs *et al.*

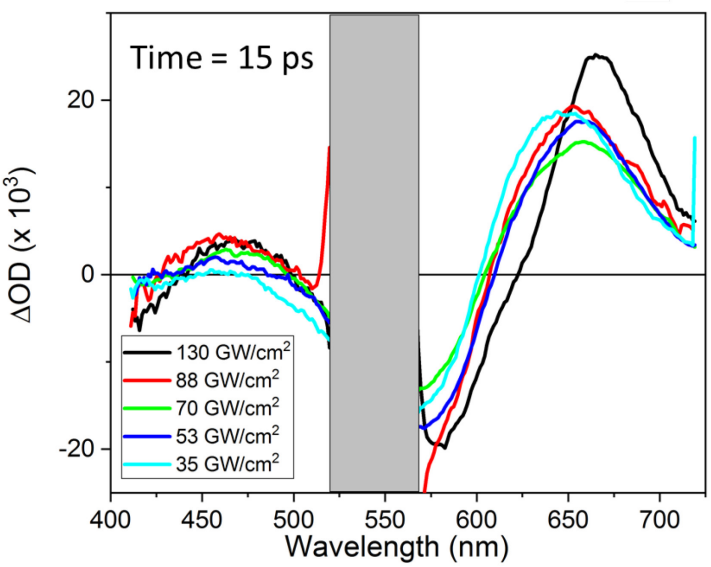

Figure 18. VIS Transient absorption spectra at 15 ps delay time in purple membranes. The 520-570 nm range (grey) is dominated by very strong pump light scatter. With increasing pump intensities the photo-product absorption band shifts to longer wavelengths (650-680 nm), and a long-lived weak absorption band appears peaking at 460 nm. This figure including caption was prepared by Stefan Haacke for the manuscript Nass Kovacs *et al.*

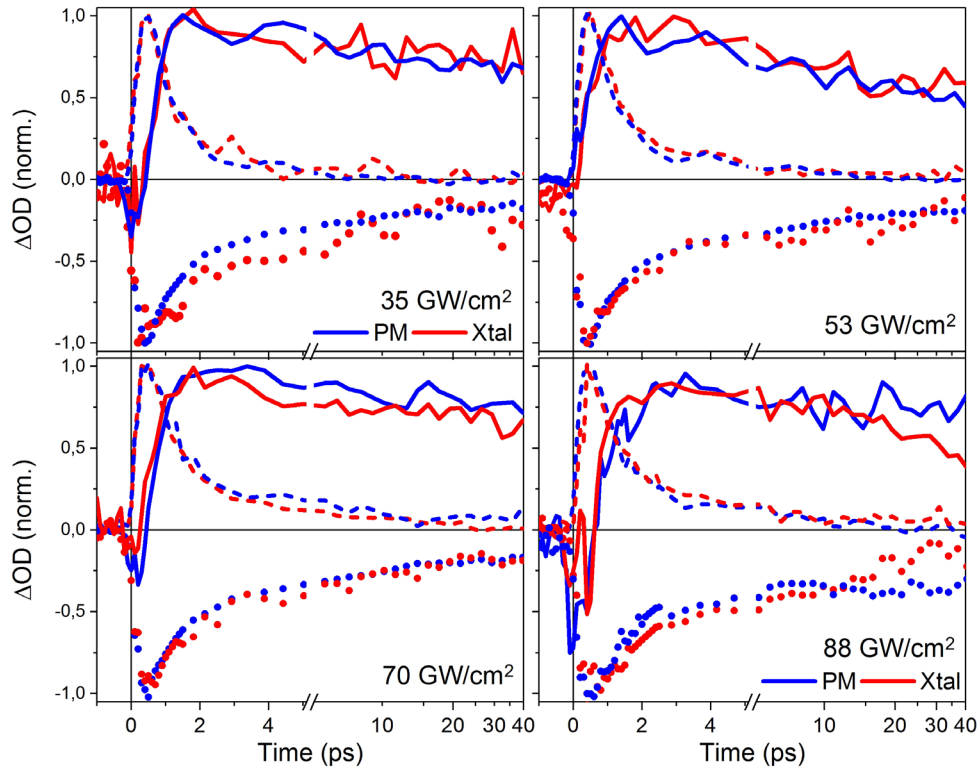

Figure 19. Comparison of the transient changes of the optical spectra of purple membranes (blue) and bR microcrystals (red). The power density of the optical pump was from 35 to 88 GW/cm^2. Within the present signal-to-noise ratio, the dynamics of 13-cis isomer formation (probe wavelength 670±5nm, solid lines, photoproduct), S_1-excited state decay (480±5 nm, dashed) and ground state recovery (570±5 nm, dots) are identical. The sub-picosecond decay of the S_1-state,

visible by the loss of stimulated emission and excited state absorption, is leading to the rise of the photoproduct. Additional relaxation dynamics occur on the picosecond timescale. For 35 GW/cm^2, global exponential fitting results in time-constants of 0.5±0.1 and 2.9±0.3 ps for bR in solution and 0.6±0.1 and 2.8±0.3 ps for the microcrystals. This figure including caption was prepared by Till Stensitzki and Stefan Haacke for the manuscript Nass Kovacs *et al.*

The power titration in the IR was performed in the range 12 – 180 GW/cm^2. The mid-IR range shows retinal C=C stretching vibrations of the excited state at ~ 1500 cm^{-1} and of the bleached ground state at 1527 cm^{-1}, photoproduct formation of J and K from 1510 cm^{-1} to 1520 cm^{-1}, and Trp bleaching signal at 1554 cm^{-1} (Figure 20a). Upon pump laser intensity increase, the photoproduct at 1513 cm^{-1} and the Trp bleaching increase linearly up to ~70 GW/cm^2, corresponding to less than 1 photon/retinal (Figure 20b). At the highest pump laser intensity of 180 GW/cm^2, the Trp signal is only twice as high as at 60 GW/cm^2. The photoproduct signal at 180 GW/cm^2 appears very low, below the value at 30 GW/cm^2. This is due to an overlap with another shoulder of the Trp bleach band. This prevents a reliable quantification of the photoproduct formed in dependence of the pump laser intensity. The Trp bleach does not rise immediately, but to a large extent with a time constant of 0.8 ps and it decays with a ~ 20 ps time-constant and no rise of the photoproduct can be observed upon this decay (Figure 20c). The Trp dynamics is slower in crystals as compared to the values above obtained from PM, but the same spectral dependence on laser power density can be observed.

At 180 GW/cm^2, the C=C stretching vibration of the excited state at 1500 cm^{-1} features an additional sub-ps decay (Figure 20c).

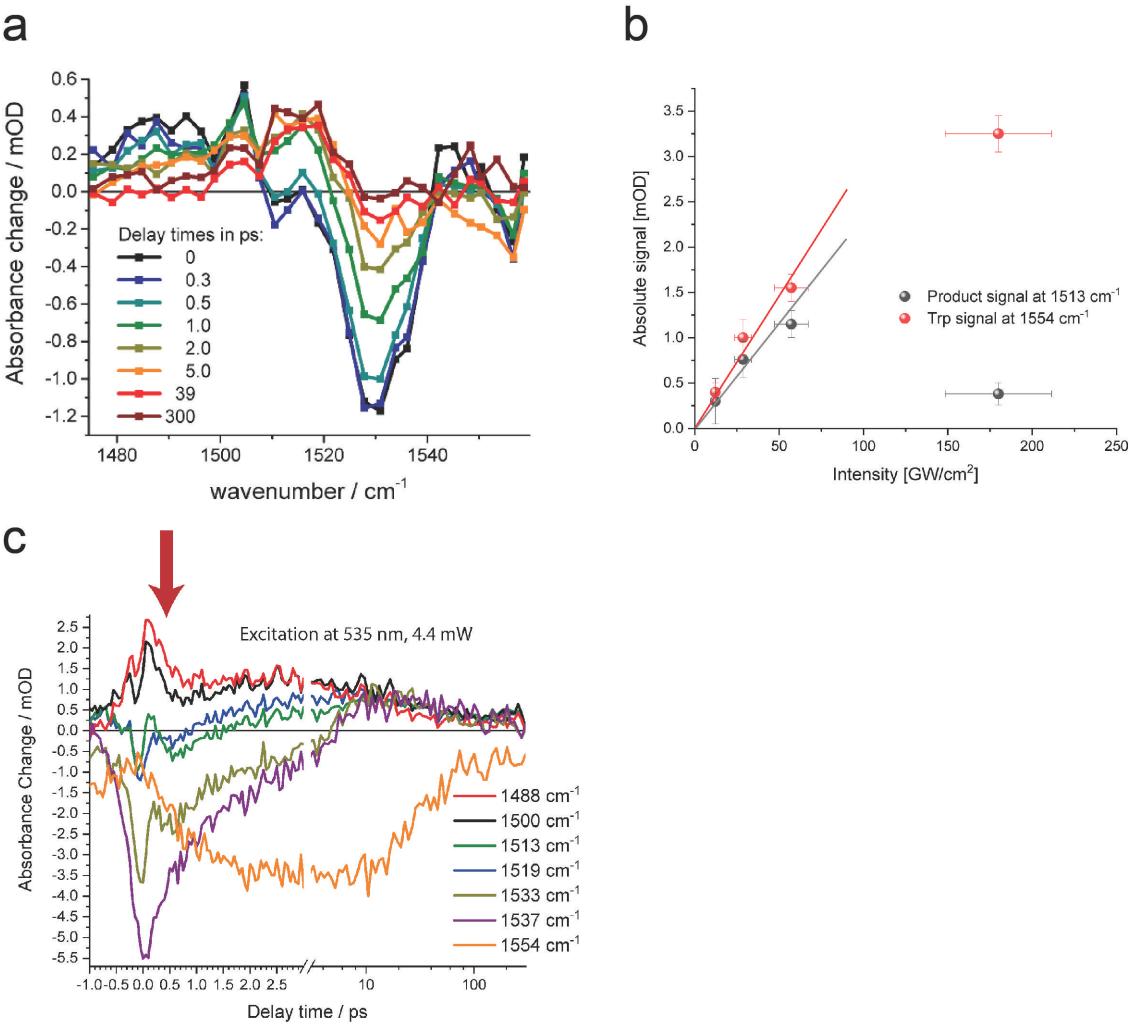

Figure 20. Mid-IR transient absorption spectra. a, Isomerization dynamics tracked in the spectral range of the retinal C=C stretching vibration for different delay times. Excitation was at 535 nm with 20 GW/cm^2 (equal to 0.5 µJ). The retinal bleaching signal at 1527 cm^{-1} and the excited state / hot product at around 1480 cm^{-1} are formed instantaneously. The rise of the J and K product signal is reflected by the signal increase around 1510 cm^{-1}. **b**, Maximal signal of the isomerization product (black circles) tracked at 1513 cm^{-1} as a function of excitation intensity at 535 nm. The maximal signal of the tryptophan bleaching band (red circles) is also presented. All four measurements were performed under the same experimental conditions without changing the laser set-up, keeping the non-systematic errors small. The samples were taken from the same batch with nearly identical concentration (~1 OD at 535 nm and 25 µm thickness). Deviation from linearity occurs at about 70 GW/cm^2. **c**, Transient signals at selected wavenumbers tracked in time. The red arrow marks the faster decay of the excited state C=C stretching vibration at 1500 cm^{-1}. This figure was prepared by Karsten Heyne and Yang Yang for the manuscript Nass Kovacs *et al.*

3.3. Production and characterization of ACR1

Expression and solubilisation of all eight ACR-GFP constructs was verified by in-gel fluorescence imaging of SDS-PAGE gels (Figure 21). All CGFP constructs (CGFP-ACR1, CGFP-ACR1-t, CGFP-ACR2 and CGFP-ACR2-t) could be expressed and solubilized in DDM while NGFP-ACR2 could be only expressed. Constructs NGFP-ACR1, NGFP-ACR1-t and NGFP-ACR2-t were expressed in too low amounts. The folding of the solubilized CGFP constructs was investigated by FSEC (Figure 22). A calibration curve $M_W = 10^{-0.2930V + 6.4457}$ (M_W is molecular mass in kDa, V is elution volume in mL, $R^2 = 0.9762$) based on protein standards was obtained from Miroslaw Tarnawski. In samples CGFP-ACR1-t and CGFP-ACR2-t, highest levels of fusion protein expression were detected, with peaks eluting at 14.4 and 14.5 ml corresponding to ~ 160 kDa and no significant free GFP peak was present. CGFP-ACR2 contained the fusion protein (13.9 ml, ~ 240 kDa) and roughly equal amounts of free GFP (17.0 ml, 29 kDa), whereas CGFP-ACR1 contained free GFP and no fusion protein (16.9 ml, 32 kDa).

Based on higher expression levels, constructs CGFP-ACR1-t and CFGP-ACR2-t were selected for recombinant baculovirus generation to enable large scale expression. Analysis of the expression of both constructs from the p_0 recombinant baculovirus generation showed that CGFP-ACR1-t has higher expression levels (Figure 23). Simultaneous detergent screening with DDM, DM, OG and Cymal-5 showed that only OG could not solubilize the proteins. Given that the overall expression level was low (protein could not be clearly observed in the lysate using Coomassie staining only), only the construct CGFP-ACR1-t was selected for large scale expression and purification, using the detergent DDM for its mild solubilisation properties and compatibility with the downstream purification procedures.

Upon solubilisation, the protein was purified by immobilized metal affinity chromatography (IMAC), the GFP and 10 × His-tag were cleaved off by a TEV protease and removed by reverse IMAC and gel filtration was the final purification step (Figure 24). The yield was typically around 1 mg ACR1-t/ 10 L of insect cell culture, which is considerate reasonable for membrane protein expression in insect cells.

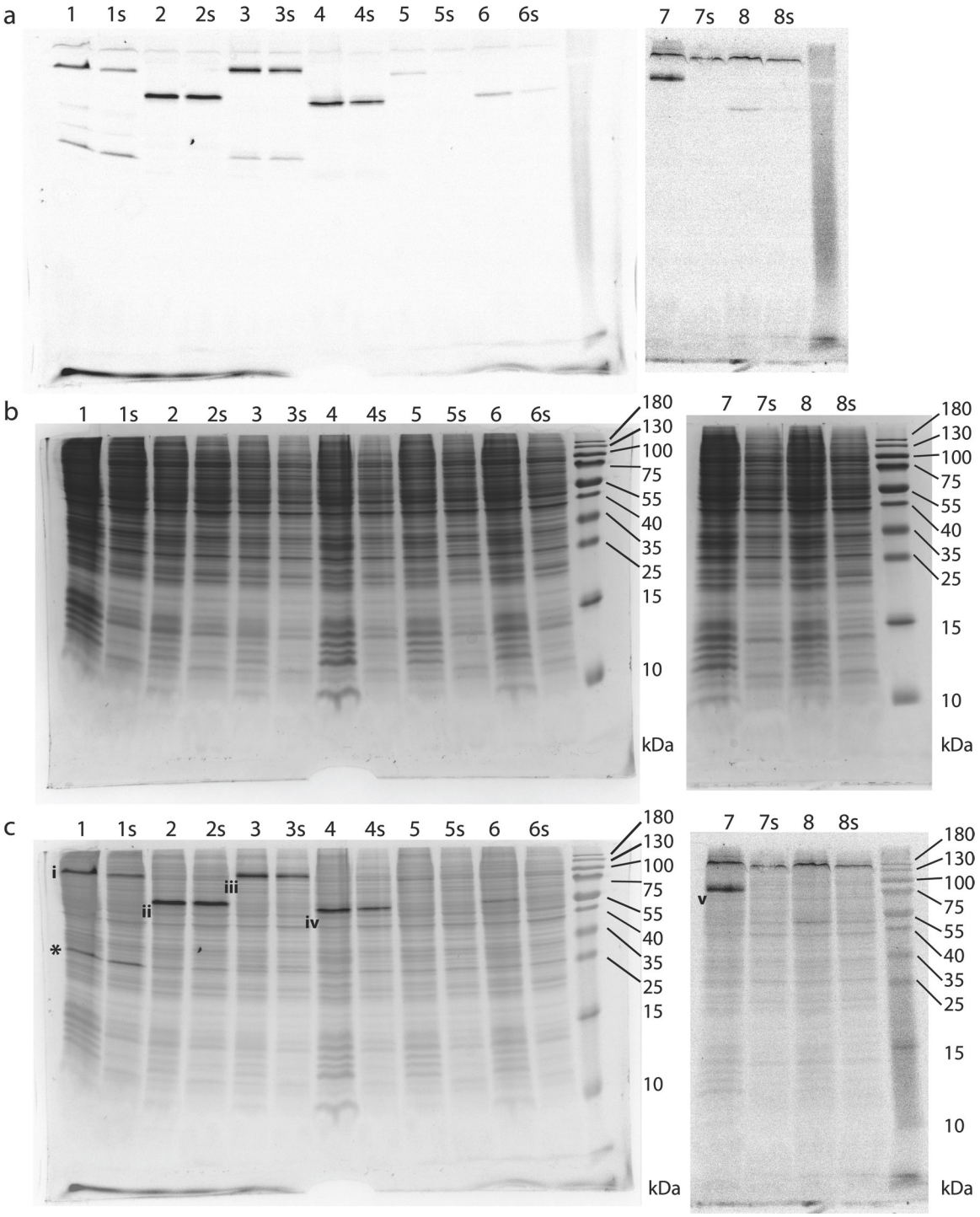

Figure 21. SDS-PAGE analysis of transient expression of all eight ACR-GFP constructs in Sf21 cells. Sample legend: 1 – CGFP-ACR1, 2 – CGFP-ACR1-t, 3 – CGFP-ACR2, 4 – CGFP-ACR2-t, 5 – NGFP-ACR1, 6 – NGFP-ACR1-t, 7 – NGFP-ACR2, 8 – NGFP-ACR2-t. Only numbers denote the total fraction and lanes with "s" in addition denote the soluble fraction. **a**, Fluorescence imaging of the gels. **b**, Coomassie-stained gels. **c**, Digital overlay of **a** and **b** showing that detected bands roughly match the molecular mass of anticipated proteins: * GFP 29.5 kDa, i – CGFP-ACR1 79.3 kDa, ii - CGFP-ACR1-t 62.7 kDa, iii - CGFP-ACR2 78.6 kDa, iv - CGFP-ACR2-t 62.0 kDa, v - NGFP-ACR2 78.7 kDa.

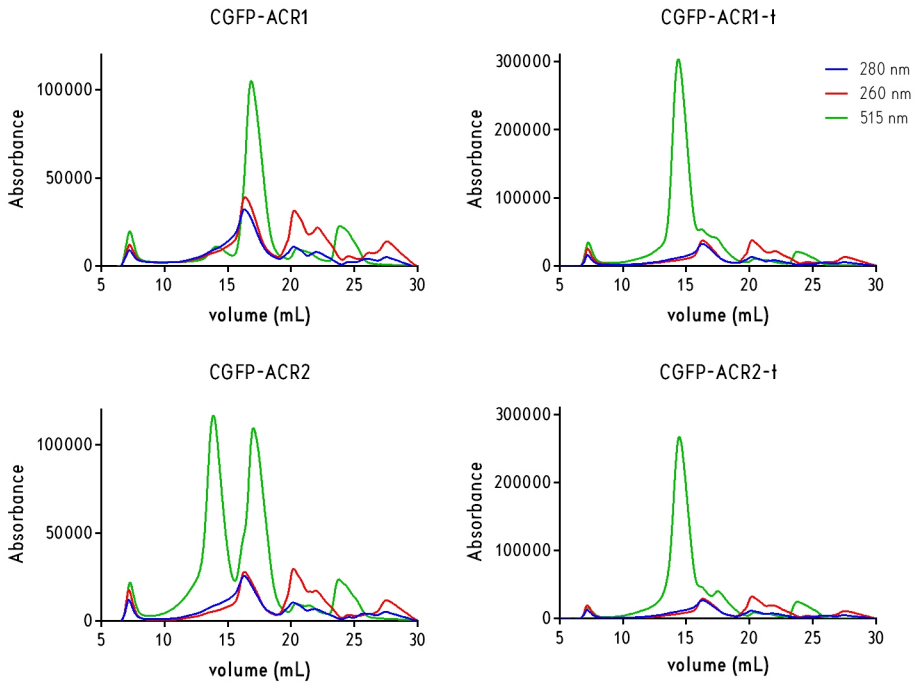

Figure 22. Chromatograms from fluorescence-detection size-exclusion chromatography of all CGFP-ACR constructs.

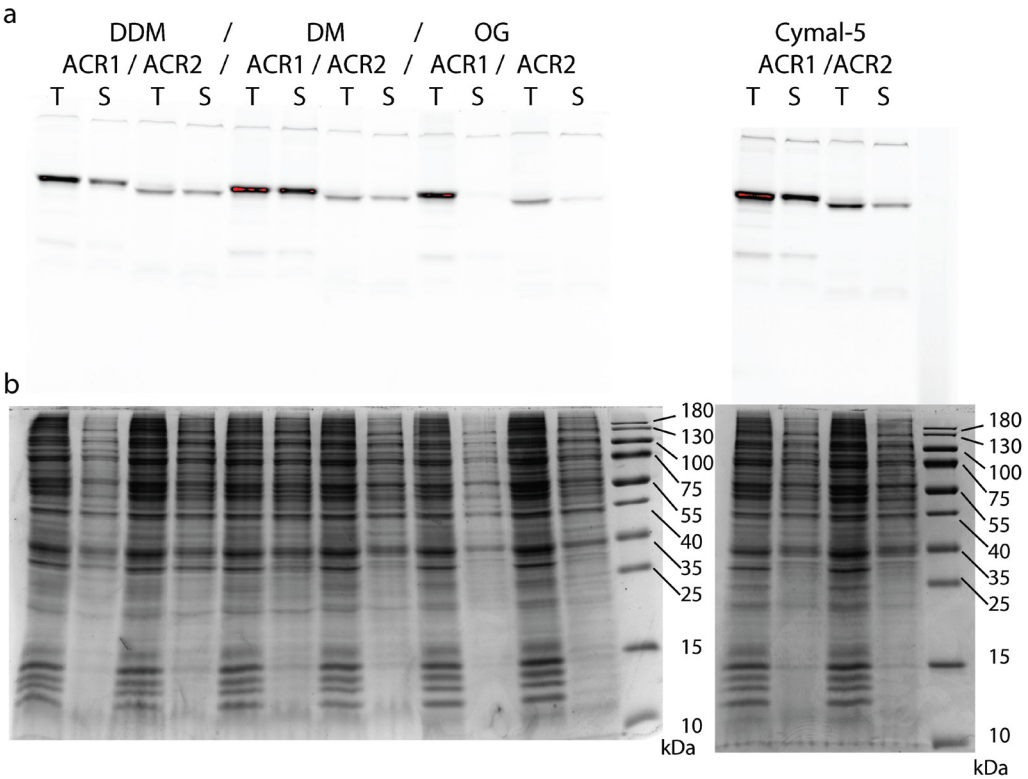

Figure 23. SDS-PAGE analysis of recombinant baculovirus expression of CGFP-ACR1-t and CGFP-ACR2-t. Total (T) and soluble (S) fractions of each construct solubilized in DDM, DM, OG and Cymal-5 were loaded. **a**, In-gel fluorescence imaging. **b**, Coomassie-stained gels.

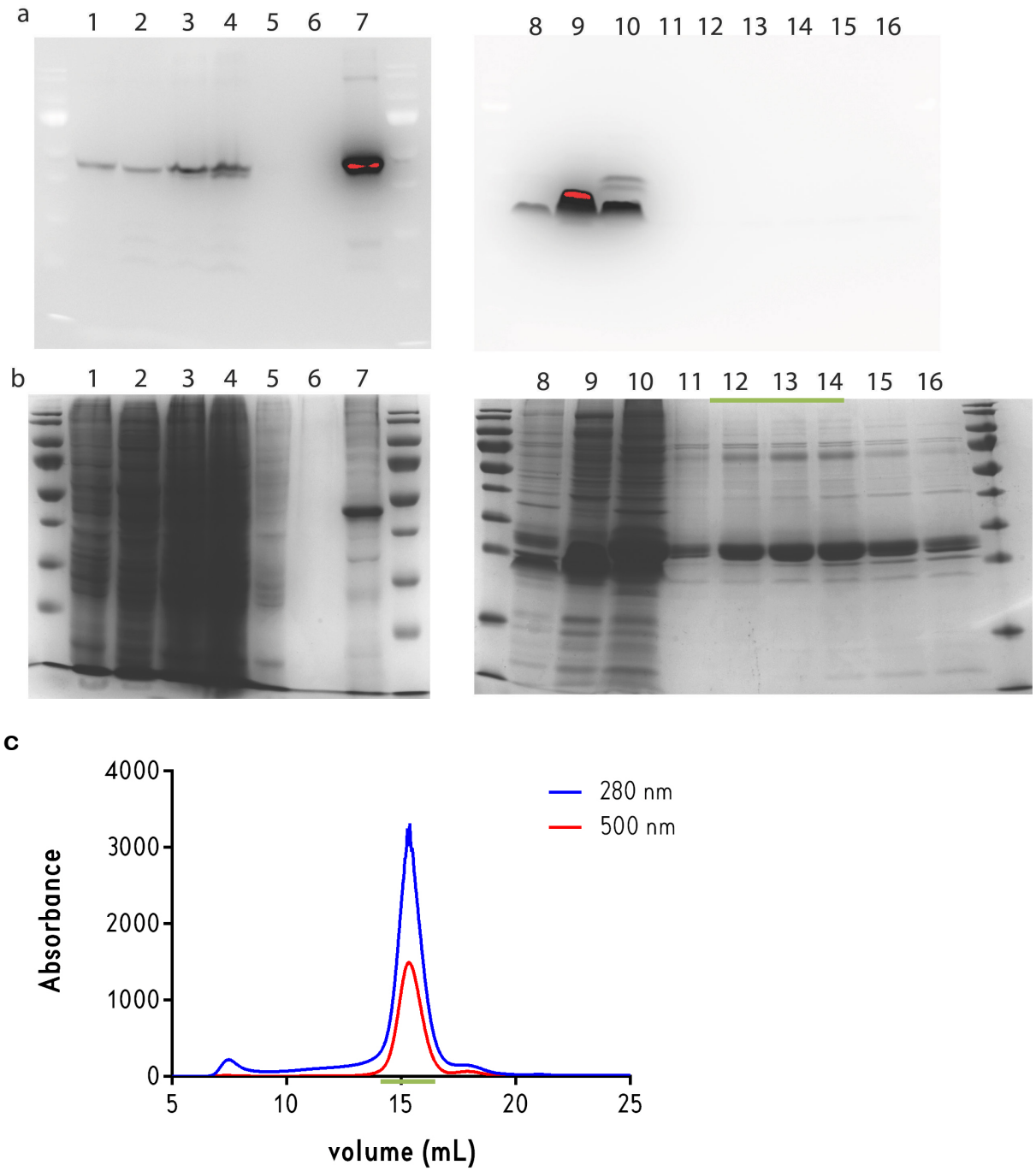

Figure 24. Purification of CGFP-ACR1-t. a,b, SDS-PAGE analysis of the purification steps - **a**, In-gel fluorescence imaging. **b**, Coomassie-stained gels. 1 – membranes, 2 – intracellular fraction, 3 – solubilized membranes, 4 – supernatant loaded onto an IMAC column, 5 – first column wash (30 mM imidazole), 6 – last column wash (30 mM imidazole), 7 – column eluate, 8 – TEV cleavage mixture, 9 – GFP and TEV eluted from the second IMAC, 10 – flow-through of the second IMAC loaded onto a SEC column, 11-16 consecutive fractions from the SEC, pooled fractions are marked with a green line. **c**, Chromatogram of the size exclusion chromatography. The green line marks the pooled fractions.

Retinal extraction and separation

Retinal extraction from purified ACR1-t was performed to measure the relative content of all-*trans* and 13-*cis* retinal in light-adapted and dark-adapted protein (Figure 25). Areas under the curve used for the relative content calculation are listed in Table 17. Room-light adapted protein yielded 36 % 13-cis and 64 % all-trans retinal (Figure 25a), essentially identical with the composition of an overnight dark-adapted sample (39 % 13-*cis* and 65 % all-*trans* retinal, Figure 25b). 15 s of white-light illumination increased the 13-cis content to 43 % and this remained unchanged even after overnight incubation in the dark (Figure 25c, d). These results indicate that ACR1-t does not undergo any light-/dark-adaptation and contains about 1/3 13-*cis* and 2/3 all-*trans* retinal, similarly to the dark-adapted state of bR. The irreversible change upon illumination was likely due to light-induced damage on the retinal, since detergent likely destabilizes the protein. This result is in line with published resonant Raman study concluding that ACR1 does not undergo light-adaptation, but it is at odds with their report of 100% all-*trans* retinal in the protein.[185] This is based on the similarity of the ACR1 light- and dark-adapted difference spectrum with those of bR and *Chlamydomonas augustae* CCR1, which both contain 100% all-*trans* retinal.[185] Given that the spectral band used for this comparison is similar, but not identical, and the large discrepancy with the extraction results presented here, further work is needed to clarify this point.

Table 17. Relative quantification of 13-cis and all-trans isomers in the samples

Sample name	Retinal isomer	Retention time (min)	Area	Relative amount
room-light adapted ACR1	13-*cis*	3.060	101352	35 %
	all-trans	3.536	232391	65 %
dark-adapted ACR1	13-*cis*	3.200	51582.9	39 %
	all-trans	3.702	101144.6	61 %
15 s illuminated ACR1	13-*cis*	3.099	48402.0	43%
	all-trans	3.629	80594.7	57%
control ON dark-adapted ACR1	13-*cis*	3.119	50220.7	42 %
	all-trans	3.626	86917.0	58 %

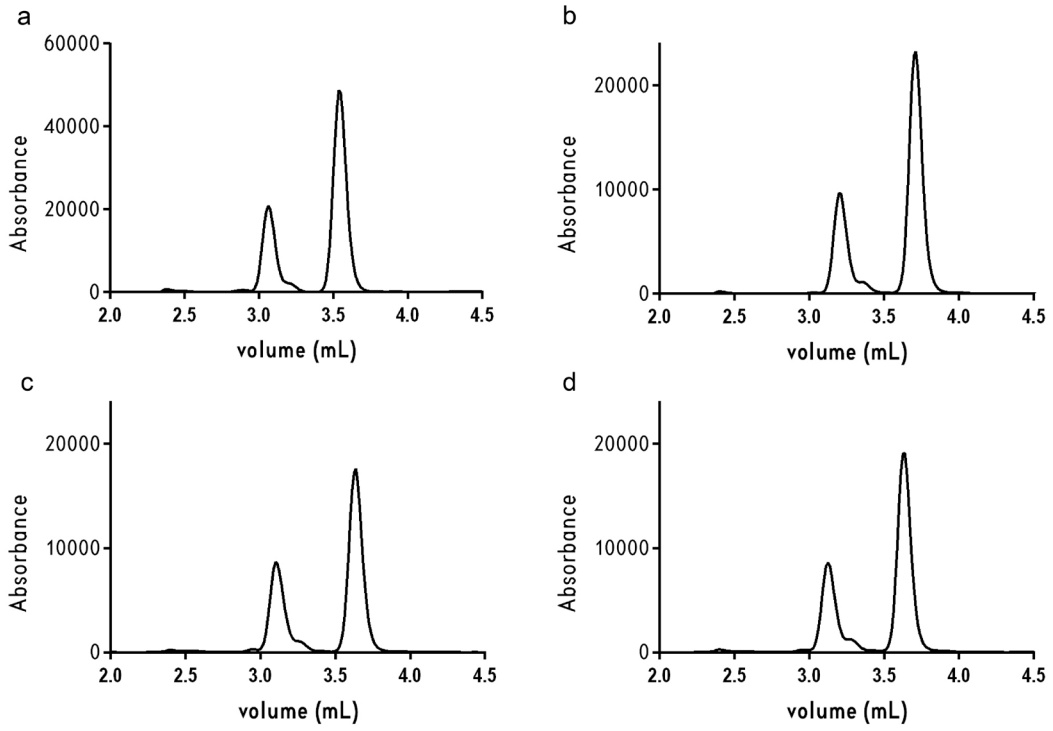

Figure 25. Chromatogram of the retinal HPLC separation. Absorbance was monitored at 360 nm. **a**, room-light adapted sample. **b**, dark-adapted sample. **c**, light-adapted sample. **d**, sample c measured after an overnight dark-adaptation.

Blue native (BN) PAGE analysis

BN PAGE is a suitable method to analyse the oligomeric state of membrane proteins under native conditions[144]. The detergent concentration was varied to access the effect on the protein dispersity. In all three samples (DDM at 3 × CMC, 1.5 × CMC, no DDM), the protein migrated as a single band with a molecular weight of ~ 150 kDa (Figure 26). This is in line with the size estimation from FSEC (~ 160 kDa) and indicates that the protein likely forms at least a dimer surrounded by many detergent molecules (ACR1-t dimer is 66.6 kDa, DDM micelle size is 72 kDa). As a 10 × dilution of detergent made no difference in the oligomeric state, this also suggests that the initial protein stock solution contained a large excess of detergent. Consequently, the purified protein was washed with buffer without detergent to decrease the detergent concentration and thereby facilitate crystallization in LCP.

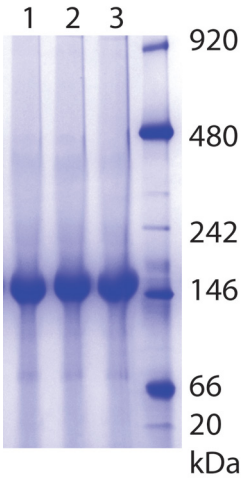

Figure 26. Blue native PAGE analysis of purified ACR1-t with different DDM concentrations.

1 – 0.025 % DDM (3 × CMC)

2 – 0.0125 % DDM (1.5 × CMC)

3 – no DDM

In-meso crystallization of ACR1-t

Initial sparse matrix screening with ACR1-t reconstituted in LCP yielded no crystals. The protein was therefore 20 x diluted with buffer without detergent and concentrated again to the initial value. This step reduced the excess of detergent in the sample. The "washed" protein was again used for crystallization screening and yielded small needle-shaped crystals grown in 1.8 M Na/K phosphate pH 7.6 (Figure 27) and very small stick-shaped crystals in 0.2 M $MgCl_2$, 0.1 M HEPES pH 7.5, 15 % isopropanol (too small for photographs). The first condition could not be reproduced, while the second would repeatedly yield very small pink needles (~10-20 um). These can now be used for time-resolved SFX measurements if granted XFEL beamtime. Meanwhile, optimization of crystallization conditions to yield larger crystals would allow determining the structure of the first protein from this new family of anion channelrhodopsin using synchrotron radiation. Crystal optimization is under way.

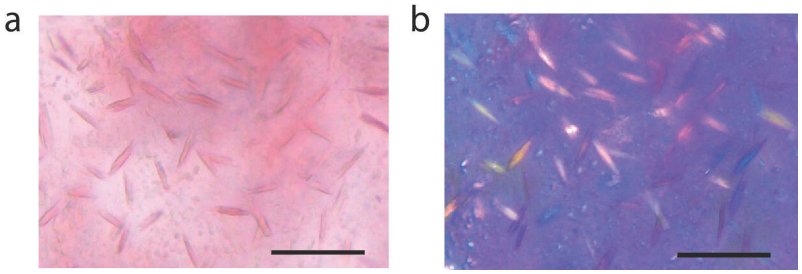

Figure 27. ACR1-t crystals obtained in 1.8 M Na/K phosphate pH 7.6. Black scale bar is 100 µm. **a**, White light exposure. **b**, Exposure with cross-polarizers.

4. Discussion

Ultrafast light-induced events in bacteriorhodopsin

The ultrafast events in single-photon photoexcited bR are known to involve an immediate change in dipole moment in the retinal modifying bond length alternation in the retinal and the protein-retinal interactions. Then, high-frequency stretching and lower-frequency torsional vibrational modes in the retinal are activated. These events precede the isomerization reaction and likely drive it. The importance of contributions of the protein is evidenced by the increased isomerization quantum yield and bond specificity of retinal bound to the opsin in contrast to free retinal in solution. The detailed mechanism of the interplay between the retinal photochemistry and the protein contribution, however, remains unclear. The current knowledge about these ultrafast events has been mainly gained from ultrafast spectroscopies, which can achieve fs time resolution, and from QM calculations. Valuable insight based on structures of ultrafast intermediates has been missing due to the technical limitation of at most ~100 ps time-resolution in time-resolved macromolecular X-ray crystallography using synchrotron sources. This has now changed with the development of SFX using XFEL radiation. SFX enables time-resolved experiments with sub-ps time resolution allowing the determination of ultrafast intermediate structures at physiologically relevant room temperature. The short pulse duration also allows outrunning effects of radiation damage, which is important in case of radiation-sensitive rhodopsins. Due to the high peak brilliance, small crystals can be used for data collection, which are more readily penetrated by the optical pump laser, increasing the occupancy of the photoexcitated intermediate in the crystallographic data.

A major issue is the power density of the optical pump laser used in the TR-SFX experiment on bR described here. Although it is well within the range used for other ultrafast TR-SFX experiments, it is significantly above the spectroscopically established limits of a linear excitation regime. Since a TR-SFX power titration could not be carried out during the experiment to identify optimal excitation conditions, a spectroscopic power titration was performed instead. It confirmed the similarity of multiphoton effects in crystals and PM and provided further insight into the nature of these effects. It remains an open question to what extent conditions established in spectroscopic experiments can be translated to SFX experiments. However, given the high excitation intensity used in this work and thus a high probability for multiphoton effects occurring, the mechanistic implications of the crystallographic observations are not straight forward.

Despite this handicap, the crystal structures are discussed with following functional questions in mind in order to identify similarities and differences compared to previous work and relate new findings.

- How do structural changes evolve in the retinal and how does the isomerization proceed in the confined binding pocket?
- How do the conformations of residues, especially those that are essential for early and late functional steps, evolve in time?
- How is the hydrogen-bonding network affected on the sub-ps and ps timescale?

4.1. Multiphoton excitation

Ultrafast optical-pump – X-ray-probe TR-SFX were so far performed at excitation intensities of 360 – 570 GW/cm^2,[102,103,181,186] which is significantly higher than what is typically used in solution spectroscopy. This is partly due to conceptual differences between these two types of experiments. In transient absorption spectroscopy, spectroscopic signatures are often highly specific for a certain molecular species, allowing its detection even at low concentrations. This is different in the crystallographic experiment, which yields an electron density representing the molecular ensemble of all molecules in the crystal. To maximize the signal from photoexcited molecules, one would ideally provide one photon for each chromophore molecule. Given that the protein concentration in crystals is extremely high (730 mg/mL for bR) and the crystal size may be beyond the penetration depth 1/e, the temptation is to go to higher excitation intensities in pump-probe SFX experiments. Additionally, extensive losses (~80%) due to laser light scattering both from the liquid jet[187] or viscous stream[181] were reported, which has been used to justify the need for a very high excitation intensity. This is however problematic, since multiphoton excitation can severely affect the biological process investigated. For bR, at excitation intensities above 100 GW/cm^2, additional spectral changes were observed, such as a red-shift of transient spectra of K_E.[188,189] Fluorescence measurements under high-excitation intensities reported an increase in the decay time constant of the excited state from 0.45 ps to 0.7 ps.[190]

This TR-SFX experiment was partly knowingly and partly by accident also performed under very high excitation conditions (500 GW/cm^2), resulting in multiphoton excitation. Given the paucity of XFEL beamtime, it was neither possible to first establish the dependence of the structural changes in the X-ray data on the pump power density and perform the experiment with the knowledge of the optimal excitation intensity, nor to repeat the TR-SFX measurement at an optimal excitation intensity. In order to gain more insight into the events occurring at high excitation intensities, a spectroscopic power titration was performed. Due to technical reasons, the highest excitation intensity achieved in the spectroscopic power titration was 180 GW/cm^2, which is about one third of what the TR-SFX experiment used.

The power titration in the VIS and IR confirmed the previously reported red-shifted spectra and a delay in the isomerization time in the high intensity excitation regime (Figure 17, Figure 18). Additionally, several previously undescribed features occurring predominantly at the highest excitation intensity used (130 GW/cm^2 and 180 GW/cm^2 in the VIS and IR measurements, resp.) were observed. In the VIS region, two new excited state emission bands were identified (ESA2 and ESA3) and their spectral positions are consistent with the excited state absorption bands of Trp in H_2O.[191] Further, the lifetimes of ESA2 and ESA3 are 15-20 ps, in line with the 10±5 ps lifetime of tryptophan fluorescence emission under sequential

two photon excitation.[192] Moreover, this assignment is also in agreement with the Trp ground state bleach observed in the IR, which decays on a time-scale of ~20 ps (Figure 19). The decay of this bleach, thus the recovery of the Trp ground state, does not appear to yield photoproduct (Figure 19), which would imply that it does not affect the isomerization. The rise of this bleach signal continues after the termination of the pump pulse (Figure 20c). In line with the results of QM calculations, this process is likely a sequential two photon absorption creating an excited state Trp, specifically Trp86. The QM calculations show a strong electronic coupling between the retinal S_1 state and the Trp86 charge-transfer (CT) state, which can be populated when the Trp86 HOMO donates an electron to the retinal LUMO, as opposed to an intra-retinal charge transfer. The absorption of a second photon by either the retinal S_1 state or the Trp86 CT state leads to the population of the excited Trp86 state. This state is more strongly coupled to the CT state than to excited states of the retinal, thus energy transfer back to retinal - and induction of photoproduct formation - is unlikely.

Another new spectral feature is the sub-ps decay of the retinal excited state C=C stretching vibration on time-scale faster than 500 fs at 180 GW/cm^2 (Figure 19). This indicates additional interactions of the excited state, such as its depletion by stimulated emission.

Nevertheless, even at 180 GW/cm^2, the VIS and IR data show the characteristic sub-ps isomerization time and the quasi-static K-bR difference spectra, attesting for isomerization in the multiphoton regime. This is in line with a previous report of a VIS experiment observing isomerization even at the maximal pump laser intensity of 200 GW/cm^2, albeit yielding less photoproduct than at low excitation intensities.[188] This was interpreted such that the additional multiphoton channels do not significantly contribute to photoproduct formation.[188]

This spectroscopic data in combination with the QM calculations provide more insight into the nature of multiphoton effects by identifying a new decay channel via a Trp86 excited state which is unlikely to contribute photoproduct. It also hints at the presence of additional retinal excited state processes, which may or may not contribute photoproduct. It can only be speculated how this translates into the TR-SFX experiment using 500 GW/cm^2, since additional processes will occur at 500 GW/cm^2, a power density that could not be reached in the spectroscopic power titration.

4.2. Ultrafast events preceding/ accompanying isomerization

The immediate charge translocation upon single photon absorption decreases the bond length alternation.[61] This property of retinal is quantitatively similar when it is free as a PSB in solution[60] or bound to the opsin.[57,58] The anticipated changes in the bond lengths (double and single bonds becoming longer and shorter, resp.) are around 0.1 Å.[71] These differences cannot be resolved at the available spatial resolution in the sub-ps SFX data, however the distorted planarity of the retinal already within the first time-point of 0.24 ps (Figure 12a, b) could be due to the altered bond order in the system. Thereafter, depopulation of the Franck Condon region launches intense stretching activity along the C=C and C-C bonds as the excited state I is formed (200-500 fs).[56,63,64] The observed twisting along the retinal aliphatic chain until ~ 0.5 ps may be thus a manifestation of this stretching activity. Notably, the displacement of the C14 atom from the retinal plane is evolving with the rise of I (τ=245 fs) (Figure 12c). The excited state I is analogous in native bR and in bR reconstituted with non-isomerizing retinal analogues that have the C13=C14 bond locked – thus these motions precede isomerization.[193]

Low-frequency modulations of spectroscopic signals from retinal have been observed in numerous experiments and computationally rationalized. Excited-state vibrational coherences with a frequency of ~120 cm^{-1} were detected in stimulated emission signals from impulsively excited retinal PSB, and are the same in 13-*cis*- and 13-*trans*-locked retinal PSB analogues.[66] However, when analogously probing bR in spectral regions of stimulated emission[66,194] and excited-state absorption[195], the main frequencies are ~160 and ~210 cm^{-1}. Interestingly, these frequencies also vary among microbial rhodopsins, which altogether highlights the specific role of the protein binding pocket in this process.[67] The periodic modulations are damped on a timescale of ~250 fs and were assigned to excited-state large skeletal torsions in the retinal molecule,[195,196] which are predicted to be part of the reactive coordinate driving the excited state population through the conical intersection to the ground state, thereby implicating isomerization.[72]

It this work, low frequency oscillations of the retinal aliphatic chain with respect to the β-ionone ring (~120 cm^{-1}) and of the entire retinal as defined by the terminal methyl groups motions (~90 cm^{-1}) were observed on the sub-ps timescale (Figure 12d, e). Given the fitting error of ±10-15 cm^{-1} and the error introduced by the in some cases very large (but necessary) temporal binning of the diffraction images, the published frequencies derived from spectroscopic data can be considered in qualitatively good agreement with these observations of low-frequency modulations in nuclear positions of retinal atoms in the crystal structures.

Nonetheless, the spectroscopic data was collected in a single-photon regime as opposed to the multiphoton excitation in the SFX experiment, therefore it remains open whether both types of experimental data describe the same process, despite a similar manifestation.

Likewise, oscillations were seen in torsion angle values of protein residues and in their distances to other residues or to hydrogen-bonded water molecules (~80-150 cm^{-1}, error ±10-20 cm^{-1}, Figure 13 and Supplementary Figure 1). Oscillations in the protein were not described in bR literature, possibly because they may not be detectable in optical experiments. These oscillations are also similar in frequencies to the values published for oscillations in optical traces from retinal in bR. Ultrafast protein motion preceding the isomerization has been observed before, but could not be further assigned.[7678,79] In this work, however, the crystal structures allow to specifically see which protein residues are in motion, and moreover, an oscillatory component can be extracted. Despite multiphoton excitation intensities, they occur predominantly in residues that are functionally relevant for the ultrafast events (e.g. Asp85, Asp212, Arg82, Trp86)[197,198] and for proton pumping (additionally Glu194, Glu204, Ser193)[54]. All these residues are connected with the PSB via an ordered network of waters. Further, oscillations in torsion angles of residues interacting sterically with retinal are also observed (Met118, Met145, Tyr185).

4.3. Isomerization mechanism

Various mechanisms were proposed for photoisomerization of polyenes around a double bond, covering both small organic molecules and protein-bound polyenes. Polyenes freely moving in solution isomerize via the simple one-bond-flip mechanisms, which is illustrated in Figure 1a.[199] For protein-bound molecules, a volume-conserving mechanism is typically required, such as the hula-twist or bicycle-pedal mechanisms, which were both suggested for visual rhodopsin (Figure 28). In the hula-twist mechanism, isomerization is achieved by simultaneous rotation of the adjacent double and single bonds or a 180° flip of the shared C-H group. In the original bicycle-pedal mechanism, two C-H groups undergo a 180° rotation, propagating the cis-bond further until single bonds are reached.[200] This mechanism, with more or less modifications, was computationally confirmed for several rhodopsins.[71]

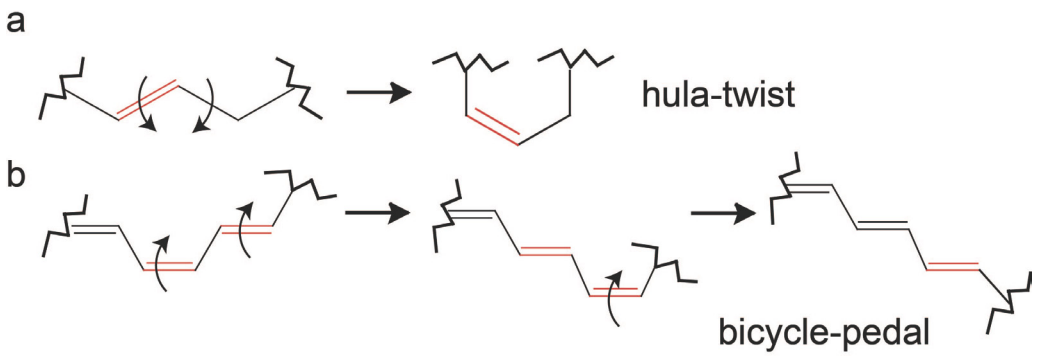

Figure 28. Volume-conserving photoisomerization mechanisms. a, The hula-twist isomerization. **b**, The bicycle-pedal isomerization.

In case of bR, this altered mechanism is termed aborted double bicycle-pedal isomerization[72] or folding-table[201]. Here, the adjacent double bonds C11=C12 and C15=N are predicted to undergo a limited concurrent counter-clockwise (CCW) twisting, while the C13=C14 twists in the clockwise (CW) direction. This alternating twisting facilitates isomerization in a confined binding pocket.[72]

In the TR-SFX derived structures, all three retinal double bonds twist in the same directions as described in the computational study (CCW, CW, CCW, Table 16).[72] Especially for the torsion around C11=C12, only a change of a few degrees is observed in the X-ray data. However, the C15=N bond undergoes more pronounced motion (Figure 29) than in the computational work, possibly because of the way the last atom, the lysine ε-carbon, was defined in the QM model. While the direction of motion is in alternating directions when judging the double bonds as separated species based on torsion angles, when looking at the entire section on the molecule as a whole, it appears as if the C13=C14 and C15=N double

bonds are were twisting in the same direction (Figure 29), resembling an actual bicycle-pedal motion.

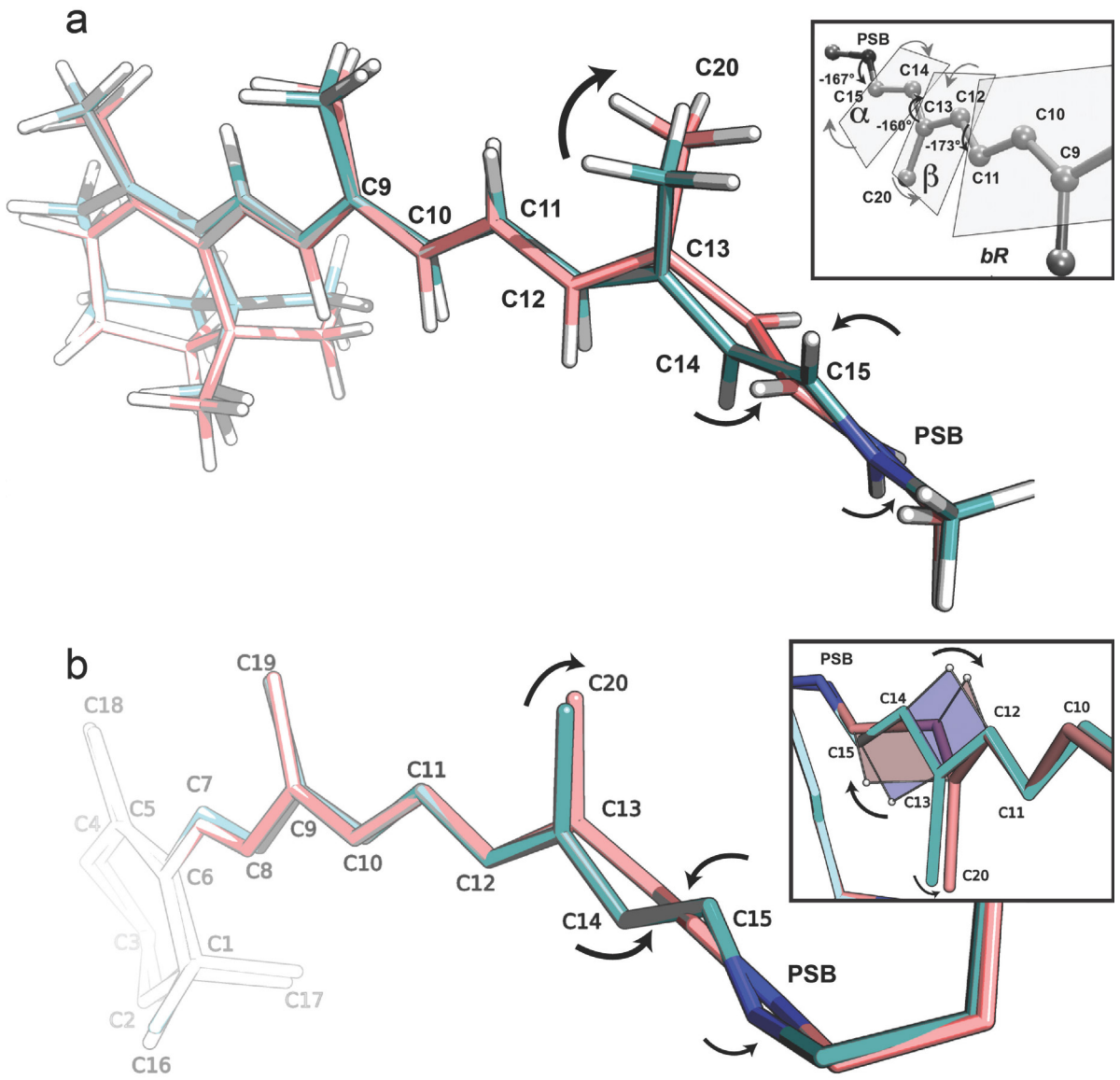

Figure 29. Twisting of bonds during the retinal isomerization in bR. Ground-state and intermediate structures of bR are displayed as cyan and salmon sticks, resp. The arrows indicate the direction of the motion. **a**, Structures of the bR ground state and a twisted (the C12-C13=C14-C15 torsion angle is -100°)[72] intermediate corresponding to the conical intersection stage obtained from quantum mechanical calculations.[72] The mobile Wat402 setup coordinates were used for this figure. The inset shows a ground state structure with the twisting of the planes that define the torsion angles of C13=C14 and C11=C12 and was adapted from figure 4B in the publication Altoe *et al.*, 2010.[72] **b**, Ground-state and 490-fs structures of bR from the TR-SFX experiment. The twisting of the bonds is in the same direction as shown in **a**, and while there is hardly any twisting at C11=C12, motion of the PSB seems more pronounced in the X-ray data. The inset shows the two planes defining the C12-C13=C14-C15 torsion angle and how these change during the isomerization (blue planes correspond to the ground state, pink planes to the intermediate state). It shows the same direction of rotation as is in the upper inset shown between the α and β plane.

For the purpose of a quantitative analysis of the observed torsion angle values, the retinal is considered isomerized when the torsion angle twists beyond -90°. The observed angle is an apparent angle that represents a superposition of all light-induced changes in the retinal molecules in the crystal. Therefore, even torsion angles, which would never accumulate in the crystal due to their instability, such as a -90° twisted structure, can be observed as apparent angles. If the processes and their contribution to the structural changes are known, as they are in the single-photon regime, one can mathematically correct the angle values to only obtain the torsion angle values of the isomerizing photoproduct. In the single-photon regime, the ground state retinal S_0 is excited to the S_1 excited state, from which it decays through the conical intersection at ~500 fs to the hot 13-*cis* retinal ground state (photoproduct), with a quantum yield of ~0.67, or back to a hot all-*trans* retinal (Figure 30).[72] Since only one process contributes to the photoproduct, and the branching of the two reactions is known (2:1), corrected angle values only representing the isomerization towards the 13-*cis* isomer can be obtained. Both the values of apparent and corrected torsion angles should follow an (bi)exponential curve, where the corrected angle values then specifically reflect the formation of the 13-*cis* retinal.

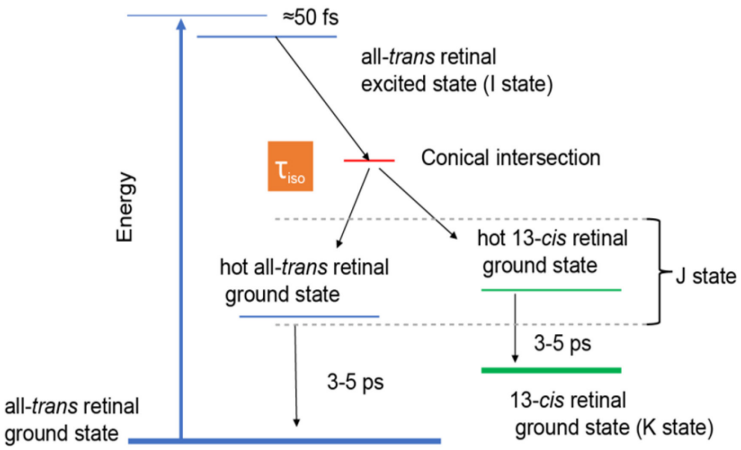

Figure 30. Schematic of the photoisomerization process in bR. Upon photoexcitation, the all-*trans* retinal excited S_1 state (I state) decays via a conical intersection to the 13-*cis* retinal S_0 state (green, forward-reaction) and back to the all-*trans* S_0 state (blue, back-reaction). The time constant of the isomerization (τ_{iso}) is defined as the decay of the I-state and rise of the J-state difference e.g in VIS/IR spectra. During formation of the J-state both hot all-*trans* and hot 13-*cis* retinal ground state coexist which differ from the all-*trans* ground state. This figure was prepared by Stefan Haacke.

In the TR-SFX crystal structures, the extent of the torsion around the C13=C14 double bond on the sub-ps time-scale does not go beyond -90°. The closest to this value is the 0.49 ps time-point (-126°), and then the values decrease (Figure 31). These points cannot be described by a simple exponential function in contrast to a single-photon process. The

reasons for that may be that at the multiphoton excitation intensities used in this experiment, excitation to higher exited states S_n via ESA is possible.[188] These states may decay through the initial S_1 and to the same conical intersection as 1-photon processes, or decay through other channels to a hot all-*trans* or hot 13-*cis* retinal.[202] As the ongoing processes and their relative contributions are unknown, no simple mathematical corrections can be done, therefore the time constant of the isomerization cannot be obtained.

The 1 ps and 3 ps values progress towards a more twisted structure, but stay below -90°, whereas the 10 ps structure resulting from the refinement of the QM model in the electron density finally features a twisted isomerized 13-*cis* retinal (-68°). The 33-ms structure contains a planar isomerized 13-*cis* retinal and the occupancy of this intermediate is comparable to the occupancy of the ultrafast intermediates within the error (occupancy 10-15 %). This confirms that an appreciable amount of photoproduct is formed. Therefore, disregarding what processes electron densities of the (sub-)ps data represent, the productive pathway is ultimately "joined" by a considerable fraction of the bR molecules, yielding an intermediate indistinguishable from the M intermediate obtained with single-photon excitation intensities (Figure 16).

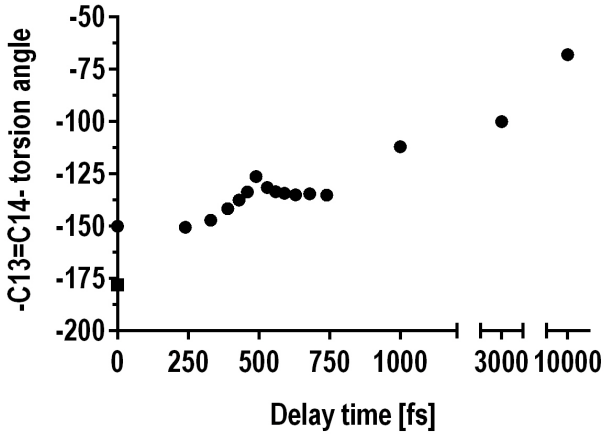

Figure 31. The value of the –C13=C14- torsion angle in time. Values are in Table 16. All dots were refined with loose constraints on the retinal geometry. The square at time=0 is the torsion angle value obtained when constraining the retinal geometry in the same manner as done in previous ground state structures.

In the 3 and 10 ps structures, the steric effect of Tyr185 on retinal is apparent as it restricts the C20 methyl group from rotating further towards it (Figure 15). Motion in other directions is also sterically limited; mainly by aromatic residues Trp86 and Trp182 (see e.g. Figure 3). Notably, these three aromatic residues are perfectly conserved among ion-pumping microbial rhodopsins.[17] It is suggestive that this arrangement plays a key role in how the protein stabilizes the all-*trans* configuration in the ground state and restrains

isomerization to only the C13=C14 double bond. Indeed, experiments with 13-demethylretinal reconstituted bR show that the protein contains predominantly the 13-*cis* isomer and undergoes neither light-dark adaptation, nor a functional photocycle.[88] Interestingly, aromatic residues corresponding to Trp182 and Tyr185 are also lining the binding pocket in visual rhodopsin, however here the pocket is much wider. It allows the more "voluminous" isomerization of 11-*cis* to all-*trans* retinal requiring larger conformational rearrangements of the retinal in the binding pocket.[203]

In the single-photon photocycle, a time-delay of 10 ps would correspond to an early K intermediate (K_E), which forms at ~3ps[46] and at ~70ps it relaxes to a more planar late K (K_L) that decays with 1-2 µs. In K_E, the positive charge localizes back on the PSB and the bond order is restored, yet the chromophore is still highly twisted.[65] During the transition to K_L, which encompasses a relaxation of the chromophore and protein, energy stored in the chromophore is transferred into perturbations of the PSB environment,[74] and the PSB forms a stronger hydrogen bond to the counterion.[73] When comparing the 10-ps structure obtained under multiphoton excitation to an TR-SFX structure of bR at 16 ns,[87] which would correspond to a K_L, the relaxation of the twisted C13=C14 angle (-68°) to a nearly planar configuration (-36°) is apparent. The PSB hydrogen bonding is similar (PSB-Wat402 distance is 3.0 Å and 2.9 Å at 10 ps and 16 ns, resp.) and undergoes more pronounced changes later in the 760 ns structure from the same study.[87] The structures of cryo-trapped K_{LT} neither corresponds to K_E nor K_L, as this highly twisted and unrelaxed state is a temperature artefact.[74]

4.4. Ultrafast changes in the water network

An extensive network of hydrogen-bonded water molecules spans from the retinal all the way to the extracellular site and is essential for the proton pumping activity.[54] Retinal is connected to this network via the hydrogen bond between PSB and Wat402, which is one of the points of the pentagonal cluster additionally formed by Asp212, Asp85, Wat401 and Wat406 (see e.g. Figure 2).[182] This part of the network is also important for the ultrafast intermediates as it stabilizes the positive charge on PSB.[197] Information on ultrafast motion of bR water molecules has been inferred from low-temperature FTIR spectroscopy on cryo-trapped K_{LT} and computational studies. These predict reorientation of the PSB N-H bond upon sudden polarization and weakening of the hydrogen bonds in the pentagonal cluster as the main features of K.[72,204] At the resolution of our X-ray data, hydrogens are not visible and thus the motion of the N-H unit can only be inferred from small changes in the N position. Changes of positions of ordered waters (their oxygen atoms), however, can be accurately

determined and a comparison of the distances in the pentagonal cluster with values obtained from published QM calculations is possible.[72]

The TR-SFX data shows a large displacement of Wat402 away from the PSB, indicating weakening of this hydrogen bond, but not its breakage, which is indicated by the published QM results.[72] There, it is due to a large displacement of the hydrogen in N-H, which cannot be observed in the TR-SFX data. Thus, a breakage of the bond cannot be excluded based in the TR-SFX data. In line with the QM study, the hydrogen bonds between Wat402 and Asp85 and Asp212 become weaker, and the weaker bond to Asp212 likely breaks. Disorder is also apparent at Wat401, weakening the hydrogen bond to Asp85. In addition, rearrangements are also apparent at the extracellular site, where Arg82 moves closer to Wat403, which has weakened hydrogen bonds with all other bonding partners (Wat404, Glu194 and Glu204). Overall this picture agrees well with the described disorder of the pentagonal cluster in K, which here is seen to further propagate to the extracellular half. It is also consistent with the hypothesis that the photon energy stored in K originates partly from the strained retinal and partly from the weakened hydrogen bonding network.[72]

4.5. Comparison with a similar experiment

Results from a similar TR-SFX experiment were published during the revision of the manuscript describing results of this work (Nass Kovacs *et al.*, in revision). As in this work, Nogly *et al.*[181] used TR-SFX to study the sub-ps and ps intermediates of bR, in a very similar experimental set-up at the same SFX instrument/XFEL facility. The amount of data collected is larger than in this work, allowing for finer binning of the sub-ps data (18 data sets vs. 12 in this work). Also, the reported microcrystal size (up to 50 μm) is larger, which together with more data resulted in a higher resolution of the electron density maps(1.5 – 1.8 Å). This, in addition to a different data analysis protocol, may be the reasons behind the generally larger structural changes observed in the Nogly *et al.* work than in this work. A detailed comparison is possible with the three deposited structures (49-404 fs, 457-646 fs, 10 ps). The 49-404 fs structure has a –C13=C14- torsion angle of -135°, which is similar to our 0.46 ps structure (-134°), whereas the 457-646 fs structure already yields an isomerized retinal with a torsion angle value of -82°, which lies between our 0.49 ps (-126°) and 10 ps (-68°) dataset. Especially the 457-646 fs structure shows a significantly more bent retinal (largest deviation at C8) than can be seen in this data. The 10 ps structure from Nogly *et al.* has a torsion angle value of -37°, which is a larger change that in this work, but is similar to the torsion angle value in our QM-optimized model (-41°). Nonetheless, all three structures can be accommodated in the 10 ps electron density map from this work (Figure 32).

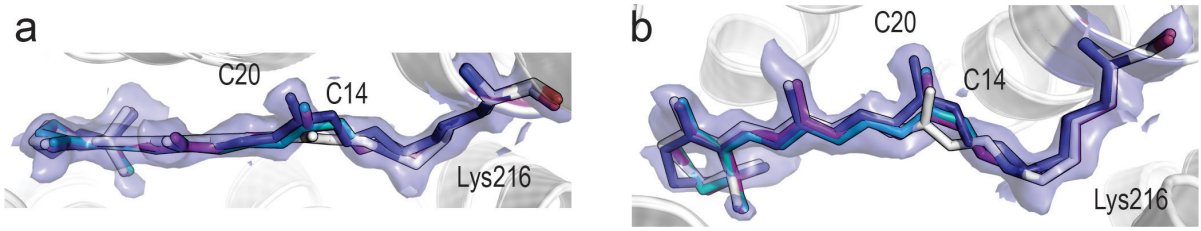

Figure 32. The 10 ps electron density with different 10 ps structures. Top view (**a**) and side view (**b**) of the retinal binding pocket are shown. Retinal dark state, 10 ps structure refined from the QM model, unrefined QM model and the 10 ps structure from Nogly et al.[181] are shown as white, purple, teal and deep blue sticks, respectively. The extrapolated electron density map of the 10 ps time-point (purple surface) is contoured at 1 σ.

Similarly to the faster evolution of the twisting around the C13=C14 double bond in the Nogly *et al.* study, the changes in the distance in the water network are also much more pronounced (Figure 33). The PSB-Wat402 hydrogen bond clearly breaks, as does the Asp212-Wat402 bond, whereas the Asp212-Tyr185 bond becomes shorter. The disorder of Wat401and Wat406 and of the water in the extracellular site is larger than observed in this work.

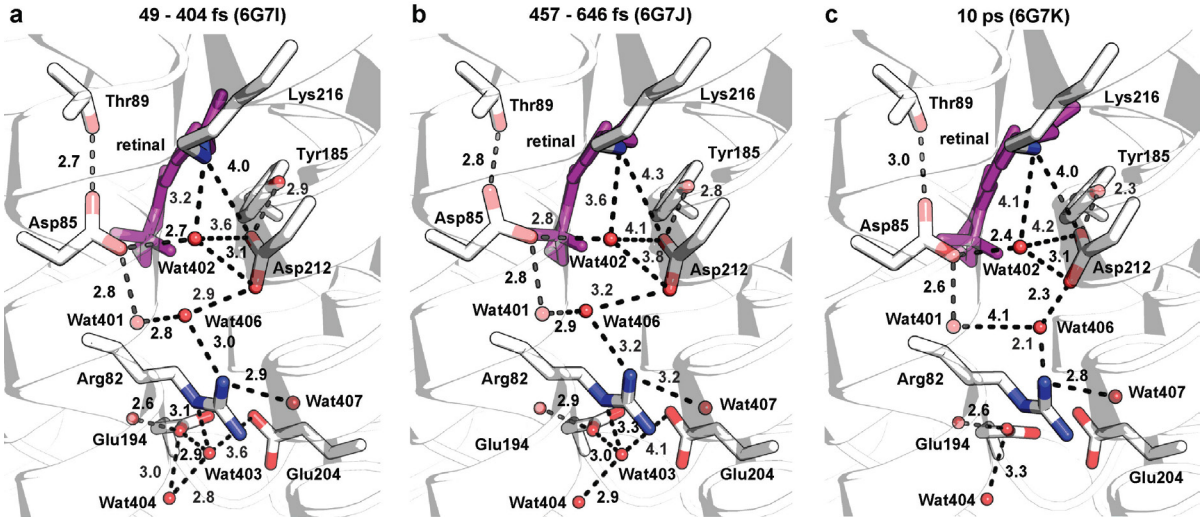

Figure 33. Distances between residues and waters from the Nogly *et al.* study[181]. Retinal is shown in pink and waters as red spheres. Distances are given in Å, those changing significantly are shown in green. **a**, The 49 – 404 fs structure from (6G7I). **b**, The 457 – 646 fs structure (6G7J). **c**, The 10 ps structure (6G7K).

Notably, no oscillations in the retinal nor in the protein were reported.

The study of Nogly *et al.* also reports a later intermediate collected at 8.3 ms, which also coincides with the M intermediate.[181] A difference density map between our 33 ms structure and the 8.3 ms structure reveals more light-induced changes in our 33 ms structure (Figure 16). This is very likely due to a different data collection procedure used for the 8.3 ms structure, in which the crystals were more distant from the pump laser and thus were

pumped with only a very small fraction of the pump laser intensity, resulting in less occupancy of the intermediate.

Several other differences in the experimental set-up can be identified. There was no online-preillumination of crystals and paraffin was used instead of Pluronic to adjust the flow-properties of the LCP stream. More importantly, the authors report to have quantified the scattering of light from the LCP jet (without crystals) to be 80%, without any experimental details. This is in stark contrast to the result of only 20% scattering (with crystals) in this work. If one takes this value for the recalculation of the excitation intensity used in Nogly *et al.*, including a correction of the neglected factor of 2 in their peak power calculation, both studies turn out to have been performed at a similar intensity of 400-500 GW/cm^2, therefore clearly in the non-linear regime where multiphoton effects occur. This implicates that the assumption of the authors that all their observations originate from single-photon absorption processes only is incorrect. Consequently, the assignment of the observed structural changes to single-photon events only and the mechanistic implications are put into question.

4.6. Conclusions and outlook

This work established that time-resolved crystallography at XFELs (SFX) using viscous streams carrying protein microcrystals is feasible and that small light-induced structural changes can be resolved in time even when the occupancy of the intermediate states is very low.

To achieve this, the main experimental challenges - reproducible preparation of well-diffracting microcrystals, identification of optimal injection conditions and pre-illumination of the sample – were addressed here. This opens the door for similar experiments using samples that are not available in ample quantities and require already established protocols in order to efficiently collect data. These can be either other membrane proteins crystallized in lipidic cubic phase, such as anion channelrhodopsin crystallized in this work, or soluble protein crystals that are embedded in viscous carrier matrices, which were also characterized in this work.

The TR-SFX data on photoexcited bacteriorhodopsin allows following light-induced structural changes on the sub-ps and ps timescale. An evolution of rearrangements in the chromophore and in the protein is observed. Due to the high intensity of the optical pump pulse used in this TR-SFX experiment, the probability for multiphoton excitation occurring in the sample is high. This fact was acknowledged and further spectroscopic and computational work was carried out to gain more insights into multiphoton processes. A new channel for the decay of the multiphoton excited retinal was identified, which is based on the strong electronic coupling of the retinal excited state and Trp86 charge-transfer state, resulting in an excited state of Trp86. Concerning the observed structural changes in the TR-SFX data, such as the isomerization reaction and the oscillations in the chromophore, protein residues and ordered water molecules, it remains unknown from which processes these originate. Nonetheless, similarities with e.g. the oscillation frequencies reported in spectroscopic and computational studies obtained in a single-photon excitation regime suggest that a system-inherent “elastic” response is observed. Yet, the implications for the single-photon regime can only be clarified by follow-up work.

This exemplifies that future ultrafast TR-SFX experiments interested in unveiling of functional processes need to focus on investigating optimal photoexcitation intensities, since this essential experimental characterization has been underestimated so far. The aim is to find photoexcitation protocols ensuring mostly single-photon excitation while yielding observable light-induced structural changes, which is non-trivial with optically thick samples. Once single-photon excitation conditions are known, the knowledge provided in this work can then be used to design data collection such that the features observed here for the first time are studied in more detail and their relation to the functional events can be

clarified. This could allow judging whether or not the concerted motions of the nearby protein residues and waters are a part of the mechanism by which the protein actively controls the isomerization reaction of the chromophore.

5. References

1 Palczewski, K. in *Annu. Rev. Biochem.* Vol. 75 *Annu. Rev. Biochem.* 743-767 (2006).

2 Shichida, Y. & Matsuyama, T. Evolution of opsins and phototransduction. *Philos. Trans. Royal Soc. B* **364**, 2881-2895, doi:10.1098/rstb.2009.0051 (2009).

3 Provencio, I. *et al.* A Novel Human Opsin in the Inner Retina. *J Neurosci* **20**, 600-605, doi:10.1523/jneurosci.20-02-00600.2000 (2000).

4 Ernst, O. P. *et al.* Microbial and Animal Rhodopsins: Structures, Functions, and Molecular Mechanisms. *Chem. Rev* **114**, 126-163, doi:10.1021/cr4003769 (2014).

5 Oesterhe.D & Stoecken.W. Rhodopsin-like protein from purple membrane of *Halobacterium halobium Nature New Biol* **233**, 149-& (1971).

6 Matsuno-Yagi, A. & Mukohata, Y. 2 Possible Roles of Bacteriorhodopsin - Comparative-Study of Strains of Halobacterium-Halobium Differing in Pigmentation. *Biochem Bioph Res Co* **78**, 237-243 (1977).

7 Schobert, B. & Lanyi, J. K. Halorhodopsin is a light-driven chloride pump. *J Biol Chem* **257**, 10306-10313 (1982).

8 Bogomolni, R. A. & Spudich, J. L. Identification of a 3rd rhodopsin-like pigment in phototactic *Halobacterium halobium*. *Proc. Natl. Acad. Sci. USA* **79**, 6250-6254, doi:10.1073/pnas.79.20.6250 (1982).

9 Spudich, E. N. & Spudich, J. L. Control of transmembrane ion fluxes to select halorhodopsin-deficient and other energy-transduction mutants of Halobacterium halobium. *Proc. Natl. Acad. Sci. USA* **79**, 4308-4312, doi:10.1073/pnas.79.14.4308 (1982).

10 Tomioka, H., Takahashi, T., Kamo, N. & Kobatake, Y. Flash spectrophotometric identification of a fourth rhodopsin-like pigment in Halobacterium halobium. *Biochem. Biophys. Res. Commun* **139**, 389-395, doi:10.1016/S0006-291X(86)80003-1 (1986).

11 Spudich, E. N., Sundberg, S. A., Manor, D. & Spudich, J. L. Properties of a second sensory receptor protein in Halobacterium halobium phototaxis. *Proteins: Struct., Funct., Bioinf.* **1**, 239-246, doi:doi:10.1002/prot.340010306 (1986).

12 Nagel, G. *et al.* Channelrhodopsin-1: A light-gated proton channel in green algae. *Science* **296**, 2395-2398, doi:10.1126/science.1072068 (2002).

13 Nagel, G. *et al.* Channelrhodopsin-2, a directly light-gated cation-selective membrane channel. *Proc Nat Acad Sci USA* **100**, 13940-13945, doi:10.1073/pnas.1936192100 (2003).

14 Govorunova, E. G., Sineshchekov, O. A., Janz, R., Liu, X. Q. & Spudich, J. L. Natural light-gated anion channels: A family of microbial rhodopsins for advanced optogenetics. *Science* **349**, 647-650, doi:10.1126/science.aaa7484 (2015).

15 Soppa, J. Sequence comparison does not support an evolutionary link between halobacterial retinal proteins including bacteriorhodopsin and eukaryotic G-protein coupled receptors. *FEBS Lett* **342**, 7-11, doi:10.1016/0014-5793(94)80573-3 (1994).

16 Beja, O. *et al.* Bacterial rhodopsin: Evidence for a new type of phototrophy in the sea. *Science* **289**, 1902-1906 (2000).

17 Kandori, H. Ion-pumping microbial rhodopsins. *Front. Biosci* **2**, doi:10.3389/fmolb.2015.00052 (2015).

18 Deisseroth, K. *et al.* Next-Generation Optical Technologies for Illuminating Genetically Targeted Brain Circuits. *J Neurosci* **26**, 10380-10386, doi:10.1523/jneurosci.3863-06.2006 (2006).

19 Boyden, E. S. Optogenetics and the future of neuroscience. *Nat Neurosci* **18**, 1200, doi:10.1038/nn.4094 (2015).

20 Deisseroth, K. Optogenetics: 10 years of microbial opsins in neuroscience. *Nat Neurosci* **18**, 1213, doi:10.1038/nn.4091 (2015).

21 Boyden, E. S., Zhang, F., Bamberg, E., Nagel, G. & Deisseroth, K. Millisecond-timescale, genetically targeted optical control of neural activity. *Nat Neurosci* **8**, 1263, doi:10.1038/nn1525 (2005).

22 Sineshchekov, O. A., Govorunova, E. G., Li, H. & Spudich, J. L. Gating mechanisms of a natural anion channelrhodopsin. *Proc Nat Acad Sci USA* **112**, 14236-14241, doi:10.1073/pnas.1513602112 (2015).

23 Sineshchekov, O. A., Li, H., Govorunova, E. G. & Spudich, J. L. Photochemical reaction cycle transitions during anion channelrhodopsin gating. *Proc Nat Acad Sci USA* **113**, E1993-E2000, doi:10.1073/pnas.1525269113 (2016).

24 Blaurock, A. E. & Stoeckenius, W. Structure of the Purple Membrane. *Nature New Biol* **233**, 152, doi:10.1038/newbio233152a0 (1971).

25 Oesterhelt, D. & Stoeckenius, W. Functions of a new photoreceptor membrane. *Proc Natl Acad Sci USA* **70**, 2853-2857 (1973).

26 Danon, A. & Stoeckenius, W. Photophosphorylation in Halobacterium halobium. *Proc Natl Acad Sci USA* **71**, 1234-1238 (1974).

27 Bagley, K., Dollinger, G., Eisenstein, L., Singh, A. K. & Zimányi, L. Fourier transform infrared difference spectroscopy of bacteriorhodopsin and its photoproducts. *Proc Natl Acad Sci USA* **79**, 4972-4976, doi:10.1073/pnas.79.16.4972 (1982).

28 Engelhard, M. *et al.* Magic angle sample spinning carbon-13 nuclear magnetic resonance of isotopically labeled bacteriorhodopsin. *Biochemistry* **28**, 3967-3975, doi:10.1021/bi00435a051 (1989).

29 Braiman, M. & Mathies, R. The resonance Raman spectra of bacteriorhodopsin's primary photoproduct: evidence for a distorted 13-cis retinal chromophore. *Biophys. J* **33**, A216-A216 (1981).

30 Mathies, R. A., Brito Cruz, C. H., Pollard, W. T. & Shank, C. V. Direct observation of the femtosecond excited-state cis-trans isomerization in bacteriorhodopsin. *Science* **240**, 777-779 (1988).

31 Diller, R., Iannone, M., Bogomolni, R. & Hochstrasser, R. M. Ultrafast infrared spectroscopy of bacteriorhodopsin. *Biophys J* **60**, 286-289, doi:10.1016/S0006-3495(91)82050-1 (1991).

32 Landau, E. M. & Rosenbusch, J. P. Lipidic cubic phases: A novel concept for the crystallization of membrane proteins. *Proc Nat Acad Sci USA* **93**, 14532-14535, doi:10.1073/pnas.93.25.14532 (1996).

33 Grote, M., Engelhard, M. & Hegemann, P. Of ion pumps, sensors and channels — Perspectives on microbial rhodopsins between science and history. *Biochim Biophys Acta* **1837**, 533-545, doi:10.1016/j.bbabio.2013.08.006 (2014).

34 Khorana, H. G. *et al.* Amino acid sequence of bacteriorhodopsin. *Proc Natl Acad Sci USA* **76**, 5046-5050 (1979).

35 Henderson, R. & Unwin, P. N. T. Three-dimensional model of purple membrane obtained by electron microscopy. *Nature* **257**, 28, doi:10.1038/257028a0 (1975).

36 Henderson, R. *et al.* Model for the structure of bacteriorhodopsin based on high-resolution electron cryo-microscopy. *J Mol Biol* **213**, 899-929, doi:10.1016/S0022-2836(05)80271-2 (1990).

37 Pebay-Peyroula, E., Rummel, G., Rosenbusch, J. P. & Landau, E. M. X-ray Structure of Bacteriorhodopsin at 2.5 Angstroms from Microcrystals Grown in Lipidic Cubic Phases. *Science* **277**, 1676-1681, doi:10.1126/science.277.5332.1676 (1997).

38 Wickstrand, C., Dods, R., Royant, A. & Neutze, R. Bacteriorhodopsin: Would the real structural intermediates please stand up? *BBA-Gen Sub* **1850**, 536-553 (2015).

39 Luecke, H., Schobert, B., Richter, H.-T., Cartailler, J.-P. & Lanyi, J. K. Structural Changes in Bacteriorhodopsin During Ion Transport at 2 Angstrom Resolution. *Science* **286**, 255-260, doi:10.1126/science.286.5438.255 (1999).

40 Edman, K. *et al.* High-resolution X-ray structure of an early intermediate in the bacteriorhodopsin photocycle. *Nature* **401**, 822, doi:10.1038/44623 (1999).

41 Lanyi, J. K. & Schobert, B. Mechanism of Proton Transport in Bacteriorhodopsin from Crystallographic Structures of the K, L, M1, M2, and M2′ Intermediates of the Photocycle. *J Mol Biol* **328**, 439-450, doi:10.1016/S0022-2836(03)00263-8 (2003).

42 Schobert, B., Brown, L. S. & Lanyi, J. K. Crystallographic Structures of the M and N Intermediates of Bacteriorhodopsin: Assembly of a Hydrogen-bonded Chain of Water Molecules Between Asp-96 and the Retinal Schiff Base. *J Mol Biol* **330**, 553-570, doi:10.1016/S0022-2836(03)00576-X (2003).

43 Zhang, J. *et al.* Crystal structure of the O intermediate of the Leu93→Ala mutant of bacteriorhodopsin. *Proteins: Struct., Funct., Bioinf.* **80**, 2384-2396, doi:doi:10.1002/prot.24124 (2012).

44 Kandt, C., Schlitter, J. & Gerwert, K. Dynamics of Water Molecules in the Bacteriorhodopsin Trimer in Explicit Lipid/Water Environment. *Biophys J* **86**, 705-717, doi:10.1016/S0006-3495(04)74149-1 (2004).

45 Maeda, A., Iwasa, T. & Yoshizawa, T. Isomeric Composition of Retinal Chromophore in Dark-Adapted Bacteriorhodopsin. *Biochem J* **82**, 1599-1604 (1977).

46 Diller, R. *et al.* Femtosecond time-resolved infrared laser study of the J-K transition of bacteriorhodopsin. *Chem Phys Lett* **241**, 109-115, doi:10.1016/0009-2614(95)00598-x (1995).

47 Gat, Y. & Sheves, M. A mechanism for controlling the pKa of the retinal protonated Schiff base in retinal proteins. A study with model compounds. *J Am Chem Soc* **115**, 3772-3773, doi:10.1021/ja00062a052 (1993).

48 Druckmann, S., Ottolenghi, M., Pande, A., Pande, J. & Callender, R. H. Acid-base equilibrium of the Schiff base in bacteriorhodopsin. *Biochemistry* **21**, 4953-4959, doi:10.1021/bi00263a019 (1982).

49 Chang, C.-H., Chen, J.-G., Govindjee, R. & Ebrey, T. Cation binding by bacteriorhodopsin. *Proc Natl Acad Sci USA* **82**, 396-400, doi:10.1073/pnas.82.2.396 (1985).

50 Gerwert, K., Souvignier, G. & Hess, B. Simultaneous monitoring of light-induced changes in protein side-group protonation, chromophore isomerization, and backbone motion of

bacteriorhodopsin by time-resolved Fourier-transform infrared spectroscopy. *Proceedings of the National Academy of Sciences* **87**, 9774-9778, doi:10.1073/pnas.87.24.9774 (1990).

51 Garczarek, F. & Gerwert, K. Functional waters in intraprotein proton transfer monitored by FTIR difference spectroscopy. *Nature* **439**, 109, doi:10.1038/nature04231 (2005).

52 Wolf, S., Freier, E., Potschies, M., Hofmann, E. & Gerwert, K. Directional Proton Transfer in Membrane Proteins Achieved through Protonated Protein-Bound Water Molecules: A Proton Diode. *Angew. Chem. Int. Ed.* **49**, 6889-6893, doi:doi:10.1002/anie.201001243 (2010).

53 Brown, L. S., Dioumaev, A. K., Needleman, R. & Lanyi, J. K. Local-Access Model for Proton Transfer in Bacteriorhodopsin. *Biochemistry* **37**, 3982-3993, doi:10.1021/bi9728396 (1998).

54 Freier, E., Wolf, S. & Gerwert, K. Proton transfer via a transient linear water-molecule chain in a membrane protein. *Proc. Natl. Acad. Sci. USA* **108**, 11435-11439, doi:10.1073/pnas.1104735108 (2011).

55 Otto, H. *et al.* Substitution of amino acids Asp-85, Asp-212, and Arg-82 in bacteriorhodopsin affects the proton release phase of the pump and the pK of the Schiff base. *Proc Natl Acad Sci USA* **87**, 1018-1022, doi:10.1073/pnas.87.3.1018 (1990).

56 Yabushita, A. & Kobayashi, T. Primary Conformation Change in Bacteriorhodopsin on Photoexcitation. *Biophys. J* **96**, 1447-1461, doi:10.1016/j.bpj.2008.10.050 (2009).

57 Colonna, A., Groma, G. I., Martin, J. L., Joffre, M. & Vos, M. H. Quantification of sudden light-induced polarization in bacteriorhodopsin by optical rectification. *J. Phys. Chem. B* **111**, 2707-2710, doi:10.1021/jp0673462 (2007).

58 Groma, G. I. *et al.* Resonant optical rectification in bacteriorhodopsin. *Proc Natl Acad Sci U S A* **101**, 7971-7975 (2004).

59 Gonzalez-Luque, R. *et al.* Computational evidence in favor of a two-state, two-mode model of the retinal chromophore photoisomerization. *Proc. Natl. Acad. Sci. USA* **97**, 9379-9384, doi:10.1073/pnas.97.17.9379 (2000).

60 Mathies, R. & Stryer, L. Retinal has a highly dipolar vertically excited singlet state: implications for vision. *Proc Natl Acad Sci USA* **73**, 2169-2173 (1976).

61 Song, L. & El-Sayed, M. A. Primary step in bacteriorhodopsin photosynthesis: Bond stretch rather than angle twist of its retinal excited-state structure. *J Am Chem Soc* **120**, 8889-8890 (1998).

62 Sharkov, A. V., Pakulev, A. V., Chekalin, S. V. & Matveetz, Y. A. Primary events in bacteriorhodopsin probed by subpicosecond spectroscopy. *Biochim Biophys Acta* **808**, 94-102, doi:10.1016/0005-2728(85)90031-3 (1985).

63 Du, M. & Fleming, G. R. Femtosecond time-resolved fluorescence spectroscopy of bacteriorhodopsin - direct observation of excited-state dynamics in the primary step of the proton pump cycle. *Biophys. Chem* **48**, 101-111, doi:10.1016/0301-4622(93)85002-y (1993).

64 Garavelli, M., Negri, F. & Olivucci, M. Initial Excited-State Relaxation of the Isolated 11-cis Protonated Schiff Base of Retinal: Evidence for in-Plane Motion from ab Initio Quantum Chemical Simulation of the Resonance Raman Spectrum. *J. Am. Chem. Soc.* **121**, 1023-1029, doi:10.1021/ja981719y (1999).

65 Shim, S., Dasgupta, J. & Mathies, R. A. Femtosecond Time-Resolved Stimulated Raman Reveals the Birth of Bacteriorhodopsin's J and K Intermediates. *J Am Chem Soc* **131**, 7592-7597 (2009).

66 Hou, B. X., Friedman, N., Ottolenghi, M., Sheves, M. & Ruhman, S. Comparing photoinduced vibrational coherences in bacteriorhodopsin and in native and locked retinal protonated Schiff bases. *Chem Phys Lett* **381**, 549-555 (2003).

67 Wand, A., Gdor, I., Zhu, J. Y., Sheves, M. & Ruhman, S. in *Annu. Rev. Phys. Chem* Vol. 64 *Annual Review of Physical Chemistry* (eds M. A. Johnson & T. J. Martinez) 437-458 (2013).

68 Herbst, J., Heyne, K. & Diller, R. Femtosecond infrared spectroscopy of bacteriorhodopsin chromophore isomerization. *Science* **297**, 822-825, doi:10.1126/science.1072144 (2002).

69 Nuss, M. C., Zinth, W., Kaiser, W., Kolling, E. & Oesterhelt, D. Femtosecond spectroscopy of the first events of the photochemical cycle in bacteriorhodopsin. *Chem Phys Lett* **117**, 1-7, doi:10.1016/0009-2614(85)80393-6 (1985).

70 Dobler, J., Zinth, W., Kaiser, W. & Oesterhelt, D. Excited-State Reaction Dynamics of Bacteriorhodopsin Studied by Femtosecond Spectroscopy. *Chem Phys Lett* **144**, 215-220 (1988).

71 Gozem, S., Luk, H. L., Schapiro, I. & Olivucci, M. Theory and Simulation of the Ultrafast Double-Bond Isomerization of Biological Chromophores. *Chem Rev* **117**, 13502-13565 (2017).

72 Altoe, P., Cembran, A., Olivucci, M. & Garavelli, M. Aborted double bicycle-pedal isomerization with hydrogen bond breaking is the primary event of bacteriorhodopsin proton pumping. *Proc Natl Acad Sci USA* **107**, 20172-20177 (2010).

73 Doig, S. J., Reid, P. J. & Mathies, R. A. Picosecond Time-Resolved Resonance Raman-Spectroscopy of Bacteriorhodopsin-J, Bacterlorhodopsin-K, Bacterlorhodopsin-Kl Intermediates. *J Phys Chem* **95**, 6372-6379 (1991).

74 Dioumaev, A. K. & Braiman, M. S. Two Bathointermediates of the Bacteriorhodopsin Photocycle, Distinguished by Nanosecond Time-Resolved FTIR Spectroscopy at Room Temperature. *J Phys Chem B* **101**, 1655-1662, doi:10.1021/jp961512w (1997).

75 Lewis, A. The molecular mechanism of excitation in visual transduction and bacteriorhodopsin. *Proc Natl Acad Sci USA* **75**, 549-553 (1978).

76 Kennis, J. T. M. *et al.* Ultrafast protein dynamics of bacteriorhodopsin probed by photon echo and transient absorption spectroscopy. *J Phys Chem B* **106**, 6067-6080 (2002).

77 Xu, D., Martin, C. & Schulten, K. Molecular dynamics study of early picosecond events in the bacteriorhodopsin photocycle: Dielectric response, vibrational cooling and the J, K intermediates. *Biophys. J* **70**, 453-460 (1996).

78 Gross, R. *et al.* Primary Photoinduced Protein Response in Bacteriorhodopsin and Sensory Rhodopsin II. *J Am Chem Soc* **131**, 14868-14878 (2009).

79 Gross, R. *et al.* Ultrafast protein conformational alterations in bacteriorhodopsin and its locked analogue BR5.12. *J Phys Chem B* **113**, 7851-7860 (2009).

80 Briand, J., Leonard, J. & Haacke, S. Ultrafast photo-induced reaction dynamics in bacteriorhodopsin and its Trp mutants. *J Optics* **12**, doi:10.1088/2040-8978/12/8/084004 (2010).

81 Leonard, J. *et al.* Functional electric field changes in photoactivated proteins revealed by ultrafast Stark spectroscopy of the Trp residues. *Proc Natl Acad Sci USA* **106**, 7718-7723 (2009).

82 Schenkl, S., van Mourik, F., van der Zwan, G., Haacke, S. & Chergui, M. Probing the ultrafast charge translocation of photoexcited retinal in bacteriorhodopsin. *Science* **309**, 917-920 (2005).

83 Tittor, J. & Oesterhelt, D. The Quantum Yield of Bacteriorhodopsin. *FEBS Lett* **263**, 269-273 (1990).

84 Hamm, P. *et al.* Femtosecond spectroscopy of the photoisomerisation of the protonated Schiff base of all-trans retinal. *Chem Phys Lett* **263**, 613-621, doi:10.1016/S0009-2614(96)01269-9 (1996).

85 Koyama, Y., Kubo, K., Komori, M., Yasuda, H. & Mukai, Y. Effect of protonation on the isomerization properties of n-butylamine Schiff-base of isomeric retinal as revealed by direct HPLC analyses : selection of isomerization pathways by retinal proteins. *Photochem. Photobiol.* **54**, 433-443, doi:10.1111/j.1751-1097.1991.tb02038.x (1991).

86 Schotte, F. *et al.* Watching a protein as it functions with 150-ps time-resolved X-ray crystallography. *Science* **300**, 1944-1947, doi:10.1126/science.1078797 (2003).

87 Nango, E. *et al.* A three-dimensional movie of structural changes in bacteriorhodopsin. *Science* **354**, 1552-1557 (2016).

88 Gartner, W., Towner, P., Hopf, H. & Oesterhelt, D. Removal of Methyl-Groups from Retinal Controls the Activity of Bacteriorhodopsin. *Biochemistry* **22**, 2637-2644 (1983).

89 Pellegrini, C. X-ray free-electron lasers: from dreams to reality. *Phys. Scr.* **T169**, doi:10.1088/1402-4896/aa5281 (2016).

90 Pellegrini, C., Marinelli, A. & Reiche, S. The physics of x-ray free-electron lasers. *Rev. Mod. Phys* **88**, doi:10.1103/RevModPhys.88.015006 (2016).

91 Colletier, J. P. *et al.* De novo phasing with X-ray laser reveals mosquito larvicide BinAB structure. *Nature* **539**, 43-+, doi:10.1038/nature19825 (2016).

92 Gati, C. *et al.* Atomic structure of granulin determined from native nanocrystalline granulovirus using an X-ray free-electron laser. *Proc. Natl. Acad. Sci. USA* **114**, 2247-2252, doi:10.1073/pnas.1609243114 (2017).

93 Liu, W. *et al.* Serial Femtosecond Crystallography of G Protein-Coupled Receptors. *Science* **342**, 1521-1524, doi:10.1126/science.1244142 (2013).

94 Neutze, R., Wouts, R., van der Spoel, D., Weckert, E. & Hajdu, J. Potential for biomolecular imaging with femtosecond X-ray pulses. *Nature* **406**, 752-757, doi:10.1038/35021099 (2000).

95 Chapman, H. N., Caleman, C. & Timneanu, N. Diffraction before destruction. *Philos. Trans. Royal Soc. B* **369**, doi:10.1098/rstb.2013.0313 (2014).

96 Young, I. D. *et al.* Structure of photosystem II and substrate binding at room temperature. *Nature* **540**, 453-+, doi:10.1038/nature20161 (2016).

97 Suga, M. *et al.* Light-induced structural changes and the site of O=O bond formation in PSII caught by XFEL. *Nature* **543**, 131-+, doi:10.1038/nature21400 (2017).

98 Borshchevskiy, V. I., Round, E. S., Popov, A. N., Bueldt, G. & Gordeliy, V. I. X-ray-Radiation-Induced Changes in Bacteriorhodopsin Structure. *J. Mol. Biol* **409**, 813-825, doi:10.1016/j.jmb.2011.04.038 (2011).

99 Aquila, A. *et al.* Time-resolved protein nanocrystallography using an X-ray free-electron laser. *Opt. Express* **20**, 2706-2716, doi:10.1364/oe.20.002706 (2012).

100 Tenboer, J. *et al.* Time-resolved serial crystallography captures high-resolution intermediates of photoactive yellow protein. *Science* **346**, 1242-1246, doi:10.1126/science.1259357 (2014).

101 Nogly, P. *et al.* Lipidic cubic phase injector is a viable crystal delivery system for time-resolved serial crystallography. *Nat. Commun.* **7**, doi:10.1038/ncomms12314 (2016).

102 Barends, T. R. M. *et al.* Direct observation of ultrafast collective motions in CO myoglobin upon ligand dissociation. *Science* **350**, 445-450 (2015).

103 Pande, K. *et al.* Femtosecond structural dynamics drives the trans/cis isomerization in photoactive yellow protein. *Science* **352**, 725-729 (2016).

104 Coquelle, N. *et al.* Chromophore twisting in the excited state of a photoswitchable fluorescent protein captured by time-resolved serial femtosecond crystallography. *Nat. Chem.* **10**, 31, doi:10.1038/nchem.2853 (2017).

105 Schmidt, M. Mix and Inject: Reaction Initiation by Diffusion for Time-Resolved Macromolecular Crystallography. *Adv. Condens. Matter Phys.*, doi:10.1155/2013/167276 (2013).

106 Altarelli, M. & Mancuso, A. P. Structural biology at the European X-ray free-electron laser facility. *Philos. Trans. Royal Soc. B* **369**, doi:10.1098/rstb.2013.0311 (2014).

107 Tschentscher, T. *et al.* Photon Beam Transport and Scientific Instruments at the European XFEL. *Applied Sciences-Basel* **7**, doi:10.3390/app7060592 (2017).

108 Schoenlein, R. W. New Science Opportunities Enabled by LCLS-II X-ray Lasers *SLAC National Accelerator Laboratory* **SLAC-R-1053** (2015).

109 Nass, K. *et al.* Indications of radiation damage in ferredoxin microcrystals using high-intensity X-FEL beams. *J. Synchrotron Radiat* **22**, 225-238, doi:10.1107/s1600577515002349 (2015).

110 Nass, K. *et al.* Protein structure determination by single-wavelength anomalous diffraction phasing of X-ray free-electron laser data. *IUCrJ* **3**, 180-191, doi:10.1107/s2052252516002980 (2016).

111 Briggs, J., Chung, H. & Caffrey, M. The Temperature-Composition Phase Diagram and Mesophase Structure Characterization of the Monoolein/Water System. *J. Phys. II France* **6**, 723-751 (1996).

112 Caffrey, M. & Cherezov, V. Crystallizing membrane proteins using lipidic mesophases. *Nat Protoc* **4**, 706-731, doi:10.1038/nprot.2009.31 (2009).

113 Liu, W., Ishchenko, A. & Cherezov, V. Preparation of microcrystals in lipidic cubic phase for serial femtosecond crystallography. *Nat. Protoc.* **9**, 2123-2134, doi:10.1038/nprot.2014.141 (2014).

114 DePonte, D. P. *et al.* Gas dynamic virtual nozzle for generation of microscopic droplet streams. *J Phys D Appl Phys.* **41**, 195505 (2008).

115 Weierstall, U., Spence, J. C. H. & Doak, R. B. Injector for scattering measurements on fully solvated biospecies. *Rev Sci Instrum* **83**, 035108, doi:10.1063/1.3693040 (2012).

116 Doak, R. B. *et al.* Microscopic linear liquid streams in vacuum: Injection of solvated biological samples into X-ray free electron lasers. *AIP Conference Proceedings* **1501**, 1314-1323, doi:10.1063/1.4769693 (2012).

117 Grünbein, M. L. *et al.* Megahertz data collection from protein microcrystals at an X-ray free-electron laser. *Nat. Commun.* **9**, doi:10.1038/s41467-018-05953-4 (2018).

118 Wiedorn, M. O. *et al.* Megahertz serial crystallography. *Nat Commun* **9**, doi:10.1038/s41467-018-06156-7 (2018).

119 Mueller, C. *et al.* Fixed target matrix for femtosecond time-resolved and in situ serial micro-crystallography. *Struct. Dyn.* **2**, doi:10.1063/1.4928706 (2015).

120 Oghbaey, S. *et al.* Fixed target combined with spectral mapping: approaching 100% hit rates for serial crystallography. *Acta Cryst. D* **72**, 944-955, doi:10.1107/s2059798316010834 (2016).

121 Roedig, P. *et al.* High-speed fixed-target serial virus crystallography. *Nat. Methods* **14**, 805-+, doi:10.1038/nmeth.4335 (2017).

122 Doak, R. B. *et al.* Crystallography on a chip - without the chip: sheet-on-sheet sandwich. *Acta Cryst. D* **74**, 1000-1007, doi:10.1107/s2059798318011634 (2018).

123 Cohen, A. E. *et al.* Goniometer-based femtosecond crystallography with X-ray free electron lasers. *Proc. Natl. Acad. Sci. USA* **111**, 17122-17127, doi:10.1073/pnas.1418733111 (2014).

124 Baxter, E. L. *et al.* High-density grids for efficient data collection from multiple crystals. *Acta Cryst. D* **72**, 2-11, doi:10.1107/s2059798315020847 (2016).

125 Roessler, Christian G. *et al.* Acoustic Injectors for Drop-On-Demand Serial Femtosecond Crystallography. *Structure* **24**, 631-640, doi:10.1016/j.str.2016.02.007 (2016).

126 Mafune, F. *et al.* Microcrystal delivery by pulsed liquid droplet for serial femtosecond crystallography. *Acta Cryst. D* **72**, 520-523, doi:doi:10.1107/S2059798316001480 (2016).

127 Fuller, F. D. *et al.* Drop-on-demand sample delivery for studying biocatalysts in action at X-ray free-electron lasers. *Nat. Methods* **advance online publication**, doi:10.1038/nmeth.4195 (2017).

128 Eriksson, M., van der Veen, J. F. & Quitmann, C. Diffraction-limited storage rings - a window to the science of tomorrow. *J Synchrotron Radiat.* **21**, 837-842, doi:10.1107/s1600577514019286 (2014).

129 Streun, A. *et al.* SLS-2-the upgrade of the Swiss Light Source. *J Synchrotron Radiat.* **25**, 631-641, doi:10.1107/s1600577518002722 (2018).

130 Chenevier, D. & Joly, A. ESRF: Inside the Extremely Brilliant Source Upgrade. *Synchrotron Radiat. News* **31**, 32-35, doi:10.1080/08940886.2018.1409562 (2018).

131 Wanzenberg, R. *et al.* Research Activities Towards a Conversion of PETRA III Into a Diffraction Limited Synchrotron Light Source. *Proc. of IPAC2017*, WEPIK065, doi:10.18429/JACoW-IPAC2017-WEPIK065 (2017).

132 Tanaka, H. *et al.* SPring-8 Upgrade Project. *Proc. of IPAC2016*, WEPOW019, doi:10.18429/JACoW-IPAC2016-WEPOW019 (2016).

133 Botha, S. *et al.* Room-temperature serial crystallography at synchrotron X-ray sources using slowly flowing free-standing high-viscosity microstreams. *Acta Cryst. D* **71**, 387-397 (2015).

134 Nogly, P. *et al.* Lipidic cubic phase serial millisecond crystallography using synchrotron radiation. *IUCrJ* **2**, 168-176 (2015).

135 Stellato, F. *et al.* Room-temperature macromolecular serial crystallography using synchrotron radiation. *IUCrJ* **1**, 204-212, doi:10.1107/s2052252514010070 (2014).

136 Roedig, P. *et al.* Room-temperature macromolecular crystallography using a micro-patterned silicon chip with minimal background scattering. *J. Appl. Crystallogr.* **49**, 968-975, doi:10.1107/s1600576716006348 (2016).

137 Martin-Garcia, J. M. *et al.* Serial millisecond crystallography of membrane and soluble protein microcrystals using synchrotron radiation. *IUCrJ* **4**, 439-454, doi:10.1107/s205225251700570x (2017).

138 Weinert, T. *et al.* Serial millisecond crystallography for routine room-temperature structure determination at synchrotrons. *Nat. Commun.* **8**, 542, doi:10.1038/s41467-017-00630-4 (2017).

139 Roedig, P. *et al.* A micro-patterned silicon chip as sample holder for macromolecular crystallography experiments with minimal background scattering. *Sci. Rep.* **5**, 10451, doi:10.1038/srep10451 (2015).

140 Grunbein, M. L. & Nass Kovacs, G. Sample delivery for serial crystallography at free-electron lasers and synchrotrons. *Acta Cryst. D* **75**, doi:doi:10.1107/S205979831801567X (2019).

141 Zhao, Y. G., Chapman, D. A. G. & Jones, I. M. Improving baculovirus recombination. *Nucleic Acids Res.* **31**, doi:10.1093/nar/gng006 (2003).

142 Kovacsova, G. *et al.* Viscous hydrophilic injection matrices for serial crystallography. *IUCrJ* **4**, doi:doi:10.1107/S2052252517005140 (2017).

143 Laemmli, U. K. Cleavage of Structural Proteins during the Assembly of the Head of Bacteriophage T4. *Nature* **227**, 680, doi:10.1038/227680a0 (1970).

144 Reisinger, V. & Eichacker, L. A. Analysis of membrane protein complexes by blue native PAGE. *Proteomics*, 6-15, doi:10.1002/pmic.200600553 (2006).

145 Scherrer, P., Mathew, M. K., Sperling, W. & Stoeckenius, W. Retinal Isomer Ratio in Dark-Adapted Purple Membrane and Bacteriorhodopsin Monomers. *Biochemistry* **28**, 829-834 (1989).

146 Muders, V. *et al.* Resonance Raman and FTIR spectroscopic characterization of the closed and open states of channelrhodopsin-1. *Febs Lett* **588**, 2301-2306, doi:10.1016/j.febslet.2014.05.019 (2014).

147 Hattne, J. *et al.* Accurate macromolecular structures using minimal measurements from X-ray free-electron lasers (vol 11, pg 545, 2014). *Nat Methods* **12**, 692-692 (2015).

148 Sugahara, M. *et al.* Grease matrix as a versatile carrier of proteins for serial crystallography. *Nat. Methods* **12**, 61-63, doi:10.1038/nmeth.3172 (2015).

149 Conrad, C. E. *et al.* A novel inert crystal delivery medium for serial femtosecond crystallography. *IUCrJ* **2**, 421-430, doi:10.1107/s2052252515009811 (2015).

150 Sugahara, M. *et al.* Oil-free hyaluronic acid matrix for serial femtosecond crystallography. *Sci. Rep.* **6**, 24484, doi:10.1038/srep24484 (2016).

151 Kabsch, W. Processing of X-ray snapshots from crystals in random orientations. *Acta Cryst. D* **70**, 2204-2216, doi:10.1107/s1399004714013534 (2014).

152 Liang, M. N. *et al.* The Coherent X-ray Imaging instrument at the Linac Coherent Light Source. *J Synchrotron Radiat* **22**, 514-519, doi:10.1107/s160057751500449x (2015).

153 Bionta, M. R. *et al.* Spectral encoding of x-ray/optical relative delay. *Opt Express* **19**, 21855-21865 (2011).

154 Blaj, G. *et al.* X-ray detectors at the Linac Coherent Light Source. *J Synchrotron Radiat* **22**, 577-583, doi:10.1107/s1600577515005317 (2015).

155 Foucar, L. *et al.* CASS-CFEL-ASG software suite. *Comput Phys Commun* **183**, 2207-2213 (2012).

156 White, T. A. *et al.* CrystFEL: a software suite for snapshot serial crystallography. *J. Appl. Crystallogr.* **45**, 335-341 (2012).

157 Ursby, T. & Bourgeois, D. Improved estimation of structure-factor difference amplitudes from poorly accurate data. *Acta Crystallogr A* **53**, 564-575 (1997).

158 Genick, U. K. Structure-factor extrapolation using the scalar approximation: theory, applications and limitations. *Acta Cryst. D* **63**, 1029-1041 (2007).

159 Genick, U. K. *et al.* Structure of a protein photocycle intermediate by millisecond time-resolved crystallography. *Science* **275**, 1471-1475 (1997).

160 Adams, P. D. *et al.* PHENIX: a comprehensive Python-based system for macromolecular structure solution. *Acta Cryst. D* **66**, 213-221 (2010).

161 Afonine, P. V., Headd, J. J., Terwilliger, T. & Adams, P. D. New tool: phenix.real_space_refine. *Computational Crystallography Newsletter* **4**, 43-44 (2013).

162 Emsley, P. & Cowtan, K. *Coot*: model-building tools for molecular graphics. *Acta Cryst. D* **60**, 2126-2132 (2004).

163 Stensitzki, T., Muders, V., Heberle, J., Schlesinger, R. & Heyne, K. The primary photoreaction of channelrhodopsin-1: wavelength dependent photoreactions induced by ground-state heterogeneity. *Front Mol Biosci* **2**, 41 (2015).

164 Fromme, R. *et al.* Serial femtosecond crystallography of soluble proteins in lipidic cubic phase. *IUCrJ* **2**, 545-551, doi:10.1107/s2052252515013160 (2015).

165 Cherezov, V., Fersi, H. & Caffrey, M. Crystallization screens: compatibility with the lipidic cubic phase for in meso crystallization of membrane proteins. *Biophys J* **81**, 225-242, doi:10.1016/S0006-3495(01)75694-9 (2001).

166 Kang, Y. *et al.* Crystal structure of rhodopsin bound to arrestin by femtosecond X-ray laser. *Nature* **523**, 561-567, doi:10.1038/nature14656 (2015).

167 Zhang, H. *et al.* Structure of the Angiotensin Receptor Revealed by Serial Femtosecond Crystallography. *Cell* **161**, 833-844, doi:10.1016/j.cell.2015.04.011 (2015).

168 Zhang, H. *et al.* Structural basis for selectivity and diversity in angiotensin II receptors. *Nature* **544**, 327-332, doi:10.1038/nature22035 (2017).

169 Zhang, H. *et al.* Structure of the full-length glucagon class B G-protein-coupled receptor. *Nature* **546**, 259-264, doi:10.1038/nature22363 (2017).

170 Sugahara, M. *et al.* Hydroxyethyl cellulose matrix applied to serial crystallography. *Sci. Rep.* **7**, doi:10.1038/s41598-017-00761-0 (2017).

171 Yamashita, K. *et al.* An isomorphous replacement method for efficient de novo phasing for serial femtosecond crystallography. *Sci. Rep.* **5**, doi:10.1038/srep14017 (2015).

172 Colletier, J. P. *et al.* Serial Femtosecond Crystallography and Ultrafast Absorption Spectroscopy of the Photoswitchable Fluorescent Protein IrisFP. *J Phys Chem Lett* **7**, 882-887, doi:10.1021/acs.jpclett.5b02789 (2016).

173 Fukuda, Y. *et al.* Redox-coupled proton transfer mechanism in nitrite reductase revealed by femtosecond crystallography (vol 113, pg 2928, 2016). *Proc. Natl. Acad. Sci. USA* **113**, E2207-E2207, doi:10.1073/pnas.1604061113 (2016).

174 Edlund, P. *et al.* The room temperature crystal structure of a bacterial phytochrome determined by serial femtosecond crystallography. *Sci. Rep.* **6**, doi:10.1038/srep35279 (2016).

175 Sugiyama, S. *et al.* A Novel Approach for Protein Crystallization by a Synthetic Hydrogel with Thermoreversible Gelation Polymer. *Cryst. Growth Des.* **13**, 1899-1904, doi:10.1021/cg301588b (2013).

176 Schmolka, I. R. Artificial Skin 1. Preparation and properties of Pluronic F-127 Gels for Treatment of Burns. *J Biomed Mater Res* **6**, 571-&, doi:10.1002/jbm.820060609 (1972).

177 Cespi, M., Bonacucina, G., Casettari, L., Mencarelli, G. & Palmieri, G. F. Poloxamer Thermogel Systems as Medium for Crystallization. *J Pharm Res* **29**, 818-826, doi:10.1007/s11095-011-0606-3 (2012).

178 Escobar-Chavez, J. J. *et al.* Applications of thermoreversible pluronic F-127 gels in pharmaceutical formulations. *J. Pharm. Pharm. Sci.* **9**, 339-358 (2006).

179 Hollabaugh, C. B., Burt, L. H. & Walsh, A. P. Carboxymethylcellulose - uses and applications. *Ind. Eng. Chem.* **37**, 943-947, doi:10.1021/ie50430a015 (1945).

180 Saha, D. & Bhattacharya, S. Hydrocolloids as thickening and gelling agents in food: a critical review. *J Fooc Sci Tech Mys* **47**, 587-597, doi:10.1007/s13197-010-0162-6 (2010).

181 Nogly, P. *et al.* Retinal isomerization in bacteriorhodopsin captured by a femtosecond x-ray laser. *Science* **361**, 145-+ (2018).

182 Luecke, H., Schobert, B., Richter, H. T., Cartailler, J. P. & Lanyi, J. K. Structure of bacteriorhodopsin at 1.55 angstrom resolution. *J. Mol. Biol* **291**, 899-911, doi:10.1006/jmbi.1999.3027 (1999).

183 Lanyi, J. K. Proton transfers in the bacteriorhodopsin photocycle. *Biochim Biophys Acta* **1757**, 1012-1018 (2006).

184 Bayly, J. G., Kartha, V. B. & Stevens, W. H. The absorption spectra of liquid phase H2O, HDO and D2O from 0.7 μM to 10 μM. *Infrared Physics* **3**, 211-222, doi:10.1016/0020-0891(63)90026-5 (1963).

185 Yi, A., Mamaeva, N., Li, H., Spudich, J. L. & Rothschild, K. J. Resonance Raman Study of an Anion Channelrhodopsin: Effects of Mutations near the Retinylidene Schiff Base. *Biochemistry* **55**, 2371-2380, doi:10.1021/acs.biochem.6b00104 (2016).

186 Coquelle, N. *et al.* Chromophore twisting in the excited state of a photoswitchable fluorescent protein captured by time-resolved serial femtosecond crystallography. *Nat Chem* **10**, 31-37 (2018).

187 Arnlund, D. *et al.* Visualizing a protein quake with time-resolved X-ray scattering at a free-electron laser. *Nat Methods* **11**, 923-926 (2014).

188 Prokhorenko, V. I., Halpin, A., Johnson, P. J. M., Miller, R. J. D. & Brown, L. S. Coherent control of the isomerization of retinal in bacteriorhodopsin in the high intensity regime. *J Chem Phys* **134** (2011).

189 Kraack, J. P., Buckup, T. & Motzkus, M. Resonant two-photon excitation pathways during retinal-isomerization in bacteriorhodopsin. *EPJ Web of Conferences* **41**, 07019 (2013).

190 Schmidt, B. *et al.* Excited-state dynamics of bacteriorhodopsin probed by broadband femtosecond fluorescence spectroscopy. *BBA-Bioenergetics* **1706**, 165-173 (2005).

191 Leonard, J., Sharma, D., Szafarowicz, B., Torgasin, K. & Haacke, S. Formation dynamics and nature of tryptophan's primary photoproduct in aqueous solution. *Phys Chem Chem Phys* **12**, 15744-15750, doi:10.1039/c0cp00615g (2010).

192 Polland, H. J., Franz, M. A., Zinth, W., Kaiser, W. & Oesterhelt, D. Energy-Transfer from Retinal to Amino-Acids - a Time-Resolved Study of the Ultraviolet Emission of Bacteriorhodopsin. *Biochim Biophys Acta* **851**, 407-415, doi: (1986).

193 Zhong, Q. *et al.* Reexamining the Primary Light-Induced Events in Bacteriorhodopsin Using a Synthetic C13C14-Locked Chromophore. *J. Am. Chem. Soc.* **118**, 12828-12829, doi:10.1021/ja961058+ (1996).

194 Ye, T. *et al.* Resolving the primary dynamics of bacteriorhodopsin, and of a 'C-13=C-14 locked' analog, in the reactive excited state. *Chem Phys Lett* **314**, 429-434 (1999).

195 Kahan, A., Nahmias, O., Friedman, N., Sheves, M. & Ruhman, S. Following photoinduced dynamics in bacteriorhodopsin with 7-fs impulsive vibrational spectroscopy. *J Am Chem Soc* **129**, 537-546 (2007).

196 Johnson, P. J. M. *et al.* The photocycle and ultrafast vibrational dynamics of bacteriorhodopsin in lipid nanodiscs. *Phys. Chem. Chem. Phys.* **16**, 21310-21320, doi:10.1039/c4cp01826e (2014).

197 Song, L., El-Sayed, M. A. & Lanyi, J. K. Protein catalysis of the retinal subpicosecond photoisomerization in the primary process of bacteriorhodopsin photosynthesis. *Science* **261**, 891-894 (1993).

198 Schenkl, S. *et al.* Insights into excited-state and isomerization dynamics of bacteriorhodopsin from ultrafast transient UV absorption. *Proc Nat Acad Sci USA* **103**, 4101-4106, doi:10.1073/pnas.0506303103 (2006).

199 Liu, R. S. H. Photoisomerization by Hula-Twist: A Fundamental Supramolecular Photochemical Reaction. *Acc. Chem. Res.* **34**, 555-562, doi:10.1021/ar000165c (2001).

200 Warshel, A. Bicycle-pedal model for the first step in the vision process. *Nature* **260**, 679, doi:10.1038/260679a0 (1976).

201 Szymczak, J. J., Barbatti, M. & Lischka, H. Is the Photoinduced Isomerization in Retinal Protonated Schiff Bases a Single- or Double-Torsional Process? *J. Phys. Chem. A* **113**, 11907-11918, doi:10.1021/jp903329j (2009).

202 Florean, A. C. *et al.* Control of retinal isomerization in bacteriorhodopsin in the high-intensity regime. *Proc Nat Acad Sci USA* **106**, 10896-10900 (2009).

203 Choe, H.-W. *et al.* Crystal structure of metarhodopsin II. *Nature* **471**, 651, doi:10.1038/nature09789 (2011).

204 Shibata, M. & Kandori, H. FTIR Studies of Internal Water Molecules in the Schiff Base Region of Bacteriorhodopsin. *Biochemistry* **44**, 7406-7413, doi:10.1021/bi050122+ (2005).

205 Govorunova, E. G., Sineshchekov, O. A., Li, H. & Spudich, J. L. Microbial Rhodopsins: Diversity, Mechanisms, and Optogenetic Applications. *Annu Rev Biochem* **86**, 845-872, doi:10.1146/annurev-biochem-101910-144233 (2017).

206 Mukohata, Y., Ihara, K., Uegaki, K., Miyashita, Y. & Sugiyama, Y. Australian Halobacteria and Their Retinal-Protein Ion Pumps. *Photochem Photobiol* **54**, 1039-1045 (1991).

207 Inoue, K. *et al.* A light-driven sodium ion pump in marine bacteria. *Nat. Commun.* **4** (2013).

208 Yoshizawa, S. *et al.* Functional characterization of flavobacteria rhodopsins reveals a unique class of light-driven chloride pump in bacteria. *Proc. Natl. Acad. Sci. USA* **111**, 6732-6737, doi:10.1073/pnas.1403051111 (2014).

209 Harris, A. *et al.* Molecular details of the unique mechanism of chloride transport by a cyanobacterial rhodopsin. *Phys. Chem. Chem. Phys.* **20**, 3184-3199, doi:10.1039/C7CP06068H (2018).

210 Agmon, N. The Grotthuss mechanism. *Chem. Phys. Lett.* **244**, 456-462, doi:doi.org/10.1016/0009-2614(95)00905-J (1995).

211 Sasaki, J. *et al.* Conversion of bacteriorhodopsin into a chloride ion pump. *Science* **269**, 73-75, doi:10.1126/science.7604281 (1995).

212 Tittor, J. *et al.* Chloride and proton transport in bacteriorhodopsin mutant D85T: different modes of ion translocation in a retinal protein. *J Mol Biol* **271**, 405-416, doi:10.1006/jmbi.1997.1204 (1997).

213 Kolbe, M., Besir, H., Essen, L. O. & Oesterhelt, D. Structure of the light-driven chloride pump halorhodopsin at 1.8 angstrom resolution. *Science* **288**, 1390-1396, doi:10.1126/science.288.5470.1390 (2000).

214 Gushchin, I. *et al.* Crystal structure of a light-driven sodium pump. *Nat Struct Mol Biol* **22**, 390, doi:10.1038/nsmb.3002 (2015).

215 Kato, H. E. *et al.* Structural basis for Na+ transport mechanism by a light-driven Na+ pump. *Nature* **521**, 48, doi:10.1038/nature14322 (2015).

216 Varo, G. Analogies between halorhodopsin and bacteriorhodopsin. *Biochim Biophys Acta* **1460**, 220-229, doi:10.1016/s0005-2728(00)00141-9 (2000).

217 Spudich, J. L. & Bogomolni, R. A. Mechanism of colour discrimination by a bacterial sensory rhodopsin. *Nature* **312**, 509, doi:10.1038/312509a0 (1984).

218 Spudich, J. L. & Luecke, H. Sensory rhodopsin II: functional insights from structure. *Curr Opin Struct Biol* **12**, 540-546, doi:10.1016/s0959-440x(02)00359-7 (2002).

219 Kim, S. Y., Yoon, S. R., Han, S., Yun, Y. & Jung, K.-H. A role of Anabaena sensory rhodopsin transducer (ASRT) in photosensory transduction. *Mol. Microbiol* **93**, 403-414, doi:doi:10.1111/mmi.12635 (2014).

220 Kateriya, S., Nagel, G., Bamberg, E. & Hegemann, P. "Vision" in Single-Celled Algae. *Physiology* **19**, 133-137, doi:10.1152/nips.01517.2004 (2004).

221 Saranak, J. & Foster, K. W. Rhodopsin guides fungal phototaxis. *Nature* **387**, 465, doi:10.1038/387465a0 (1997).

222 Avelar, Gabriela M. *et al.* A Rhodopsin-Guanylyl Cyclase Gene Fusion Functions in Visual Perception in a Fungus. *Curr Biol* **24**, 1234-1240, doi:10.1016/j.cub.2014.04.009 (2014).

223 Yoshida, K., Tsunoda, S. P., Brown, L. S. & Kandori, H. A unique choanoflagellate enzyme rhodopsin exhibits light-dependent cyclic nucleotide phosphodiesterase activity. *J. Biol. Chem.* **292**, 7531-7541, doi:10.1074/jbc.M117.775569 (2017).

224 Famintzin, A. Die Wirkung des Lichtes auf Algen. *Jb wiss Bot* **6**, 1-44 (1867).

225 Foster, K. W. *et al.* A rhodopsin is the functional photoreceptor for phototaxis in the unicellular eukaryote Chlamydomonas. *Nature* **311**, 756, doi:10.1038/311756a0 (1984).

226 Braun, F.-J. & Hegemann, P. Two Light-Activated Conductances in the Eye of the Green Alga Volvox carteri. *Biophys J* **76**, 1668-1678, doi:10.1016/S0006-3495(99)77326-1 (1999).

227 Harz, H. & Hegemann, P. Rhodopsin-regulated calcium currents in Chlamydomonas. *Nature* **351**, 489, doi:10.1038/351489a0 (1991).

228 Sineshchekov, O. A., Jung, K.-H. & Spudich, J. L. Two rhodopsins mediate phototaxis to low- and high-intensity light in Chlamydomonas reinhardtii. *Proc Natl Acad Sci USA* **99**, 8689-8694, doi:10.1073/pnas.122243399 (2002).

229 Sineshchekov, O. A., Govorunova, E. G. & Spudich, J. L. Photosensory Functions of Channelrhodopsins in Native Algal Cells†. *Photochem. Photobiol.* **85**, 556-563, doi:doi:10.1111/j.1751-1097.2008.00524.x (2009).

230 Kato, H. E. *et al.* Crystal structure of the channelrhodopsin light-gated cation channel. *Nature* **482**, 369, doi:10.1038/nature10870 (2012).

231 Inaguma, A. *et al.* Chimeras of Channelrhodopsin-1 and -2 from Chlamydomonas reinhardtii Exhibit Distinctive Light-induced Structural Changes from Channelrhodopsin-2. *J Biol Chem* **290**, 11623-11634, doi:10.1074/jbc.M115.642256 (2015).

232 Volkov, O. *et al.* Structural insights into ion conduction by channelrhodopsin 2. *Science* **358**, 1018-+, doi:10.1126/science.aan8862 (2017).

233 Kuhne, J. *et al.* Early Formation of the Ion-Conducting Pore in Channelrhodopsin-2. *Angew. Chem. Int. Ed.* **54**, 4953-4957, doi:doi:10.1002/anie.201410180 (2015).

234 Lórenz-Fonfría, V. A. *et al.* Transient protonation changes in channelrhodopsin-2 and their relevance to channel gating. *Proc Natl Acad Sci USA* **110**, E1273-E1281, doi:10.1073/pnas.1219502110 (2013).

235 Krause, N., Engelhard, C., Heberle, J., Schlesinger, R. & Bittl, R. Structural differences between the closed and open states of channelrhodopsin-2 as observed by EPR spectroscopy. *FEBS Lett* **587**, 3309-3313, doi:10.1016/j.febslet.2013.08.043 (2013).

236 Sattig, T., Rickert, C., Bamberg, E., Steinhoff, H.-J. & Bamann, C. Light-Induced Movement of the Transmembrane Helix B in Channelrhodopsin-2. *Angew. Chem. Int. Ed.* **52**, 9705-9708, doi:doi:10.1002/anie.201301698 (2013).

237 Müller, M., Bamann, C., Bamberg, E. & Kühlbrandt, W. Light-Induced Helix Movements in Channelrhodopsin-2. *J Mol Biol* **427**, 341-349, doi:10.1016/j.jmb.2014.11.004 (2015).

238 Resler, T., Schultz, B.-J., Lórenz-Fonfría, Víctor A., Schlesinger, R. & Heberle, J. Kinetic and Vibrational Isotope Effects of Proton Transfer Reactions in Channelrhodopsin-2. *Biophys J* **109**, 287-297, doi:10.1016/j.bpj.2015.06.023 (2015).

239 Gerwert, K. Channelrhodopsin reveals its dark secrets. *Science* **358**, 1000-1001, doi:10.1126/science.aar2299 (2017).

240 Wietek, J. *et al.* Conversion of Channelrhodopsin into a Light-Gated Chloride Channel. *Science* **344**, 409-412, doi:10.1126/science.1249375 (2014).

241 Keeling, P. J. *et al.* The Marine Microbial Eukaryote Transcriptome Sequencing Project (MMETSP): Illuminating the Functional Diversity of Eukaryotic Life in the Oceans through Transcriptome Sequencing. *PLOS Biology* **12**, e1001889, doi:10.1371/journal.pbio.1001889 (2014).

242 Matasci, N. *et al.* Data access for the 1,000 Plants (1KP) project. *GigaScience* **3**, 2047-2217X-2043-2017-2047-2217X-2043-2017, doi:10.1186/2047-217X-3-17 (2014).

243 Lórenz-Fonfría, V. A. & Heberle, J. Channelrhodopsin unchained: Structure and mechanism of a light-gated cation channel. *Biochim Biophys Acta* **1837**, 626-642, doi:10.1016/j.bbabio.2013.10.014 (2014).

244 Varo, G. *et al.* Photocycle of Halorhodopsin from *Halobacterium salinarum Biophys. J* **68**, 2062-2072 (1995).

245 Gmelin, W. *et al.* The crystal structure of the L1 intermediate of halorhodopsin at 1.9 angstrom resolution. *Photochem. Photobiol.* **83**, 369-377, doi:10.1562/2006-06-23-ra-947 (2007).

246 Schreiner, M., Schlesinger, R., Heberle, J. & Niemann, H. H. Structure of Halorhodopsin from Halobacterium salinarum in a new crystal form that imposes little restraint on the E-F loop. *J. Struct. Biol.* **190**, 373-378, doi:10.1016/j.jsb.2015.04.010 (2015).

247 Kabsch, W. XDS. *Acta Cryst D* **66**, 125-132, doi:10.1107/S0907444909047337 (2010).

248 McCoy, A. J. *et al.* Phaser crystallographic software. *J Appl Crystallogr* **40**, 658-674, doi:doi:10.1107/S0021889807021206 (2007).

249 Winn, M. D. *et al.* Overview of the CCP4 suite and current developments. *Acta Cryst. D* **67**, 235-242 (2011).

250 Murshudov, G. N., Vagin, A. A. & Dodson, E. J. Refinement of Macromolecular Structures by the Maximum-Likelihood Method. *Acta Cryst D* **53**, 240-255, doi:doi:10.1107/S0907444996012255 (1997).

251 Takeda, K. *et al.* A novel three-dimensional crystal of bacteriorhodopsin obtained by successive fusion of the vesicular assemblies11Edited by K. Nagai. *J Mol Biol* **283**, 463-474, doi:10.1006/jmbi.1998.2103 (1998).

6. Appendix

6.1. Microbial rhodopsins

There are over 7000 microbial rhodopsins and their biological function is either light-driven ion pumping that helps maintaining the membrane potential and thus contributes to energy formation or sensory reception in order to use light as environmental information for regulating intracellular processes[205].

Ion-pumping microbial rhodopsins

Among these rhodopsins are **outward proton pumps** first found in *Archaea*, such as archaeal bacteriorhodopsin (bR)[5] and archaerhodopsins 1-3[206], but also present in marine bacteria (proteobacterial proteorhodopsin[16] and flavobacterial KR1[207]), fungi and algae; or **inward chloride pumps** such as archaeal halorhodopsin (hR)[6,7], flavobacterial ClR[208] and cyanobacterial MastR[209], or a bacterial **outward sodium ion pumps** NaR (i.e. flavobacterial KR2[207]). All microbial rhodopsins contain protein-bound water molecules in the vicinity of the PSB, which are likely needed for its stabilization but also for the protein function.[17] The relationship between the structure and molecule to be transported is fairly well established – archaeal proton pumps use aspartic residues as proton acceptors and donors (D85 and D96 in bR) with respect to the retinal PSB. D85 and D96 together with a highly conserved residue R82 form a counterion complex that balances the positive charge on the PSB, thus an electrostatically stabilized quadrupole is created (Figure 34a), which is then perturbed during the photocycle causing a proton shuttle to the extracellular, possibly in a Grotthuss-like mechanism[54,210] (concerted proton "hopping" in a water chain). The electrostatic quadrupole is characteristic of most microbial rhodopsins and the sequence motif is largely conserved in marine bacterial proton pumps, but changes in sodium and chloride pumps.[17] In case of chloride pumps, uncharged amino acids (asparagine and threonine in marine and archaeal pumps, respectively) replace aspartate and the positive charge on the PSB is thus neutralized by the nearby bound chloride, which is then translocated to the cytoplasma (in line with that, the D85T bR mutant is a chloride pump[211,212]). Consequently, there is no deprotonation of the PSB and both the proton donor and acceptor are replaced, in case of hR by alanine (A122) and threonine (T111), respectively (Figure 34b).[213] Based on the crystal structures of KR2, the likely mechanism of sodium pumping is that during the photocycle, the proton acceptor D116 reorients as it accepts a proton from PSB, and Na^+ passes around the neutral Schiff base to the extracellular (Figure 34c).[214,215] Notably, the sodium ion is not near the PSB,

but binding near the cytoplasmic site, explaining no change of the KR2 absorption spectrum in the absence or presence of sodium ions.[207,214,215]

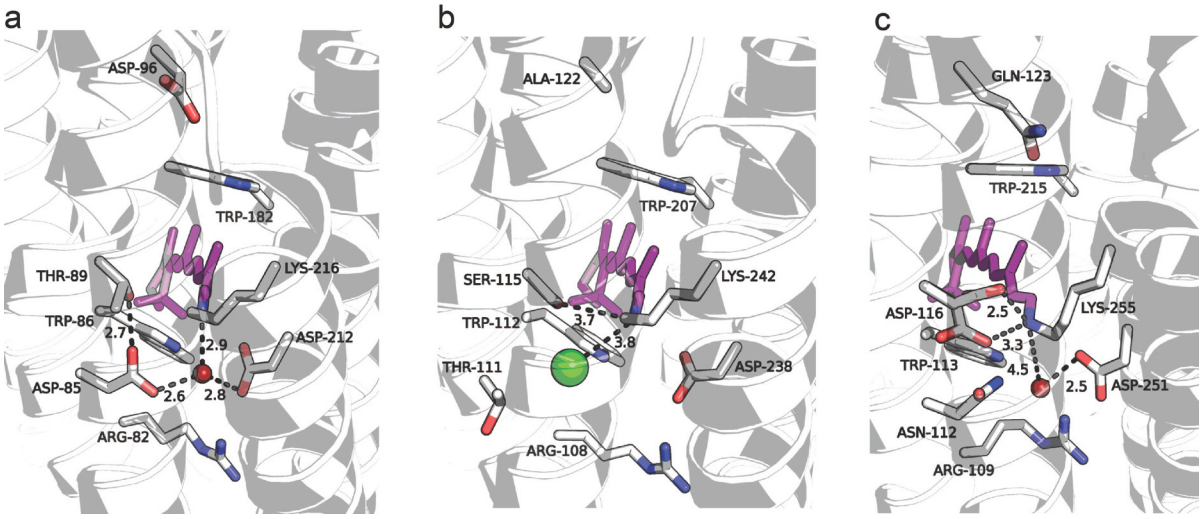

Figure 34. Ion-pumping rhodopsins. Residues important for the ion specificity and function as well as highly conserved tryptophanes are shown as grey sticks. Retinal is shown as purple sticks. The red spheres are waters. **a**, Bacteriorhodopsin (PDB 1C3W)[182] as an example of a proton pump having the motif DTD (Asp85, Thr89, Asp96), where Asp85 and Asp96 are the proton acceptors and donor, resp., and Thr89 contributes to stabilization of the PSB together with water 402, Asp85 and Asp96. The quandrupole is formed by PSB, Asp85, Arg82 and Asp96. **b**, Halorhodopsin (PDB 1E12)[213] is an inward chloride pump with the motif TSA (Thr111, Ser115, Ala122). The proton acceptor is replaced by Thr111 and the proton donor by Ala122 – the PSB does not deprotonate in hR.[216] The missing negative charge of Asp85 is compensated by chloride (green sphere). **c**, KR2 (PDB 3X3C)[215] as an example of an outward sodium pump with the motif NDQ (Asn112, Asp116, Gln123). The putative proton acceptor, Asp116, directly stabilizing the PSB, was modelled in two conformations at the neutral pH used for crystallization, supposedly mimicking the ground state structure closer to the PSB and the downshifted protonated conformation (acidic conditions produced only the downshifted conformation).[215]

Microbial rhodopsins with a sensory function

These microbial rhodopsins have diverse signalling mechanisms, yet they share photochemical features such as long-lived stable signalling states that are not present in ion pumps rhodopsins.[205] The first identified microbial light-sensing receptor was a phototaxis receptor **sensory rhodopsin** I (SRI) found in *Archaea*.[8,9] Whereas 1-photon excitation with orange light guides the microorganism towards higher light intensities, a second photon (near UV) absorbed by the long-lived photointermediate at 373 nm causes light-avoidance.[217] In addition, a second signalling photoreceptor is present, sensory rhodopsin II (SRII), which causes negative phototaxis in response to blue light.[10,11] SRI and SRII are part of a 2:2 protein complex formed with the transmembrane transducers HtrI and HtrII, respectively, to which the light-induced helix motion is transmitted via helix-helix contacts. Htr's cytoplasmic domain controls the activity of a bound histidine kinase, thus modulating the cell's motility apparatus.[218] In contrast to that, a cyanobacterial sensory rhodopsin, *Anabaena* sensory

rhodopsin (ASR), interacts with a soluble transducer (ASRT). A unique property of ASR is bistable switching between all-*trans* and 13-*cis* retinal depending on the light wavelength. While the function of the ASTR-ASRT complex is not yet completely understood, studies indicate that the complex regulates expression of some of the genes encoding of the phycobilisome and controls the circadian clock.[219]

Microbial rhodopsins also exist as multidomain proteins, where the N-terminal rhodopsin domain is followed by diverse cytoplasmic C-terminal domains, some of which are of known enzymatic functions[205]. These **enzymerhodopsins** were found in several algae and fungi genomes. Here, the rhodopsin domain is followed by domains homologous to histidine kinases, response regulators and guanylyl or adenylyl cyclases (histidine kinase rhodopsins from green algae[220]) or it is directly followed by a guanylyl cyclase (fungal guanylyl cyclase rhodopsins[221,222]) or a phosphodiesterase domain (found in flagellate eukaryotes).[223]

Currently the largest family of microbial rhodopsins equipped with a sensory function is that of **channelrhodopsins,** having a bulky cytoplasmic C-terminal extension of unknown function.[205] While light-induced alterations of swimming behaviour of microalgae were described already in 1867,[224] it was not until 1984 that K.W. Foster experimentally proved that the responsible photoreceptor is a rhodopsin, which he achieved by restoring light sensing in blind *Chlamydomonas reinhardii* alga by complementation with retinal.[225] Based on recorded photocurrents, a function in both positive and negative phototaxis was proposed and given the extremely fast rise time of the currents, a close link of the photoreceptor to an ion channel was proposed.[226,227] This was confirmed once the DNA sequences were identified and the protein could be obtained[13,228] (isolation from native source was not successful). Electrophysiological recordings further specified that these pigments, **cation channelrhodopsin** I and II (CCR), are light-gated proton and sodium ion channels, resp.[12,13] In native algal cells, the photocurrent has two components, where the fast (early) one observed at high light intensities is directly linked to CCRs activity. The major contribution to the membrane depolarization however comes from the slow (late) component arising at 1000 × lower light intensities, predominantly originating from CCR2 activating secondary Ca^{2+} channels by a yet unknown mechanism.[205,229] Wild-type CCRs have been resistant to structure determination via X-ray crystallography for a long time and until recently, only the structure of a C1C2 chimera was available,[230] which had different spectroscopic signatures when compared to *C.reinhardii* CCR2 (*Cr*ChR2).[231] In 2017, the structure of *Cr*ChR2 was the first membrane protein structure obtained from the expression host *Leishmania tarentolae*.[232] Here, in contrast to archaeal proton pumps, the PSB is directly hydrogen-bonded to counterions Glu123 and Asp253 (homologous to Asp85 and Asp212 in bR), without a water molecule in between (Wat402 in bR).[232] PSB, Asp253 and Glu90 and several other residues

form the central gate (CG) in the channel, which is dissected into four highly hydrophilic cavities by two additional gates (extracellular (ECG) and intracellular gate (ICG)). An extensive hydrogen-bond network containing residues and ordered water molecules connects the CG with the ECG, where the central residue is Arg120, a highly conserved residue critical for function in all microbial rhodopsins (Arg82 in bR).[232] From this, the following mechanism of channel opening emerges, which has been in part predicted by earlier computational and spectroscopic studies:[233,234] after retinal isomerization, the PSB donates a proton to Asp253 (rise of the M intermediate), whose rearrangements disturb the hydrogen-bond network extending to Arg120. This opens the CG and ECG, several residues of which are located in helix 2, whose reorientation unique for CCRs was observed in the open channel by electron paramagnetic resonance[235,236] and electron microscopy[237]. Together with motion of helix 6 and 7 typical for rhodopsins, the salt bridge (Arg268, Glu82, Glu83) in the ICG may break and the channel would be completely open.[232] Indirect reprotonation of PSB by Asp156, which is simultaneously the decay of the M intermediate, launches closing of the channel[234,238], thus analogously to bR the de- and reprotonation of PSB would control ion translocation[239]. Glu90 is known to control the ion selectivity, as a mutation to a positively charged residue turns *Cr*ChR2 into a slow chloride channel.[240]

Light-gated anion channels have not been known until recently, when model proteins with sequences similar to CCRs were identified in the nuclear genome data of *Guillardia theta*, the only fully sequenced cryptophyte so far.[14] It turned out that these **anion channelrhodopsins** (ACRs) *Gt*ACR1 and *Gt*ACR2 conduct strictly anions when heterologously overexpressed and the photocurrents generated are greater than from *Cr*ChR2, with a unity conductance 25-fold higher.[14] Ongoing transcriptome sequencing projects revealed about 20 other ACRs from various cryptophyte algae.[205,241,242] Similarly to marine and archaeal chloride pumps, a noncarboxylic residue occupies the position analogous to the primary proton acceptor in bR. Both Glu90 and Asp258 in CCRs are preserved in ACRs. This is surprising in case of Glu90, which is known to determine the cation selectivity in CCRs. Not only is a glutamate also present in ACRs (Glu68), its mutation to R does not affect the selectivity, but the gating – the channel is closed in the light and open in the dark state.[22] Clearly, the ion selectivity and gating in ACRs is different from that in CCRs. Further intriguing differences are in the link between the photocycle intermediates and channel opening and closing. Whereas in CCRs, deprotonation of PSB and thus M formation precedes opening of the channel, in ACRs it is already open in the preceding L-like intermediate[23]. In ACRs, M rise is strikingly slower (~1000 ×) than in CCRs and the rise and decay are associated with fast and slow channel closing, resp.[23,243] Interestingly, the absorption spectrum of ACR is not altered in the absence of chloride ions as it is in the case of hR, suggesting that a chloride ion is not surrounding the

PSB and Glu68 may act as a counterion instead.[23,205] All taken together, ACR present a functionally distinct family of microbial rhodopsins.

6.2. Ion translocation in halorhodopsin

6.2.1. Introduction and aim

The microbial rhodopsin halorhodopsin (hR) from the organism *H.salinarum* is a light-activated inward chloride pump which facilitates maintaining osmotic balance during phototrophic cell growth.[7] The light-induced steps occur during a photocycle containing multiple spectroscopically characterized intermediates (Figure 35).[244] In the ground state, the chloride ion is in the proximity of the PSB neutralizing its positive charge.[213] The aspartic residues essential for proton pumping in bR, the proton acceptor Asp85 and donor Asp96, are replaced by Thr111 and Ala122 in hR (Figure 34b), since in hR, the PSB does not deprotonate during the hR photocycle.[17] Like in bR, the photocycle is initiated by photon absorption (λ_{max}=578 nm), inducing the isomerization of all-*trans* retinal to 13-*cis* (K intermediate).[244] The structure of the following intermediate L1 was determined using crystals of the T203V hR mutant, which has a long lifetime of L, allowing to trap L1 at low temperatures.[245] This L1 crystal structure shows that the chloride ion moves by 0.3 Å towards to the PSB, which underwent rearrangement after retinal isomerization. As the chloride ion is still in the extracellular part of the protein, it implies that structural changes which allow the ion to bypass the retinal and make room for its exit to the cytosol occur later, presumably during the transition to L2.[245]

The aim of this project was to determine the structures of K and L intermediates in a time-resolved SFX experiment in order to observe the isomerized retinal and the subsequent structural changes enabling ion translocation. In this case, the advantages of SFX over synchrotron-based cryo-crystallography are the possibility (1) to avoid the use of mutants and observe intermediates in wild-type protein, (2) to perform data collection at physiologically relevant room temperature and (3) to be able to use easier-to-photoexcite microcrystals while mitigating the effects of radiation damage. In order to achieve this, the first milestone was to establish conditions for large-scale preparation of well-diffracting hR microcrystals, starting with initial protocols for purification and crystallization provided by collaborators from FU Berlin. The group of Dr. Ramona Schlesinger provided protocols and hR-rich membrane patches and the group of Prof. Joachim Heberle performed FTIR spectroscopy on the crystals to provide optimal time-delays for measurements of the specific intermediates in the TR-SFX experiment. The results of the TR-SFX experiment should provide clues about the mechanism of light-induced ion transport, which is more easily observed in a chloride pump as compared to a proton pump, since an ordered chloride ion can be well resolved in the electron density map. Besides a better understanding of light-energy conversion principles, it would also provide valuable insight for optogenetics, which uses microbial rhodopsin to control membrane potentials.

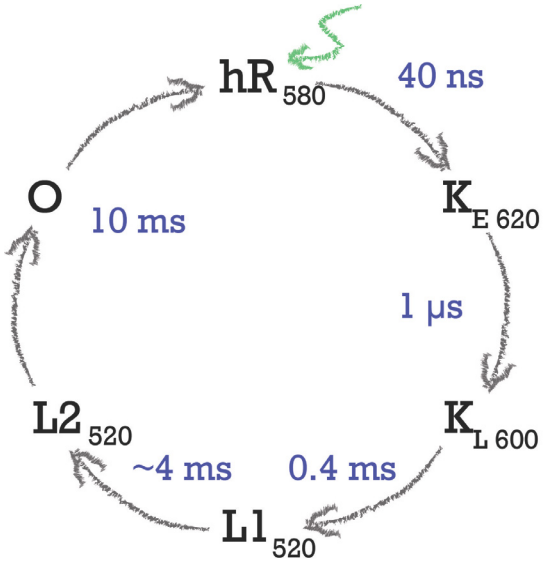

Figure 35. Halorhodopsin photocycle. The absorption of a green/yellow photon (green arrow) triggers a functional photocycle encompassing several intermediate states (letters K to O). Their rise times are written in blue and the subscript of the intermediate name refers to the maximum absorption wavelength. The time-constants were provided by Prof. Joachim Heberle.

6.2.2. Additional methods

6.2.2.1. Purification

hR from the *H.salinarum* bR-deficient (bop$^-$) L33 strain transformed with a bop promotor controlled vector encoding His-tagged *s*hR was expressed by Ramona Schlesinger's group (FU Berlin) and obtained as purified membrane patches.

A protocol for the purification was also provided by this group (Rieke Stock) and adapted with minor modifications. The purified membranes were pelleted by ultracentrifugation (50 000 rpm, rotor Ti70, 30 min, 4 °C) and resuspended in 50 mM MES pH 6.8, 4 M NaCl (buffer 1) with 2% DDM for solubilisation (gentle agitation, 2h, 4 °C). The insoluble fraction was pelleted by ultracentrifugation (50 000 rpm, rotor Ti70, 30 min, 4 °C) and the soluble fraction was supplemented with 5 mM imidazole and mixed with Ni^{2+}-NTA resin equilibrated with buffer 1 with 0.05% DDM. Binding was performed in batch (1 h) and subsequent steps were performed on the column. The column was washed with 5 column volumes (CVs) of buffer 1 with 5 mM imidazole, 0.05% DDM; 5 CVs of buffer 1 with 20 mM imidazole, 0.05% DDM and 5 CV of buffer 1 with 0.05% DDM. The protein was eluted with 50 mM MES pH 4.3, 4 M NaCl, 0.05 % DDM. The protein concentration was adjusted to 1 mg/mL and the sample was loaded onto a PD10 desalting columns (GE Healthcare, Uppsala, Sweden) equilibrated with 250 mM K_2HPO_4/ NaH_2PO_4 pH 7.4, 0.5 % OG (buffer 2). The protein was eluted with buffer 2 and concentrated to 30-50 mg/mL for crystallization with

100 kDa MWCO centrifugal filter units. Concentration was determined using the molar extinction coefficient ε= 50 000 M^{-1} cm^{-1} at 570 nm.

OG was either supplied by Anatrace (Anagrade or Sol-grade quality) or Glycon Biochemicals GmbH (purity >99.5% or 99 %).

6.2.2.2. Crystallization

In meso crystallization on the cover slip

A protocol for mixing monoolein and protein 1:2 on a cover slip with a spatula was provided by Rieke Stock (FU Berlin). The following adaptation yielded best crystals: on the cover-slip incorporated in the screw cap of a 24-well crystallization plate (Nextal Crystallization Tool) 14.1 mg molten monoolein was spread as a thin layer and overlaid with 28.2 µl protein (28 mg/mL) mixed with 1.5 µl of 5 M NaCl. After two weeks, the layer was topped up with additional 8.8 mg monoolein, 19.6 mg protein (15 mg/mL) and 1 µl 5 M NaCl and overlaid with ~15 µl 750 mM NaCl, 250 mM K/Na P_i pH 7.4. This dissolved all crystals that initially appeared. However, after one week, crystals reappeared in larger sizes and quantities.

In meso crystallization in Hamilton syringes

hR was reconstituted in LCP using monoolein (NuChek Prep) at a ratio 60:40 monoolein:protein and gas-tight Hamilton syringes (1710 or 1725 RN) connected with a coupler (TTP Labtech).[113] Commercial sparse matrix and self-made screens were set up in LCP sandwich plates (Marienfeld, Hampton Research) at 20°C as described.[112] Initial crystals appeared in crystallization conditions with 1-2 M KCl, 0-8% PEG 550 MME, pH 5-7. The final crystallization condition was 0.75 M KCl, 0.125 M K/Na P_i pH 5.8. Large-scale crystallization was performed in Hamilton syringes.[113] Typical crystals were 10-50 µm sized thin hexagonal purple plates.

For lipid-supplementation tests, polar lipids 1,2-diphytanoyl-sn-glycero-3-phosphocholine and 1,2-diphytanoyl-sn-glycero-3-phospho-(1'-rac-glycerol) were purchased from Avanti, Polar Lipids Inc. Monoolein was supplemented with 10% or 20% of each following the published procedure[112] and used for crystallization in the same manner.

Vapour-diffusion crystallization

Hanging-drop vapour-diffusion set-ups were made in 24-well Linbro plates at 293 K. Best crystals appeared in drops prepared by mixing 0.5 µl precipitant and 2 µl protein at 21-27 mg/mL. The precipitant contained 2.1-2.4 M ammonium sulfate, 100 mM bicine pH 8, 150 mM NaCl, based in the published condition.[246]

6.2.2.3. Synchrotron x-ray data collection and structure determination

Diffraction testing and collection of rotation datasets on single hR crystals at 100 K was carried out at the X10SA beamline at the Swiss Light Source (Villingen, Switzerland).The programs XDS, XSCALE and XDSCONV[247] were used for processing of complete hR data sets. The structure was determined by molecular replacement using PDB coordinates 1E12 and the program *Phaser*[248] from the CCP4 program suite.[249] *Refmac*[250] and *Coot*[162] were used for iterative rounds of model refinement.

6.2.3. Results and discussion

Several 40 – 50 µm large hR crystals were obtained by following the purification and "*in meso* crystallization on the cover slip protocol" provided by Rieke Stock with minor modifications (Figure 36a). These crystals diffracted to a high resolution of 1.6 Å at the synchrotron (crystallographic statistics are in Table 18), yielding a well-defined electron density (Figure 36b)and a structure in excellent agreement with the published high-resolution structures of hR.[213,245] In this crystallization protocol, the mesophase was exposed to air and thus largely dehydrated, transitioning from the non-birefringent LCP phase to a birefringent phase (likely the lamellar crystalline phase), which produces strong diffraction rings.[111] This is not critical for single-crystal data collection, where the crystal is "scooped out" with only residuals amounts of the mesophase attached. However, this is detrimental for a SFX experiment, where the surrounding mesophase constitutes the largest fraction of the exposed sample and the background rings can be so intense that they damage the detector. Therefore, the crystallization set-up needed to be modified such that the mesophase hydration level was controlled and stable, which can be achieved by performing the crystallization in gas-tight Hamilton syringes (Figure 9).[113]

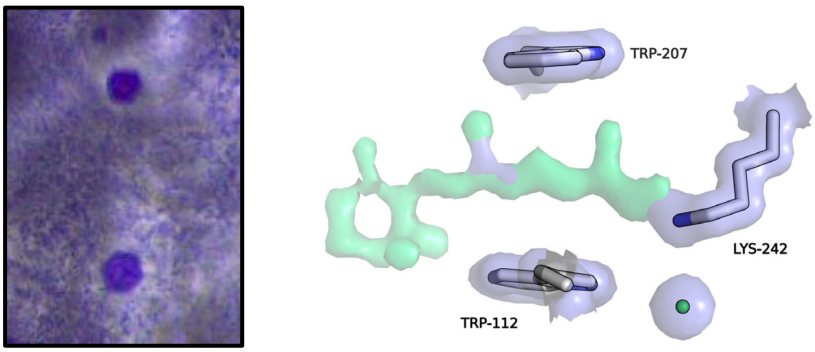

Figure 36. Single large hR crystal. a, The data was collected from bottom purple hexagonal crystal which is ~50 µm in diameter. **b**, The 1.6 Å electron density in the retinal binding pocket. A well-defined electron density for retinal (green) appeared even when retinal coordinates were removed from the model, indicating very good data quality. Slate surface shows the $2F_o$-F_c map contoured at 1σ, green surface shows F_o-F_c contoured at +3σ. The residues in the model are shown as white sticks and chloride ion is a green sphere.

Table 18. Crystallographic statistics.

Data collection	
Wavelength	0.992 Å
Space group	H32
Unit cell parameters [Å]	a,b= 93.5, c= 155.4; α,β= 90°, γ=120°
Resolution (highest shell) [Å]	50-1.6 (1.7-1.6)
Number of unique reflection	34654 (5728)
Completeness [%]	99.8 (99.9)
redundancy	5.5 (5.5)
R_{merge} [%]	5.0 (53.4)
I/σ	19.42 (3.6)
$CC_{1/2}$	100.0 (86.4)
Wilson B-factor [Å]	28.0

To transition to this new crystallization geometry, small-scale and high-throughput screening plates were set-up. A range of crystallization conditions yielding microcrystals was found and reproduced in Hamilton syringes once the protein concentration was increased up to 60 mg/mL, which was significantly higher than the typical range of 10-20 mg/mL used in LCP crystallization.[112] The optimized crystallization condition contained only 0.75 M KCl as compared to the initial 1.5 M, as this produced salt crystal diffraction rings when injected into the SFX vacuum chamber, which is again unacceptable for SFX data collection due to the risk of detector damage. The diffraction quality of these crystals was in the range of 3 – 6 Å at the synchrotron source and numerous optimization steps were tested (Figure 37a, Figure 38b). Some of these did not yield crystals at all (screening for different detergents, decreasing detergent concentrations in the buffers, supplementing monoolein with archeol-like polar lipids). In many cases, crystals appeared, but with no improvement in diffraction quality (different detergent purity and supplier). Supplementing the precipitant with PEG (17 % PEG 550 MME) in order to further dehydrate the crystals in the mesophase did also not increase the diffraction quality. Interestingly, crystals appeared more reproducibly when excess detergent was decreased by using higher molecular weight cut-off concentration units. On the other hand, indistinguishable crystals, yet with a decreased diffraction quality to ~ 8 Å, appeared when switching from small 10 mL gravity-flow desalting columns (PD10 Desalting columns, GE Healthcare) to a larger high-pressure driven 53 mL desalting column (HiPrep 26/10 Desalting column, GE Healthcare) with the aim of a larger-scale purification (Figure 37b, Figure 38a). It also remained unclear why some batches yielded crystals

diffracting to ~ 3 Å and others to 6 Å. The diffraction quality did not improve when the crystals were tested at the XFEL, indicating that the low quality was due to poor crystalline order and not due to other factors, such as manual crystal handling for synchrotron data collection or radiation damage. During the preparations for the XFEL experiment, Pluronic F-127 was identified as an injection additive that improved flow properties of the stream and the homogeneity of the sample. It was tested at the synchrotron source that Pluronic had no impact on the diffraction quality of hR crystals, moreover it prevented formation of ice-rings during flash-freezing of the single crystals (Figure 38c).

In parallel to the *in meso* crystallization, vesicle-fusion crystallization[251] was tested based on a published crystallization condition, which was reported to yield crystals diffracting to 2.2 Å.[246] In this protocol, a different protein purification protocol preceded the crystallization. The published procedure could not be reliably reproduced and yielded high amounts of precipitate, which would not be compatible with the SFX sample delivery. However, when vapour-diffusion crystallization drops were set-up with the protein purified using the same purification protocol as provided by Rieke Stock for the in meso crystallization, large quantities of microcrystals appeared reproducibly (Figure 37c). Unfortunately, these diffracted to ~25 Å when tested at the synchrotron source, therefore the in meso crystallization was preferred.

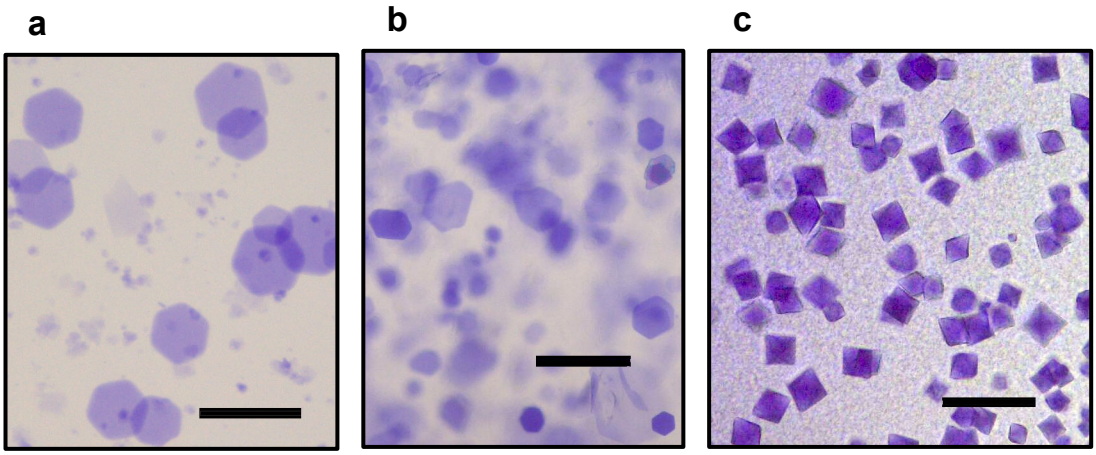

Figure 37. hR microcrystals obtained with different purification and crystallization protocols. The black bar represents 100 µm. **a,** Crystals grown in LCP obtained from protein purified using a small (**a**) and large (**b**) column for desalting diffracted to 3.5 Å and 8–9 Å, resp. **c,** Crystals grown in vapour diffusion set-ups diffracted to ~ 25 Å.

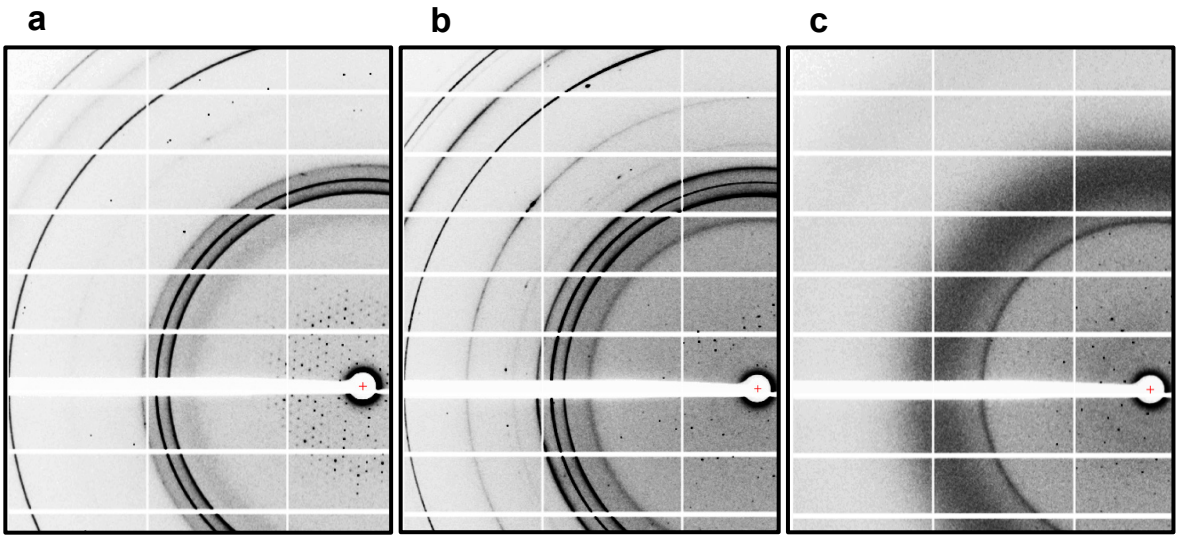

Figure 38. hR diffraction patterns collected at a synchrotron source. Crystals grown in LCP obtained from protein purified using a large and small column for desalting diffracted to 8 – 9 Å (**a**) and 3.5 Å (**b**), resp. **c,** Same crystal batch as in **b** was supplemented with Pluronic, resulting in the disappearance of sharp ice rings (visible in **b**).

While the exact cause of the irreproducible diffraction quality could not be identified, the most likely reason seems to be the variability in the protein:detergent:lipid composition of the sample. Only a very specific ratio of the mixed DDM:OG micelles promotes crystallization of hR. This implies that all buffer volumes used in the purification have to be kept strictly constant (e.g. volumes used for protein elution or any dilution) which impacts scaling-up to produce large amounts of protein needed for TR-SFX. Further, the amount of endogenous lipid bound to the protein will also affect the micelle composition, meaning that not only purification, but also protein expression and membrane preparation needs to be highly standardized. As part of the work was carried out by collaborators, it was impossible to control the reproducibility of each step.

In conclusion, this demonstrates that sample preparation is one of the major challenges in TR-SFX, in particular when shifting away from well-understood model systems to real samples. This is especially true for membrane proteins, which remain difficult targets. While one well-diffracting crystal is sufficient for a complete dataset at a synchrotron source, thousands of these are needed for a TR-SFX experiment. Therefore, thorough understanding and high reproducibility of the crystallization procedure is a pre-requisite in this case. Regular testing of crystal diffraction quality at the synchrotron prior to the XFEL experiment is essential.

6.3. Supplementary Figures

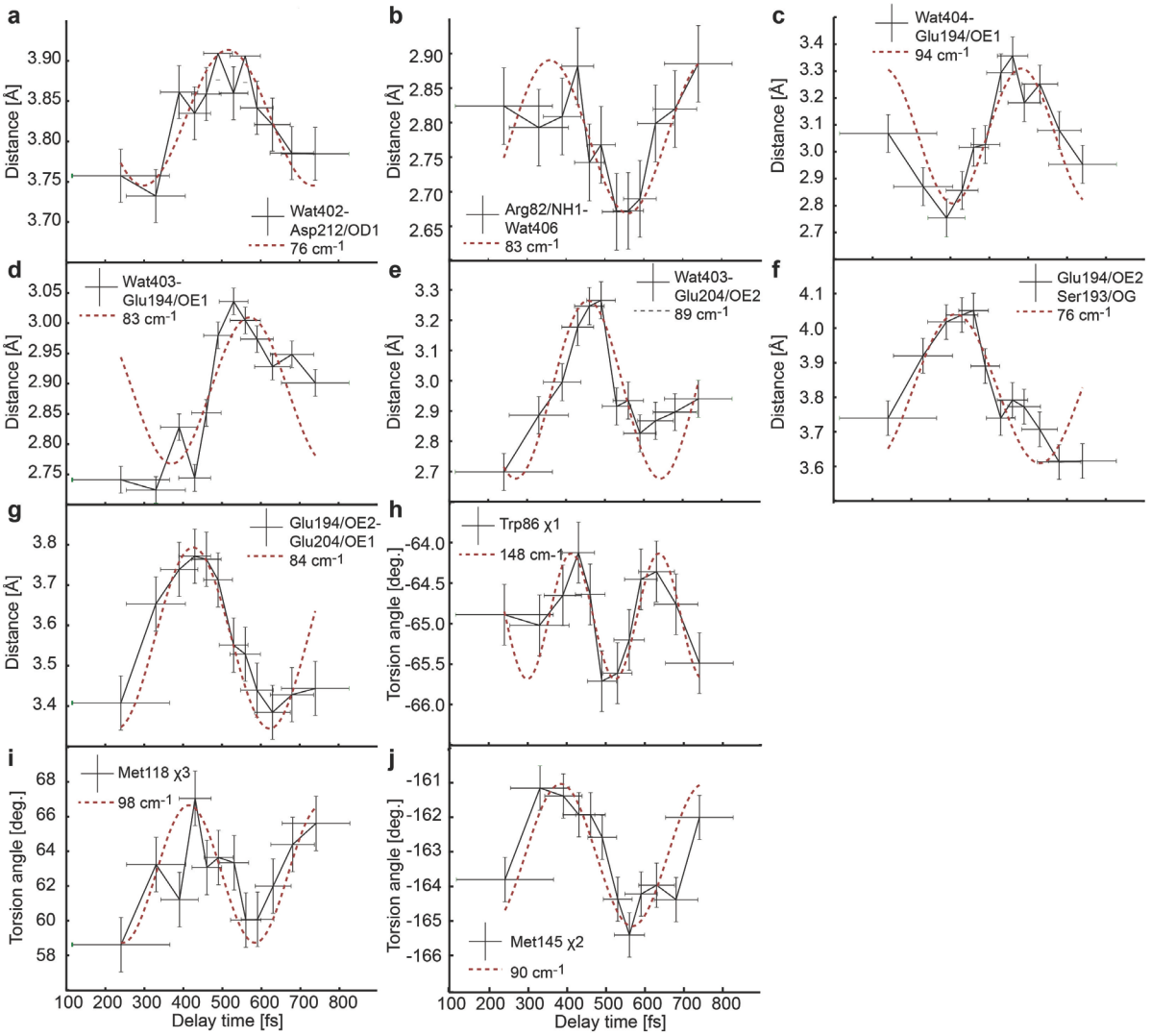

Supplementary Figure 1. Oscillatory modulations in the torsion angles of residues and their distances to other residues and water molecules. The error bars represent standard deviations. The dashed sinusoid shows the main frequency of the oscillation. **a**, The distance between the Asp212 oxygen OD1 and water Wat402 oscillates in time with a period of 76 cm^{-1} similarly to the oxygen OD2-Wat402 distance (80±9 cm^{-1},Figure 13e). **b**, The motion is likely propagated via the water network towards Arg82, whose nitrogen NH1 to water Wat406 distance oscillates with 83 cm^{-1}. **c-g**, Similar oscillatory modulation occur in the residues at the proton release site towards the extracellular. This includes in addition to Figure 13**f** distances between Glu194/OE1 and waters Wat404 (94 cm^{-1}, **c**) and Wat403 (83 cm^{-1}, **d**), between Glu204/OE2 and Wat403 (89 cm^{-1}, **e**) and Ser193/OG (76 cm^{-1}, **f**) and between Glue204/OE2 and Glu194/OE1 (84 cm^{-1}, **g**). **h-j**, Oscillations of torsion angles of residues lining the retinal pocket (in addition to Figure 13**g-i)** include Trp86 χ_1 (148 cm^{-1}, **h**), Met118 χ_3 (98 cm^{-1}, **i**) and Met145 χ_2 (90 cm^{-1}, **j**).

6.4. Abbreviations

ACR	Anion channelrhodopsin
*Ac*NPV	*Autographa californica* nuclear polyhedrosis virus
ASR	*Anabaena* sensory rhodopsin
ASRT	*Anabaena* sensory rhodopsin transducer
APS	Ammonium peroxydisulfate
AU	Absorption units
bR	bacteriorhodopsin
BSA	Bovine serum albumin
c	Concentration
CVs	Column volumes
CCR	Cation channelrhodopsin
CCW	Counter-clockwise
CW	clockwise
CXI	Coherent X-ray Imaging Instrument, endstation at LCLS
DDM	n-Dodecyl-β-D-Maltopyranoside
DM	Decyl maltoside
DTE	Dithioerythritol
DTT	Dithiothreitol
EDTA	Ethylenediaminetetraacetic acid
E. coli	*Escherichia coli*
ESA	Excited state absorption
FSEC	Fluorescence-detection size-exclusion chromatography
GBS	Ground state bleach
GDVN	Gas-dynamic virtual nozzle
GFP	Green fluorescent protein
GI	Glucose isomeraze
HEPES	4-(2-Hydroxyethyl)-1-piperazineethanesulfonic acid
HEWL	Hen egg-white lysozyme
HOMO	Highest occupied molecular orbital
HPLC	High performance liquid chromatography
hR	halorhodopsin

HVE	High viscosity extrusion
ID	Inner diameter
IR	Infrared, in this context also ultrafast visible-pump – infrared probe spectroscopy
LB	Lysogeny broth medium
LCLS	Linac Coherent Light Source, XFEL in California, US
LCP	Lipidic cubic phase
LED	Light-emitting diode
LUMO	Lowest occupied molecular orbital
MAG	Monoacyl glycerol
MES	2-(N-Morpholino) ethanesulfonic acid
MPD	Methyl-2,4-pentanediol
MR	Molecular replacement
MS	Mass spectrometry
MWCO	Molecular weight cut-off
NaCMC	Carboxymethylcellulose sodium salt
NTA	Nitrilotriacetic acid
OG	Octyl β-D-glucopyranoside
PCR	Polymerase chain reaction
PDB	Protein Data Bank
PEG	Polyethylene glycol
PM	Purple membranes
PP	Photoproduct
PSB	Protonated Schiff base
QM	Quantum mechanics
RMSD	Root mean square deviation
rpm	Rotations per minute
SACLA	SPring-8 Angstrom Compact free electron Laser, XFEL in Japan
SDS	Sodium dodecyl sulfate
SEC	Size exclusion chromatography
SFX	Serial femtosecond crystallography
SOC	Super optimal broth supplemented with glucose
SRI, SRII	Sensory rhodopsin I, II
TEMED	Tetramethylethylenediamine

TEV	Tobacco etch virus
Tris	Tris(hydroxymethyl)aminomethane
TRL	thermolysin
TR-SFX	Time-resolved serial femtosecond crystallography
VIS	Visible spectral region, in this context also ultrafast visible-pump – visible probe spectroscopy
(*v*/*v*)	Volume per volume
wt	Wild-type
(*w*/*v*)	Weight per volume
(*w*/w)	Weight per weight
XFEL	X-ray free-electron laser

Amino acids, three and one letter codes

alanine	Ala	A
arginine	Arg	R
asparagine	Asn	N
aspartic acid	Asp	D
cysteine	Cys	C
glutamic acid	Glu	E
glutamine	Gln	Q
glycine	Gly	G
histidine	His	H
isoleucine	Ile	I
leucine	Leu	L
lysine	Lys	K
methionine	Met	M
phenylalanine	Phe	F
proline	Pro	P
serine	Ser	S
threonine	Thr	T
tryptophan	Trp	W
tyrosine	Tyr	Y
valine	Val	V